Formulation and Application of the Neutral Particle Beam Deposition Code SINBAD

Yühe Feng

IPP III/190

January 1993

MAX-PLANCK-INSTITUT FÜR PLASMAPHYSIK

8046 GARCHING BEI MÜNCHEN

Formulation and Application of the Neutral Particle Beam Deposition Code SINBAD

Yühe Feng

IPP III/190

January 1993

ABSTRACT

A fast computer code, SINBAD (**SI**mplified **N**eutral **B**eam **A**ttenuation and **D**eposition), which simulates the neutral particle beam injection into tokamak plasmas has been developed. The SINBAD code is based on a simplified beam model which nevertheless accurately describes the beam intensity distribution and particle trajectories in the plasma. Compared with Monte Carlo codes, such as TRANSP and FREYA, the SINBAD code has the advantage that it requires much less CPU time for about the same degree of calculating accuracy.

Direct measurement of the beam deposition profile is very difficult. In this work, the beam deposition profile is investigated indirectly through its effects on neutron production and plasma energy content. For cold plasmas, the neutron rate mainly depends on the electron temperature and the beam particle deposition rates. The beam deposition profile is changed by varying the plasma density during beam injection. The corresponding change in the global neutron rate is observed by means of neutron counters. Discharges with counter-injection are investigated. The experimental observations agree very well with the theoretical calculations. In spite of their small number, the fast ions significantly increase the global plasma energy content. For some ASDEX discharges investigated, both the theoretical calculations and the diamagnetic flux measurements have consistently indicated that the increases in transverse energy content from ohmically heated plasmas to neutral beam heated plasmas are mainly due to the fast particle populations.

A first successful method to deduce neutron emission profiles from nuclear emulsion plate measurements is presented. The procedure is tested first by NEPMC (**N**uclear **E**mulsion **P**late **M**onte **C**arlo) simulations and then applied to two ASDEX discharges. Due to the lack of other relevant measurements at ASDEX, the neutron emission profile for a D→D (deuterium injection into deuterium plasma) discharge obtained from the nuclear emulsion measurement is compared with that calculated by the SINBAD+NRFPS code (**N**eutron **R**ate **F**okker-**P**lanck **S**olver). Comparison shows that the measurement agrees well with the calculation.

Contents

PART III

PART IV

1. INTRODUCTON

Tokamak Fusion Research

The aim of fusion-oriented plasma research is to achieve the conditions for a burning plasma, where the thermonuclear power is sufficiently large to replace the power required for plasma heating. The power balance condition for deuterium-tritium reactions is described approximately by the *Lawson criterion:*

$$n\tau \gtrsim 10^{20}\, m^{-3}\, s \tag{1.1}$$

where n and τ are the plasma ion density and the energy confinement time. The fuel temperature actually required T is around 10 keV, that is about 100 million degrees centigrade. In the attempt to reach the *breakeven* conditions, the tokamak has become the predominant research tool (KADOMTSEV *et al.*, 1990). According to the two IFRC (International Fusion Research Council) reports published in 1978 and in 1990, the fusion triple product $n\tau T$ was increased by almost two orders of magnitude in twelve years of tokamak experiments. The *breakeven* conditions have almost been reached in the JET tokamak (REBUT *et al.*, 1991).

Heating tokamak plasmas to fusion temperatures has already been demonstrated. However, confining sufficiently dense plasmas at such high temperatures has turned out to be very difficult. Any effort to increase the plasma temperature in a tokamak by auxiliary heating has led to severe degradation of confinement. Understanding the physics of confinement in the presence of auxiliary heating remains a challenge to physicists working in the field. The exploration of the particle and energy transport mechanisms in tokamak plasmas requires, on the one hand, diagnostics capable of providing adequate spatial and temporal resolution, and on the other hand, reliable theories to explain experimental observations and calculate the quantities which are hardly available from measurements.

Neutral Beam Injection

Neutral particle beam injection plays an important role in tokamak research for current drive, fueling and diagnostics as well as plasma heating. Neutral atom beams can be injected across magnetic field lines and then trapped in the plasma by ionization. The resulting fast ions are slowed down by Coulomb collisions. As the slowing-down occurs energy is transferred to the particles of the plasma, causing heating of both electrons and ions (DUESING *et al.*, 1987; GRISHAM *et al.*, 1985; MATSUDA *et al.*, 1987). Neutral beams also provide a particle source to offset the diffusion losses and can give rise to an electric current in the plasma which can partially replace the transformer-induced

Ohmic current, thereby allowing extension of the operational domain in tokamaks (ZARNSTORFF *et al.*, 1988; CHALLIS *et al.*, 1989). A further exploited potential of the neutral beam is that it can serve as a diagnostic tool. Both active charge-exchange spectroscopy and the energy spectrum of passive charge-exchange neutral atoms leaving the plasma include information about background ions (DAVIS *et al.*, 1983; FIORE *et al.*, 1988; WEISEN *et al.*, 1989). In addition to these desirable effects, neutral particle beam injection may have deleterious effects on plasma equilibrium and confinement in a plasma. That energy confinement decreases with increasing beam heating power has been observed in all tokamak experiments (WAGNER *et al.*, 1989).

Investigation of the above-mentioned effects requires essentially a knowledge of the beam deposition. Direct measurement of particle, momentum and energy absorption from the injected beam is very difficult and is thus routinely replaced by computations. To develop a fast computer code for simulating neutral particle beam injection into tokamak plasmas and to investigate the effects of the fast particles on the plasma energy content as well as on neutron production are the main objectives of this thesis.

Neutron Diagnostic

Measurement of the density and temperature of the fusing ion species is of great importance. For this purpose, for further experiments, neutron diagnostics will become one of the most promising diagnostic tools. Neutrons as fusion product carry information about the reacting ions. Since neutrons, having no charge, do not interact with electromagnetic fields, they can be well traced from measurements back to the plasma.

Neutron counters have been installed at most tokamaks to measure global neutron rates with good temporal resolution (JARVIS, 1991). The nuclear emulsion method has been used for accurate measurement of the neutron yield and estimation of the average ion temperature of a discharge (JARVIS *et al.*, 1986; HÜBNER *et al.*, 1989). However, both diagnostics remain to be improved to allow measurement with adequate spatial resolution. Neutron emission profiles are routinely measured at the JET tokamak by using a number of neutron counters viewing different plasma regions (MARCUS *et al.*, 1991). An effort to measure neutron emission profiles by means of nuclear emulsion has been made by HÜBNER *et al.* (1989) by setting a nuclear emulsion plate as close to the plasma as possible. The remaining problem is to analyze the recoil proton tracks in order to determine the spatial origin of the neutron emission.

In this work, a successful method is introduced to deduce the neutron emission profile from the angular distribution of recoil proton tracks measured by nuclear emulsion plates. The procedure is first tested by NEPMC simulations and then applied to ASDEX discharges.

PART I

2. Neutral Beam Attenuation and Deposition

A fast and sufficiently accurate simulation of the neutral particle beam deposition is essential for investigating the detailed behaviour of the resulting fast ions, e.g. the momentum and energy transport. Due to the multiple dimensionality of the source distribution function associated with the beam geometry and the optical properties, Monte Carlo techniques have usually been used in previous beam deposition codes such as FREYA, NFREYA, FAFNER and TRANSP (Lister *et al.*, 1976; Fowler *et al.*, 1979; Lister *et al.*, 1985, Goldston *et al.*, 1981). Although very successful, Monte Carlo codes require much CPU time since a large number of neutral atoms have to be followed in order to achieve reasonable statistical fluctuations.

Due to a reduction of the beam geometry, as performed in the PENCIL code (Stubberfield *et al.*, 1987), the problem could be treated analytically and thus the computation could be significantly speeded up. However, due to the strongly simplified beam model used in PENCIL, the deposition profiles are wrongly calculated when the poloidal flux sections are comparable with the beam width, i.e. in the central plasma region. In addition, regardless of the fact that the fast ions, once they are born in the plasma, follow drift surfaces and not just flux surfaces, the PENCIL code is not very suitable for tokamak plasmas where the toroidal plasma current is not strong enough to suppress this unwished effect caused by the inhomogeneity and curvature of the toroidal magnetic field, as is the case in ASDEX.

Therefore, it is necessary to develop a new deposition code that can provide a fast and reasonably accurate evaluation of the neutral particle deposition. Clearly, an appropriate approximation to the beam geometry is the key to speed up the computation. Therefore, attention will first be paid to the treatment of the beam geometry, with emphasis on investigation of the particle trajectories and the beam intensity distribution in the plasma.

Once a fast ion is born in the plasma, its motion is influenced by the electromagnetic fields. The initial drift motion of the fast ions before being slowed down will be discussed in detail.

2.1 Attenuation of the Neutral Particle Beam in the Plasma

As the neutral particles pass through the plasma, they will be removed from the incident beam through interactions with the background plasma, i.e. ionization and charge exchange. As a consequence, the intensity of the incident beam is reduced on its way through the plasma.

For a monoenergetic neutral particle beam with an infinitesimal cross section dA_o, the transmitted intensity at an observation point O (FIG.2.1.1), $I(x_o)$, is found from the incident beam intensity I_s to be

$$I(x_o) = I_s \exp\left(-\int_O^{S_o} dS/\lambda\right), \tag{2.1.1}$$

where the integration is performed along the trajectory from the source to the observation point O. Futhermore, λ is the mean free path length, which can be written as

$$\frac{1}{\lambda} = \frac{\langle \sigma_e V_e \rangle}{V_B} n_e + \frac{\langle (\sigma_{cx} + \sigma_{ion}) V_{rel} \rangle}{V_B} n_i + \sum_j \sigma_j n_j . \tag{2.1.2}$$

Here, V_B is the beam velocity, $\langle \sigma_e V_e \rangle$ is the product of the electron impact ionization cross section and the electron velocity averaged over a Maxwellian with the local electron temperature. It can be assumed that the beam velocity is negligibly small as compared with the electron mean thermal velocity, i.e $V_{rel} = V_e - V_B \approx V_e$. Furthermore, n_e, n_i are the local electron density and the local density of the hydrogen isotopes and σ_{cx}, σ_{ion} are the charge exchange and the ion impact ionization cross sections. The product of the total cross section and the relative velocity V_{rel} is averaged over an appropriate velocity distribution for the dominant ions in the plasma. The total capture cross section for the impurity ion species j with the local density n_j is σ_j. The mean thermal velocity of the impurity ions has been neglected in equation (2.1.2) because it is usually much smaller than the beam velocity ($V_{rel} \approx V_B$).

An actual neutral particle beam can be characterized by an intensity distribution $f(x_b, v)$, where x_b and v are the spatial coordinates on a source face and the velocity coordinates of the beam particles. Thus, the incident intensity of the monoenergetic infinitesimal beam in equation (2.1.1), I_s, can be described by

$$I_s = f(x_b, v)\, dx_b dv \tag{2.1.3}$$

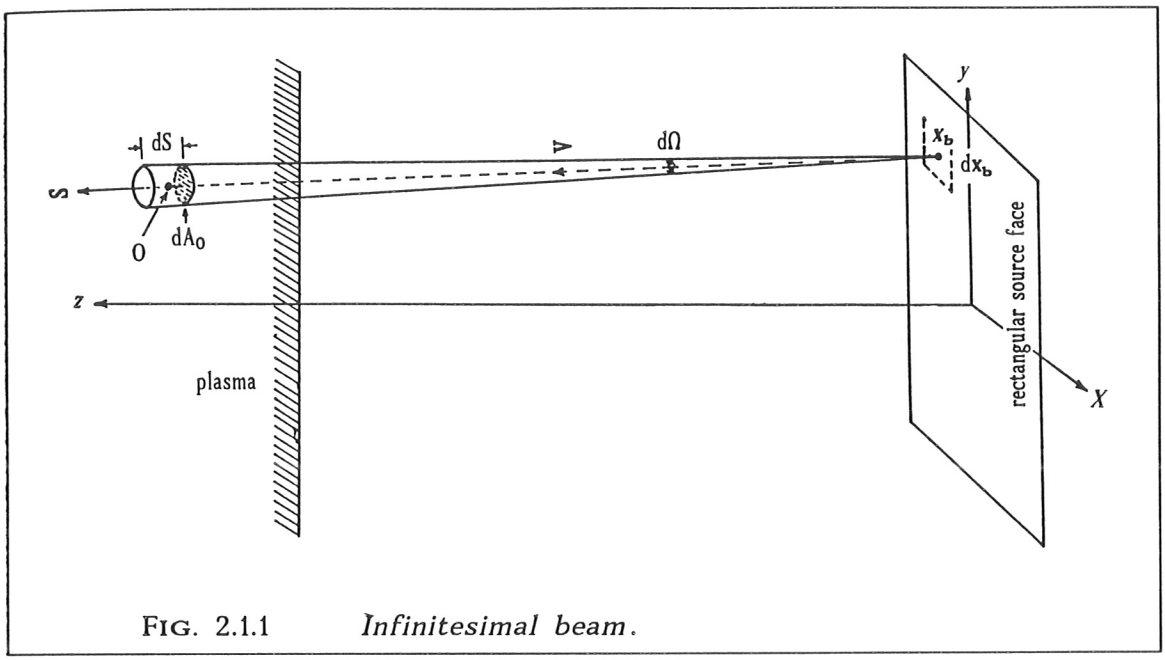

FIG. 2.1.1 *Infinitesimal beam.*

with

$$\iint f(\boldsymbol{x}_b, \boldsymbol{v})\, d\boldsymbol{x}_b d\boldsymbol{v} \;=\; N_{inj}\,, \tag{2.1.4}$$

where N_{inj} is the total number of neutrals injected per second into the plasma. Differentiating with respect to the path length S in equation (2.1.1), one obtains the number of the neutral particles trapped per second in dS at the point $\boldsymbol{O}$, $dN_{dep}(\boldsymbol{x}_o)$:

$$\begin{aligned} dN_{dep}(\boldsymbol{x}_o) \;&=\; -dI(\boldsymbol{x}_o) = \; I_s \exp\Big(-\int_0^{S_o} dS/\lambda\Big)\,\frac{dS}{\lambda(\boldsymbol{x}_o)} \\ &=\; f(\boldsymbol{x}_b, \boldsymbol{v})\, d\boldsymbol{x}_b\, \upsilon^2 d\upsilon\, d\Omega \exp\Big(-\int_0^{S_o} dS/\lambda\Big)\,\frac{dS}{\lambda(\boldsymbol{x}_o)}\,, \end{aligned} \tag{2.1.5}$$

where the relation $d\boldsymbol{v} = \upsilon^2 d\upsilon\, d\Omega$ has been used. Note that $dA_o = S_o^2 d\Omega$ (FIG. 2.1.1). The local particle deposition rate contributed by the incident infinitesimal beam, $dn_{dep}(\boldsymbol{x}_o)$, is given by

$$dn_{dep}(\boldsymbol{x}_o) = \frac{dN_b(\boldsymbol{x}_o)}{dA_o dS} = \frac{1}{\lambda(\boldsymbol{x}_o)}\,\frac{\upsilon^2}{S_o^2}\, f(\boldsymbol{x}_b, \boldsymbol{v}) \exp\Big(-\int_0^{S_o} dS/\lambda(s)\Big)\, d\boldsymbol{x}_b d\upsilon. \tag{2.1.6}$$

Adding up all the contributions of the neutrals emitted from the whole source face and with different velocities, we get

$$n_{dep}(\boldsymbol{x}_o) \;=\; \iint \frac{1}{\lambda(\boldsymbol{x}_o)}\,\frac{\upsilon^2}{S_o^2}\, f(\boldsymbol{x}_b, \boldsymbol{v}) \exp\Big(-\int_0^{S_o} dS/\lambda(s)\Big)\, d\boldsymbol{x}_b d\upsilon\,, \tag{2.1.7}$$

where $n_{dep}(x_o)$ is the total beam deposition rate at the observation point O. The total number of particles trapped per second in the three-dimensional plasma, N_{dep}, is given by

$$N_{dep} = \int [\iiint \frac{1}{\lambda(x_o)} \frac{v^2}{S_o^2} f(x_b, v) \exp\left(-\int_0^{S_o} dS/\lambda(s) \right) dx_b dv] dx_o . \qquad (2.1.8)$$

This appears to be an eight-dimensional integration including $\int dS$. It will be seen that the velocities of the injected particles have only three discrete values. For monoenergetic particles, the integration (2.1.8) has a dimensionality of six due to the flat nature of the source region. For arbitrary plasma profiles and source distribution rates, analytical evaluation of the integral presents an intractable problem, and so numerical methods are required. However, the integration continues to be a time consuming problem although there are different suitable methods available. Therefore, the reduction of its dimensionality is the key to decreasing the computation time. This can be realized by appropriately simplifying the beam intensity distribution function.

2.2 Beam Model

In this section, a simplified model of the beam geometry is derived. Based on this approximation, the integration (2.1.8) is performed partly analytically so that the dimensionality of the remaining integral which has to be solved numerically can be significantly reduced.

2.2.1 General Beam Configuration

The position s of a source of an injector is determined by R_S and Z_S (FIG. 2.2.1.a) in a cylindrical coordinate system with origin in the center of the tokamak. The beam axis is defined by a tangential radius R_t relative to the torus center and an angle β_S (FIG. 2.2.1.b) with respect to the median plane.

Before entering the plasma, the neutral atoms emerging from a circular source face will be focussed at a distance of Z_f from the source, whereas those from a rectangular source face are usually separately focussed in the horizontal and vertical planes (FIG. 2.2.2). The total beam from a source consists of a number

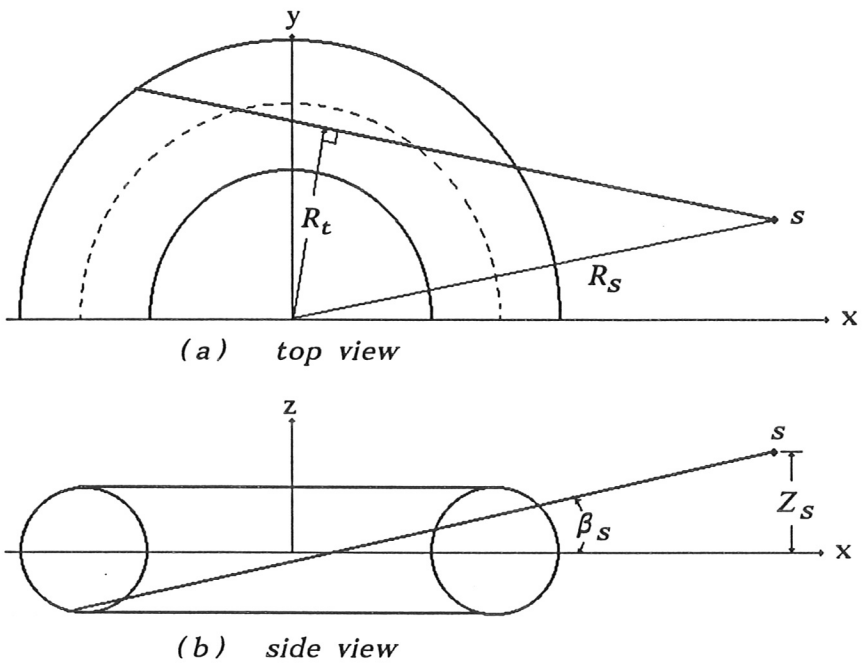

FIG. 2.2.1: *Beam geometry.*

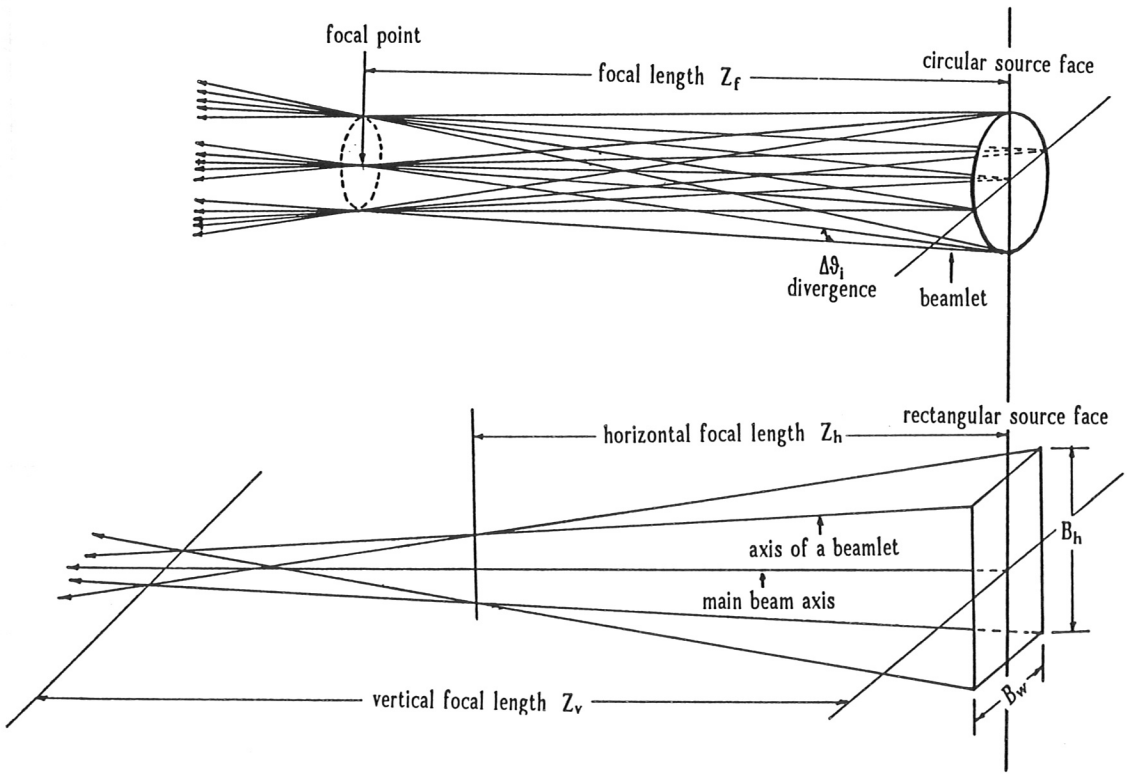

FIG. 2.2.2: *Beam divergence and focussing.*

2.2.2 Simplified Beam Model

Now, let us see how strongly the attenuation factor $\int dS/\lambda$ along the path S in the equation (2.1.7) will depend on the source face coordinates $\boldsymbol{x}_b$ if it varies over the complete source face. Note that λ, for monoenergetic atoms, is only a function of the plasma flux surface positions.

For this purpose, we consider monoenergetic atoms which come from different parts of a circular source face and pass through, for instance, the point P in the plasma. These particles form a narrow beam as shown in FIG. 2.2.3. Due to the finite size of the source face, the narrow beam has a finite width $2R_b$, which

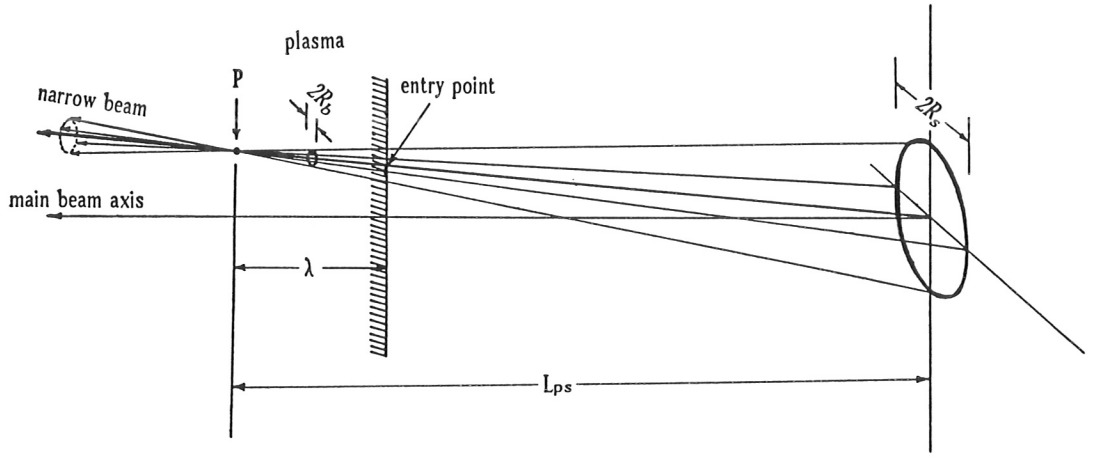

FIG. 2.2.3 *Narrow beam model.*

depends on the distance of the observation position to the reference point P. In practice, the incident neutral particles can only travel a small distance in the plasma before they are ionized or undergo charge-exchange processes. The typical traveling distance of the neutral particles in the plasma is characterized by the mean free path length λ, which depends on the local plasma conditions and the properties of the injected particles. If the reference point P is selected in a plasma region where most of the neutral particles are ionized or undergo charge exchange, the average size of the narrow beam between the entry point and the reference point can be reasonably estimated by

$$2R_b = \frac{\lambda/2}{L_{ps}} 2R_s, \qquad (2.2.2.1)$$

where R_s and L_{ps} are the radius of the circular source face and the distance between the source and the reference point P. The parameters of the background plasma and the neutral particle beam are generally chosen such that the neutral particles reach the plasma center in order to heat it up with little

shine through the plasma. According to ROME *et al.* (1974), the mean free paths of the neutrals are comparable to the plasma minor radius in this case. Replacing λ by the minor plasma radius a, we rewrite equation (2.2.2.1) as

$$2R_b \approx \frac{R_s}{L_{ps}}\, a \,. \qquad (2.2.2.2)$$

For most neutral beam injector arrangements the ratio R_s/L_{ps} has small values (for example, for ASDEX R_s/L_{ps} is about 0.02). Hence, the diffuseness of the narrow beam in the plasma is usually very small compared with the size of the poloidal plasma section.

Let us now consider such a narrow beam injected into an ASDEX plasma. The reference point P is fixed at a distance of about *50 cm* from the entry point according to the typical mean free path length of the atoms injected into ASDEX plasmas. If a point $\boldsymbol{x}_b$ on the source face is selected, a straight trajectory through P is formed. The atoms traveling along this trajectory are attenuated in the plasma according to $exp[-\int dS/\lambda(\varkappa(S,\boldsymbol{x}_b))]$, where $\varkappa$ is the normalized flux surface radius and is a function of S and $\boldsymbol{x}_b$. As $\boldsymbol{x}_b$ varies on the source face, new trajectories are formed and thus the atoms have to be followed along each trajectory through the plasma. However, due to the appropriate selection of the reference point P, the flux surface radius $\varkappa$ along each trajectory of the narrow beam depends very slightly on its origin $\boldsymbol{x}_b$, as shown in FIG. 2.2.4. Here, the flux surface radius $r=a\varkappa$ as a function of the path length S along different trajectories is illustrated. The five given trajectories are traced out by the atoms emitted in the center (blacked line) and at four edge points on the circular source face, which itself has a radius of *10 cm.*

FIGURE 2.2.4 shows that the narrow beam widens only in the region far away from the reference point. In practice, only a small number of neutrals can reach this region without being ionized or lost by charge exchange. In the region of interest, where the most neutral atoms are ionized or undergo charge exchange, the average beam size is less than *1 cm*, which is much less than the spatial resolution of any local diagnostic system at ASDEX.

The plasma volume in JET is about *20* times larger than that in ASDEX. The JET neutral particle injector system consists of two injectors arranged symmetrically around the torus and at a distance of about *12 m* with respect to the tokamak center. Each of the two injectors includes eight atom sources which are divided into two groups, i.e. tangential and normal beams, according to their different injection angles with respect to the torus. Two narrow beams corresponding to the tangential and normal beams respectively are shown in FIG. 2.2.5. Each of them is formed by the atoms emerging from the edges and the center of the corresponding source face.

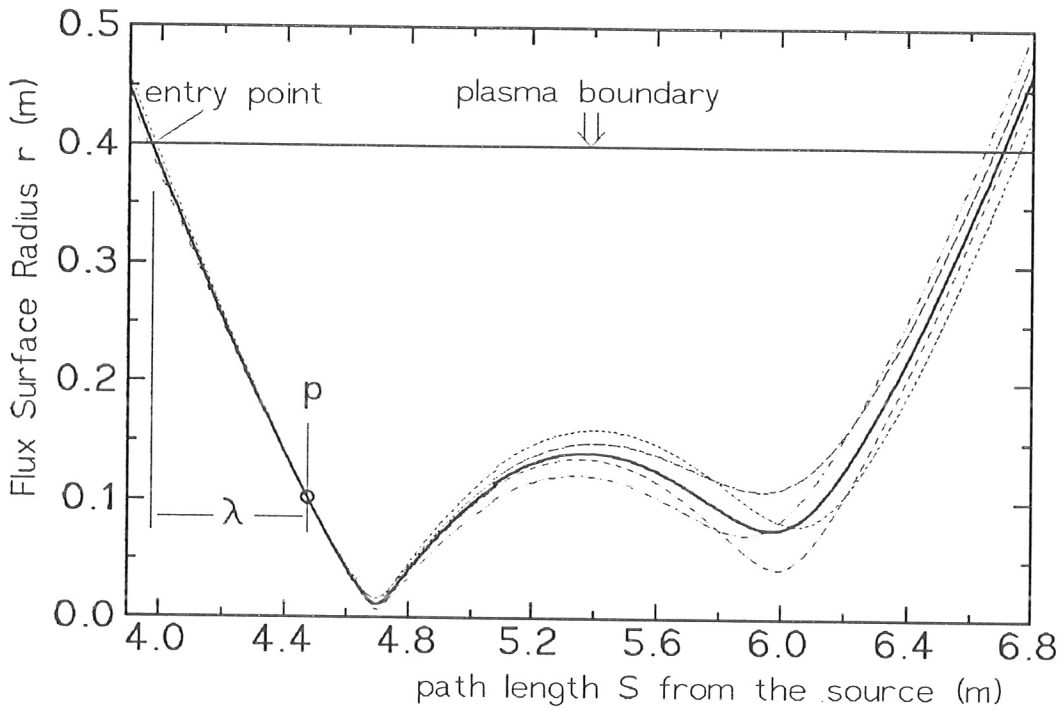

FIG. 2.2.4 *Flux surface radius as a function of the path length along different trajectories of a narrow beam through the ASDEX plasma.*

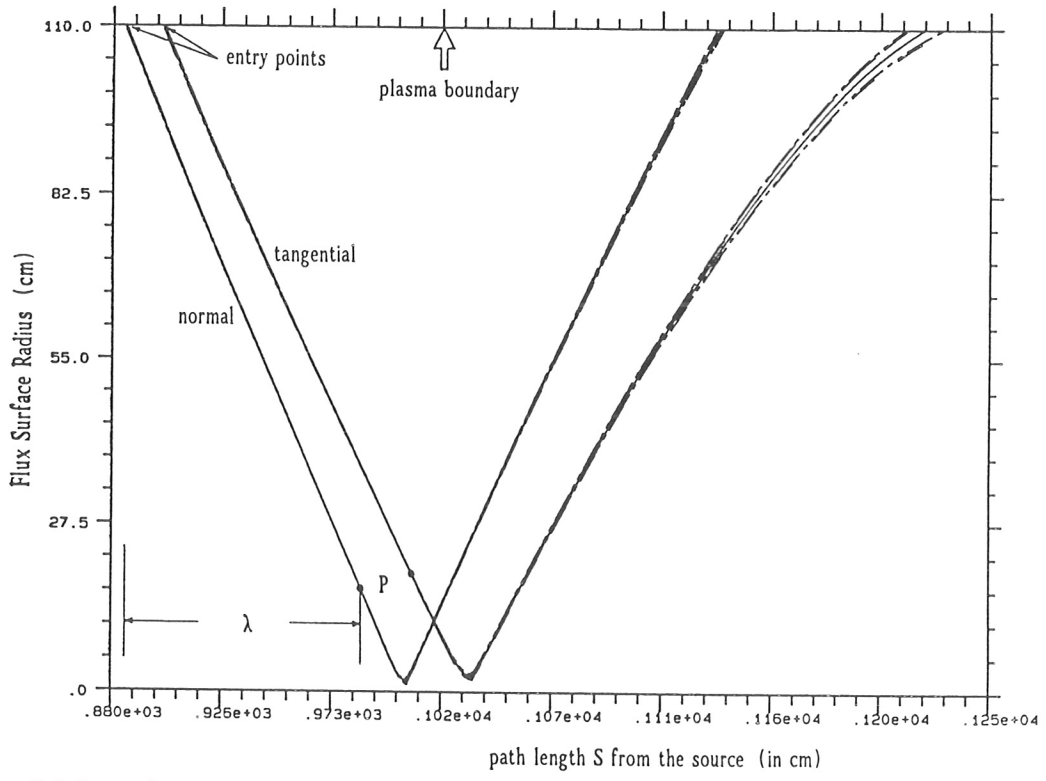

FIG. 2.2.5 *Flux surface radius as a function of the path length along different trajectories of a tangential and a normal narrow beam through the JET plasma.*

According to the discussion above, the diffuseness of the narrow beam caused by the finite size of the source face can be neglected since it is usually beyond the resolution used in the calculations. With this assumption, all neutral atoms in the narrow beam travel through plasma along the same trajectory as those coming from the source center. Hence, the beam source can actually be regarded as a point source.

The remaining problem is to calculate the incident intensity of the narrow beam such that the atoms involved are followed just one time.

2.2.3 Beam Intensity Distribution

Since the magnitude of the velocity of the injected particles has only three discrete values, we divide $f(\boldsymbol{x}_b, \boldsymbol{v})$ into three parts:

$$f(\boldsymbol{x}_b, \boldsymbol{v}) = \sum_{j=1}^{3} f_j(\boldsymbol{x}_b, \boldsymbol{v}_j) \qquad (2.2.3.1)$$

with $$\iint f_j(\boldsymbol{x}_b, \boldsymbol{v}_j)\, d\boldsymbol{x}_b d\boldsymbol{v}_j = c_j N_{inj},$$

where c_j is the fraction of the particles with velocity v_j.

For each energy component, the intensity distribution of the beamlets on a source face can be described by $f_j(\boldsymbol{x}_b)$. Assuming that the divergence of each beamlet is $\Delta\vartheta_j$, one can write the intensity distribution of a monoenergetic beam as

$$f_j(\boldsymbol{x}_b, \boldsymbol{v}_j) = \frac{c_j N_{inj}}{\pi v_j^2 \Delta\vartheta_j^2} f_j(\boldsymbol{x}_b) \exp\left[-\left(\frac{\vartheta_b}{\Delta\vartheta_j}\right)^2\right] \qquad (2.2.3.2)$$

with $$\int f_j(\boldsymbol{x}_b) d\boldsymbol{x}_b = 1,$$

where ϑ_b is the angle between the axis of a beamlet with origin at $\boldsymbol{x}_b$ and an atom trajectory in the beamlet.

According to the point source model, the trajectory of a narrow beam can be described by a pitch angle ϑ and an azimuthal angle φ with respect to the main beam axis (FIG.2.2.6). For a given (ϑ,φ), a reference point on this trajectory is fixed by z_p, which is determined according to the mean free path of the atoms along the trajectory through a given plasma. The incident intensity of the narrow beam is calculated by integrating the contributions of each beamlet through the reference point.

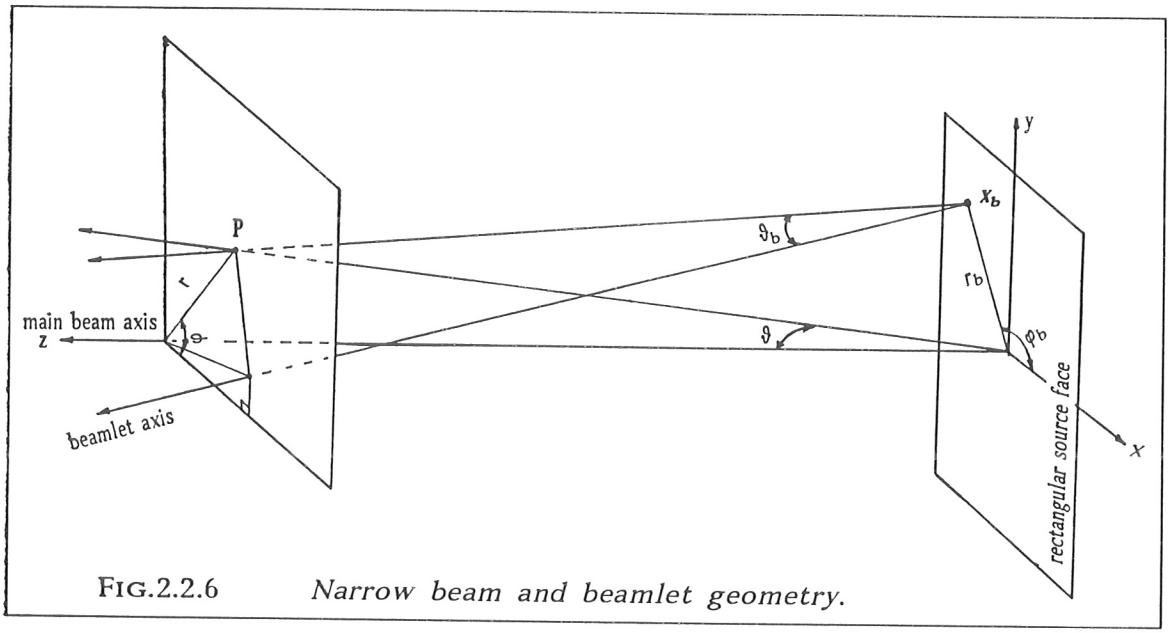

FIG.2.2.6 *Narrow beam and beamlet geometry.*

For a given point $\boldsymbol{x}_b$ on a source face, a beamlet is selected and its axis is determined in Cartesian coordinates with origin at the source face center by

$$\begin{cases} x = (1-\frac{z}{Z_h})\,x_b\,, \\ y = (1-\frac{z}{Z_v})\,y_b\,, \end{cases} \tag{2.2.3.3}$$

where Z_h and Z_v are the focal lengths in the horizontal plane and the vertical plane, respectively. The straight trajectory of the atoms emitted from $\boldsymbol{x}_b$ and passing through P is described by

$$\frac{x-x_b}{x_P-x_b} = \frac{y-y_b}{y_P-y_b} = \frac{z-z_b}{z_P-z_b}\,, \tag{2.2.3.4}$$

where (x_P,y_P,z_P) are the Cartesian coordinates of the reference point. Thus, the angle between the beamlet axis and the trajectory ϑ_b is determined by

$$\cos\vartheta_b = \frac{-x_b(x_P-x_b)\frac{z_P}{Z_h} - y_b(y_P-y_b)\frac{z_P}{Z_v} + z_P^2}{\sqrt{(x_b\frac{z_P}{Z_h})^2+(y_b\frac{z_P}{Z_v})^2+z_P^2}\,\sqrt{(x_P-x_b)^2+(y_P-y_b)^2+z_P^2}}\,. \tag{2.2.3.5}$$

Since the beam divergence $\Delta\vartheta_j$ is rather small, the beamlet is concentrated around the beamlet axis and hence ϑ_b is also small. With the approximation $\cos\vartheta_b \approx 1-\vartheta_b^2/2$, equation (2.2.3.5) can be approximated to

$$\vartheta_b^2 \approx \vartheta^2 - \frac{2}{z_p^2}\left[x_p x_b\left(1-\frac{z_p}{Z_h}\right) + y_p y_b\left(1-\frac{z_p}{Z_v}\right)\right] + \frac{1}{z_p^2}\left[x_b^2\left(1-\frac{z_p}{Z_h}\right)^2 + y_b^2\left(1-\frac{z_p}{Z_v}\right)^2\right] \quad (2.2.3.6)$$

with $$\vartheta^2 = \frac{x_p^2 + y_p^2}{z_p^2}.$$

The incident density of the narrow beam, $i_j(\vartheta,\varphi)$, is then given by

$$i_j(\vartheta,\varphi) = \frac{c_j N_{inj}}{\pi v_j^2 \Delta\vartheta_j^2} \iint f_j(x_b,y_b)\, exp\left[-\left(\frac{\vartheta_b}{\Delta\vartheta_j}\right)^2\right] dx_b dy_b$$

$$= \frac{c_j N_{inj}}{\pi v_j^2 \Delta\vartheta_j^2}\, exp\left(-\alpha^2\right) \iint f_j(x_b,y_b) \cdot \quad (2.2.3.7)$$

$$exp\left[\frac{1}{z_p^2 \Delta\vartheta_j^2}\left(2\delta_h x_p x_b + 2\delta_v y_p y_b - x_b^2\delta_h^2 - y_b^2\delta_v^2\right)\right] dx_b dy_b ,$$

where $\alpha = \frac{\vartheta}{\Delta\vartheta_j}$, $\delta_h = 1-\frac{z_p}{Z_h}$ and $\delta_v = 1-\frac{z_p}{Z_v}$.

The integration in equation (2.2.3.7) can be carried out by expanding the exponential function into polynomials.

Assuming a beam source with a circular face indicated by the radius R_s and assuming that the beam intensity distribution over the source face is $f_j(r_b)$, where

$$2\pi \int_0^{R_s} f_j(r_b) r_b dr_b = 1, \quad (2.2.3.8)$$

we obtain from equation (2.2.3.7) with $Z_h = Z_v = Z_f$

$$i_j(\vartheta,\varphi) = \frac{c_j N_{inj}}{\pi v_j^2 \Delta\vartheta_j^2}\, e^{-\alpha^2}\left\{1 + \rho\zeta_1(\alpha^2 - 1) + \frac{1}{3}\rho^2\zeta_2(\alpha^4 - 4\alpha^2 + 2) + \cdots\right\} \quad (2.2.3.9)$$

with $$\rho = \frac{1}{2}\left(\frac{R_s}{\Delta\vartheta_j z_p}\right)^2\left(1 - \frac{z_p}{Z_f}\right)^2,$$

$$\zeta_n = \frac{n+1}{R_s^{2n}}\, 2\pi \int_0^{R_s} f_j(r_b)\, r_b^{2n+1} dr_b \quad (n=1, 2, \cdots).$$

Here, the factor ρ is determined mainly by the beam source properties and only weakly depends on the position of the reference point associated with the mean free path of the neutral particles injected into a given plasma. With present arrangements of neutral particle injectors at tokamaks, the neutral particle beams are possibly focussed on the plasma center in order to achieve a desired heating efficiency. In this case, the factor ρ takes small values (for example, the typical value of ρ for the injector arrangement at ASDEX is less than 0.1). The coefficients ζ_n, which reflect the beam intensity distribution on the source face, usually take values in the range from *0* to *1* ($\zeta_n \equiv 1$ if $f_j(r_b)$ is constant). Thus, the high order terms in equation (2.2.3.9) can be neglected for use in practical calculations.

For a rectangular source, the beam intensity distribution on the source face is usually considered to be constant. With a rectangular source having a width B_w and a height B_h being assumed, integration of equation (2.2.3.7) yields

$$i_j(\vartheta,\varphi) = \frac{c_j N_{inj}}{\pi v_j^2 \Delta\vartheta_j^2} e^{-\alpha^2}\{1 + \rho_h(\alpha^2\cos^2\varphi - \tfrac{1}{2}) + \rho_v(\alpha^2\sin^2\varphi - \tfrac{1}{2}) + \cdots\} \qquad (2.2.3.10)$$

with

$$\rho_h = \frac{1}{6}\left(\frac{B_w}{\Delta\vartheta_j z_p}\right)^2\left(1 - \frac{z_p}{Z_h}\right)^2 \quad \text{and} \quad \rho_v = \frac{1}{6}\left(\frac{B_h}{\Delta\vartheta_j z_p}\right)^2\left(1 - \frac{z_p}{Z_h}\right)^2.$$

Due to the asymmetry of the beam geometry, the intensity distribution, equation (2.2.3.10), for a rectangular source depends, in contrast to a circular source, on the azimuthal angle φ.

With the point source model and the corresponding beam intensity distributions (2.2.3.9) and (2.2.3.10), equations (2.1.7) and (2.1.8) become

$$n_{dep}(\mathbf{x}_o) = \sum_{j=1}^{3} \frac{1}{\lambda_j(\mathbf{x}_o)} \frac{v_j^2}{S_o^2} i_j(\vartheta_o,\varphi_o) \exp\left(-\int_0^{S_o} dS/\lambda_j(s)\right), \qquad (2.2.3.11)$$

$$N_{dep} = \int\left[\sum_{j=1}^{3} \frac{1}{\lambda_j(\mathbf{x}_o)} \frac{v_j^2}{S_o^2} i_j(\vartheta_o,\varphi_o) \exp\left(-\int_0^{S_o} dS/\lambda_j(s)\right)\right] d\mathbf{x}_o. \qquad (2.2.3.12)$$

Comparing equation (2.1.8) with equation (2.2.3.12), one finds that the dimensionality of the integral is reduced from six to four. Consequently, the computational time will be significantly reduced. Due to the approximation of the beam geometry, the error in determining the fast ion deposition is estimated to be less than 1% in calculations for ASDEX discharges.

2.3. Plasma Geometry

In a tokamak, the plasma is kept in equilibrium by a complex magnetic field configuration. The equilibrium can be described by the balance equation

$$\nabla P = \boldsymbol{j} \times \boldsymbol{B}, \tag{2.3.1}$$

where the pressure-gradient force is balanced by the Lorentz force. Equation (2.3.1) tells us that the current density $\boldsymbol{j}$ and the magnetic field $\boldsymbol{B}$ are each perpendicular to ∇P. This means that, if the magnetic field lines tend to form a flux surface, the plasma pressure on this surface must be constant and no current can pass through it. In order to determine the shapes and the positions of the magnetic flux surfaces in a given tokamak plasma, it is convienent to express $\boldsymbol{B}$ in terms of a magnetic flux function. The result is known as the *Grad-Shafranov Equation.*

Solving the *Grad-Shafranov Equation* to evolve the magnetic flux surface geometry is important, but not the aim of this work. For computer simulations of the behavior of the fast particles, an analytical representation of the flux surface geometry is preferred, e.g. the Lao representation, which is an approximate solution to the *Grad-Shafranov Equation* obtained by LAO *et al.* (1981) using a variational method. Here, it is assumed that the flux surfaces possess up-down symmetry. Furthermore, the flux surface coordinates (R,z), given in a cylindrical coordinate system, are expanded in Fourier series of the poloidal angle β. In most cases, a few terms of the Fourier series are sufficient to get a reasonable accuracy for describing the flux surfaces.

In this work, we are using the first two terms in the expansion and thus

$$\begin{cases} R = R_0(\varkappa) - a\,\varkappa\cos\beta + R_2(\varkappa)\cos 2\beta, \\ z = E(\varkappa)\,(a\,\varkappa\sin\beta + R_2(\varkappa)\sin 2\beta), \end{cases} \tag{2.3.2}$$

where the amplitudes $R_0(\varkappa)$, $R_2(\varkappa)$ and $E(\varkappa)$ describe the position and shape of each flux surface. The variable $\varkappa$ is normalized to the minor radius a and indicates different flux surfaces.

Replacing $R_0(\varkappa)$ and $R_2(\varkappa)$ by the more convenient parameters $S(\varkappa)$ and $D(\varkappa)$, i.e. the Shafranov shift and the triangularity of the flux surfaces, and using the relations $R_0(\varkappa)=R_0+S(\varkappa)-D(\varkappa)/4$ and $R_2(\varkappa)=D(\varkappa)/4$, one can rewrite the expression (2.3.2) as

$$\begin{cases} R = R_O + S(\varkappa) - \frac{1}{4}D(\varkappa) - a\varkappa\cos\beta + \frac{1}{4}D(\varkappa)\cos 2\beta, \\ z = E(\varkappa)[a\varkappa\sin\beta + \frac{1}{4}D(\varkappa)\sin 2\beta], \end{cases} \tag{2.3.3}$$

where the condition $a\varkappa >> R_2(\varkappa)$ has been used. The parameter $E(\varkappa)$ indicates the ellipticity of the flux surfaces. The geometrical meanings of the parameters involved in equation (2.3.3) are illustrated in FIG.2.3.1, where S_O and D_o are the Shafranov shift of the innermost flux surface and the triangularity of the outermost flux surface.

For current tokamak plasmas, the following fit formulas are suggested for some flux surface parameters:

$$S(\varkappa) = \sum_{n=O}^{3} s_n \varkappa^{2n}, \qquad E(\varkappa) = \sum_{n=O}^{3} e_n \varkappa^{2n}, \qquad D(\varkappa) = \sum_{n=1}^{3} d_n \varkappa^{2n}, \tag{2.3.4}$$

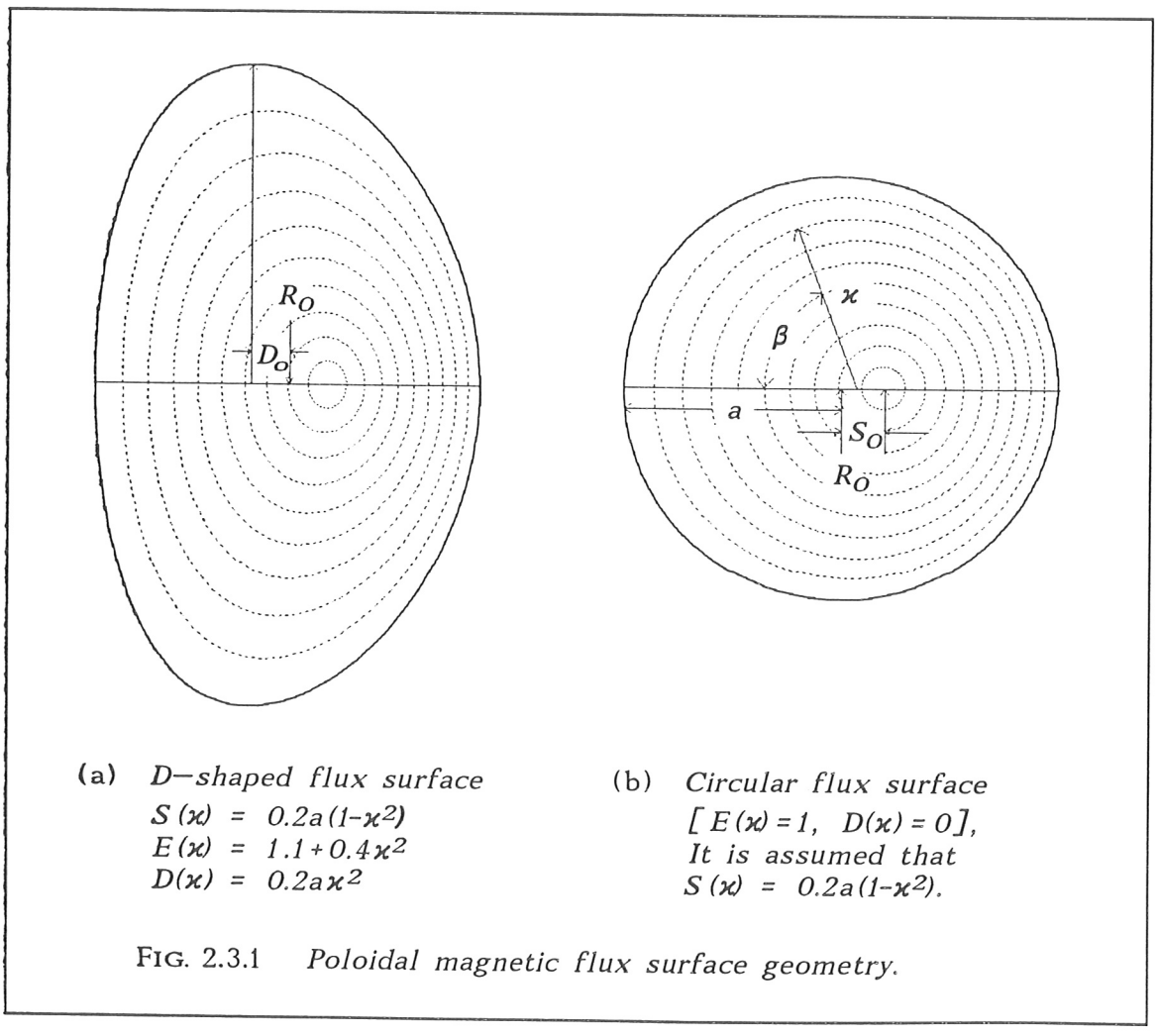

(a) *D–shaped flux surface*
$S(\varkappa) = 0.2a(1-\varkappa^2)$
$E(\varkappa) = 1.1+0.4\varkappa^2$
$D(\varkappa) = 0.2a\varkappa^2$

(b) *Circular flux surface*
$[E(\varkappa)=1,\ D(\varkappa)=0]$,
It is assumed that
$S(\varkappa) = 0.2a(1-\varkappa^2)$.

FIG. 2.3.1 *Poloidal magnetic flux surface geometry.*

where the coefficients s_n, e_n and d_n are usually available from a plasma equilibrium code. Alternatively, the values for $S(\varkappa)$, $E(\varkappa)$ and $D(\varkappa)$ to describe the flux surface geometry can also be introduced directly.

The integration of a plasma parameter or a function g over the full plasma volume V_{tot} is described in the cylindrical coordinate system by

$$G = 2\pi \iint R\, g\, dR\, dz, \tag{2.3.5}$$

where the symmetry in the toroidal direction has been taken into account.

Because of the convenient representation of the plasma boundary conditions, it is favorable to perform this integration in the plasma coordinate system:

$$G = 2\pi \int_0^1 \int_0^{2\pi} R(\varkappa, \beta)\, |J|\, g\, d\varkappa\, d\beta, \tag{2.3.6}$$

where $|J|$ is the Jacobi determinant of the expression (3.3) and is given by

$$|J| = \frac{\partial R}{\partial \varkappa}\frac{\partial z}{\partial \beta} - \frac{\partial R}{\partial \beta}\frac{\partial z}{\partial \varkappa} \tag{2.3.7}$$

If it is borne in mind that g is generally a function of the flux surface coordinates and is independent of the poloidal angle β, the integration over β can immediately be carried out. Then equation (2.3.4) can be rewritten as

$$G = \int g(\varkappa)\, dV(\varkappa), \tag{2.3.8}$$

where $V(\varkappa)$, i.e. is the plasma volume enclosed by the flux surface $\varkappa$, is given by the following expression:

$$V(\varkappa) = 2\pi^2 \left[R_0 + S(\varkappa) - \tfrac{1}{4} D(\varkappa)\right]\left[a^2\varkappa^2 - \tfrac{1}{8} D(\varkappa)^2\right] E(\varkappa). \tag{2.3.9}$$

As expected, the plasma volume enclosed by a flux surface is completely determined by its geometrical parameters.

2.4. Collision Cross Sections

For the plasma conditions at tokamak experiments, the dominant atomic collision processes are charge exchange and ionization of the ground state beam atoms by plasma particles. For a plasma density of less than 10^{14} cm^{-3} and a beam energy smaller than 80 *keV/A* (*A* is the mass number of the beam atom), the excited beam atom density is negligibly smaller than that of the ground state ones. Therefore, neither ionization nor charge exchange of the excited beam atoms is considered here.

Cross sections for ion impact ionization and charge exchange in a plasma consisting of hydrogen isotopes and impurities are taken from the interpolation formulae given by RIVIERE (1971). For small energies, i.e. in the range $\frac{E}{A} \leq 150$ keV, where E is in *eV*, the ionization cross section is determined by

$$\log_{10}\sigma_{ion} = -0.8712\,(\log_{10}{}^{E/A})^2 + 8.156\,\log_{10}{}^{E/A} - 34.833, \qquad (2.4.1)$$

where the cross section σ_{ion} is given in cm^2. In the high energy range ($\frac{E}{A} > 150$ keV), it is approximated by

$$\sigma_{ion} = 3.6\cdot10^{-12}\,(\tfrac{E}{A})^{-1}\,\log_{10}{}^{(0.1666\,E/A)} \quad [cm^2]. \qquad (2.4.2)$$

The expression for the charge-exchange cross section is

$$\sigma_{cx} = \frac{0.6937\cdot10^{-14}\,(1-0.155\log_{10}{}^{E/A})^2}{1+0.1112\cdot10^{-14}\,(\frac{E}{A})^{3.3}} \quad [cm^2]. \qquad (2.4.3)$$

The ionization and charge-exchange cross sections by ion impact are illustrated in FIG.2.4.1. For a beam energy *E/A* smaller than ~80 *keV/A*, charge exchange between the beam atom and the plasma ion is the dominant collision process, while the ionization impact becomes important for a high beam energy (*E/A*>80*keV*).

The total trapping cross section for the impurity species j depends on their charge q_j. JANEV *et al.* (1989) have given the following fit formula:

$$\tilde{\sigma}_j = 7.457 \left[\frac{1}{1 + 0.081\,\tilde{E}} + \frac{2.754}{64.58 + \tilde{E}} \ln(1 + 1.27\,\tilde{E}) \right] \cdot 10^{-16} \quad [\mathrm{cm}^2], \quad (2.4.4)$$

where $\tilde{\sigma}_j$ and $\tilde{E}$ are defined as

$$\tilde{\sigma}_j = \frac{\sigma_j}{q_j}, \qquad \tilde{E} = \frac{E(keV)}{A q_j} \quad . \quad (2.4.5)$$

The rate coefficients $\langle \sigma_e V_e \rangle$ for electron impact ionization at electron temperatures below 5 *keV* are based on the tables used by LISTER (1985), which are originally presented by FREEMAN and JONES (1974). A point at 10 keV is taken from SWEETMAN (1973). FIGURE 2.4.2 gives the rate coefficients in the range of electron temperatures from 10 *eV* to 10 *keV*.

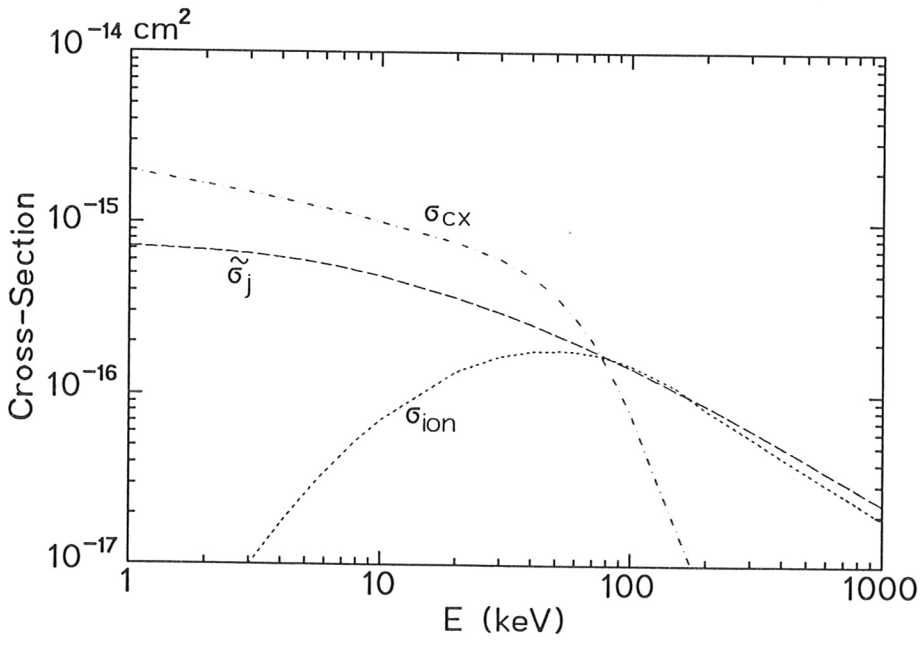

FIG. 2.4.1 *Collision cross sections of hydrogen isotopes and plasma impurities*

σ_{ion}: *Ionization cross section of the hydrogen isotopes*
σ_{cx}: *Charge-exchange cross section with hydrogen isotopes*
$\tilde{\sigma}_j$: *q-scaled electron loss cross section by impurity impact*

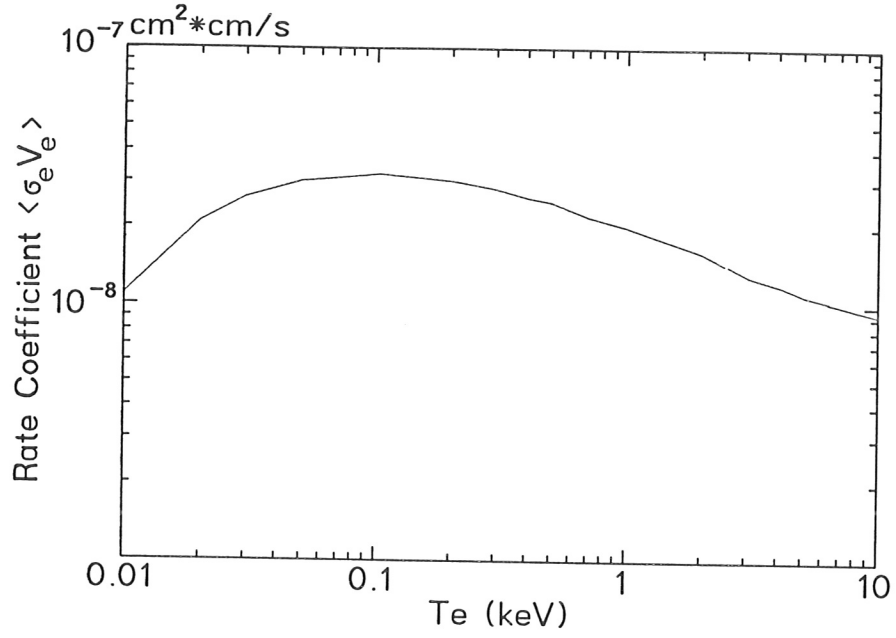

FIG. 2.4.2 *Rate coefficient of electron impact ionization at different electron temperatures.*

2.5 Fast Ion Birth Deposition

In this section we present two methods of performing the calculation, i.e. local depositions at the points chosen in three-dimensional plasmas and deposition profiles as a function of the flux surfaces according to different requirements.

For diagnostics based on the local population of the neutral particles, such as CXRS (**C**harge e**X**change **R**ecombination **S**pectroscopy) and neutral particle analyzers, it is desirable to have a theoretical prediction about the local deposition of the injected particle. In these cases, only information on sightlines is required.

2.5.1 Local Information

Once an observation point (x_o,y_o,z_o) is selected in the plasma, some narrow beams aimed at this point are formed in keeping with the operating sources. The trajectory of each narrow beam is competely determined by the observation point and the source position from which the narrow beam comes. This straight-line path is described in the Cartesian coordinate system with origin in the tokamak center as

$$\frac{x-x_o}{x_s-x_o} = \frac{y-y_o}{y_s-y_o} = \frac{z-z_o}{z_s-z_o} , \qquad (2.5.1.1)$$

where x_s, y_s and z_s are the source coordinates. The incident intensity of the narrow beam is given by equation (2.2.3.9) for a circular source and by equation (2.2.3.10) for a rectangular source, obtained in section 2.2.3 by means of choosing a reference point on the trajectory of the narrow beam. The local fast ion birth deposition rate $n_{dep}(E_j,\boldsymbol{x}_o)$ arising from the narrow beam with energy E_j is then calculated by

$$n_{dep}(E_j,\boldsymbol{x}_o) = \frac{1}{\lambda_j(\boldsymbol{x}_o)} \frac{v_j^2}{S_o^2} i_j(\vartheta_o,\varphi_o) \exp\Big(-\int_{S_e}^{S_o} dS/\lambda_j(S) \Big) \qquad (2.5.1.2)$$

with $$S = \sqrt{(x - x_s)^2 + (y - y_s)^2 + (z - z_s)^2} .$$

Here, the narrow beam is followed along its trajectory from the entry point into the plasma up to the observation point. The entry point is determined by the trajectory and the geometry of the outermost flux surface.

Sometimes the local energy and momentum depositions are also of interest. The energy deposition rate $E_{dep}(\boldsymbol{x}_o)$ arising from the narrow beam is simply given by

$$E_{dep}(\boldsymbol{x}_o) = \sum_{j=1}^{3} n_{dep}(E_j,\boldsymbol{x}_o)\, E_j . \qquad (2.5.1.3)$$

The momentum deposition rate $P_{dep}(\boldsymbol{x}_o)$ can be written as

$$P(\boldsymbol{x}_o) = \Big[\sum_{j=1}^{3} n_{dep}(E_j,\boldsymbol{x}_o) \sqrt{2mE_j} \Big] \boldsymbol{e} , \qquad (2.5.1.4)$$

where the unit vector $\boldsymbol{e}$ on the path of the narrow beam can be expressed in different coordinate systems. The component coefficients e_x, e_y and e_z of the vector $\boldsymbol{e}$ in Cartesian coordinates are given by

$$\begin{cases} e_x = \dfrac{x_o - x_s}{L}, \\ e_y = \dfrac{y_o - y_s}{L}, \\ e_z = \dfrac{z_o - z_s}{L}. \end{cases} \tag{2.5.1.5}$$

It is interesting to express the unit vector $\boldsymbol{e}$ in the plasma coordinate system $(\varkappa,\psi,\beta)$ as

$$\begin{aligned} e_\varkappa &= \frac{\sqrt{(\frac{\partial R}{\partial \varkappa})^2+(\frac{\partial z}{\partial \varkappa})^2}}{|J|}\left[\frac{\frac{\partial z}{\partial \beta}}{\sqrt{x_o^2+y_o^2}}(x_o e_x + y_o e_y) - e_z \frac{\partial R}{\partial \beta}\right], \\ e_\beta &= \frac{\sqrt{(\frac{\partial R}{\partial \beta})^2+(\frac{\partial z}{\partial \beta})^2}}{|J|}\left[\frac{-\frac{\partial z}{\partial \varkappa}}{\sqrt{x_o^2+y_o^2}}(x_o e_x + y_o e_y) + e_z \frac{\partial R}{\partial \varkappa}\right], \\ e_\psi &= \frac{1}{\sqrt{x_o^2+y_o^2}}(x_o e_y - y_o e_x), \end{aligned} \tag{2.5.1.6}$$

where the coefficients $e_\varkappa$, e_β and e_ψ describe the momentum components perpendicular to the flux surface and in the poloidal and toroidal directions, respectively.

The total local deposition rate is the sum of all contributions of the narrow beams from different operating sources.

2.5.2 Deposition Profile

Using the method discussed above, one can obtain a deposition distribution by varying the observation point through the total plasma volume. Furthermore, a deposition profile as a function of the flux surface can be derived through summation of the particles born on the same flux surface. However, because the attenuation factor at each observation point is an integration starting from the entry point of a narrow beam into the plasma, the calculations for the points

located on the same trajectory are partly repeated. In order to avoid repeating the calculation, we follow the particles from the source by dividing the total incident neutral particle beam into a large amount of narrow beams. A narrow beam is defined such that its diffuseness in the plasma can be ignored in the calculation. The intensity $I_b(E_1)$ of the incident narrow beam included in the solid angle element $d\Omega$ is given by

$$I_b(E_1) = \dot{I}_1(\vartheta, \varphi)\, v_1^2 d\Omega, \tag{2.5.2.1}$$

where v_1 is the velocity of the injected atoms with energy E_1. The trajectory of the narrow beam which is determined by choosing ϑ and φ is represented in the Cartesian coordinate system as

$$\begin{cases} y = \vartheta \sin\varphi\,(x - x_s) + y_s, \\ z = (\vartheta\cos\varphi - \beta_s)(x - x_s) + z_s, \end{cases} \tag{2.5.2.2}$$

and the path length S from the source can be written as

$$\begin{aligned} S &= \sqrt{(x - x_s)^2 + (y - y_s)^2 + (z - z_s)^2} \\ &= (x - x_s)\sqrt{1 + (\vartheta\sin\varphi)^2 + (\vartheta\cos\varphi)^2}\,. \end{aligned} \tag{2.5.2.3}$$

The number of atoms which are ionized or undergo charge exchange per second in the step dS on the trajectory is calculated by

$$dN_s = \dot{I}_1(\vartheta, \varphi)\, v_1^2 \vartheta\, d\vartheta\, d\varphi\, \exp\Big(-\int_{S_e}^{S} dS/\lambda\Big)\, \frac{dS}{\lambda_1(S)}, \tag{2.5.2.4}$$

where $d\Omega \approx \vartheta\, d\vartheta\, d\varphi$ has been used.

Now, at each step on the path, number of the trapped atoms and their energy, position and pitch angle ($\mu = y/R$) can be computed exactly. For numbering these particles, a four-dimensional array, BIRTH(E_1, R_i, z_j, μ_k), is required since these coordinates will be used later for averaging the initial deposition over their orbits by using a guiding center theory. The array has $3*N_R*N_z*N_\mu$ elements which cover the full region of atoms being ionized or lost by charge exchange. The volume for each element indicated by E_1, R_i, z_j and μ_k is given by $\Delta V = \Delta R \Delta z \Delta\mu$, where ΔR, Δz and $\Delta\mu$ are the intervals selected for R, z and μ, respectively. The atoms trapped in the step dS with the coordinates (E, R, z, μ) will be stored in the BIRTH(E_1, R_i, z_j, μ_k) array if the following conditions

are satisfied:

$$
\begin{aligned}
E_1 &= E, \\
R_i - \Delta R/2 &\le R < R_i + \Delta R/2, \\
z_j - \Delta z/2 &\le z < z_j + \Delta z/2, \\
\mu_k - \Delta \mu/2 &\le \mu < \mu_k + \Delta \mu/2.
\end{aligned}
$$

After these particles have been stored, the calculation along the path of the narrow beam continues. From the new coordinates of the ionized atoms, the corresponding array element is determined. This continues until the narrow beam reaches the plasma boundary and leaves the plasma. If the narrow beam passes many times through the same element, these contributions are added up. Summation over all narrow beams then gives the resulting deposition distribution.

In some cases, it is favorable to calculate the fast ion birth deposition as a function of the flux surface radius. This can be done by equally dividing the minor radius into N_r intervals of length $\Delta\varkappa$. The plasma volume ΔV_m enclosed by two flux surfaces $\varkappa_m - \Delta\varkappa/2$ and $\varkappa_m + \Delta\varkappa/2$ can easily be calculated from equation (2.3.11). The fast ion birth deposition profile is defined as

$$
H(E_1, \varkappa_m) = N_{1m}/\Delta V_m, \tag{2.5.2.5}
$$

where N_{1m} is the total number of the incident monoenergetic atoms lost per second by ionization or charge exchange in the volume ΔV_m around $\varkappa_m$. It is given by

$$
N_{1m} = \sum_{k=1}^{N_k} \sum_{i=1}^{N_i} \sum_{j=J_1}^{J_2} \mathrm{BIRTH}(E_1,\ R_i,\ z_j,\ \mu_k)\ . \tag{2.5.2.6}
$$

For given R_i and $\varkappa_m$, J_1 and J_2 have to be determined such that the condition

$$
\varkappa_m - \Delta\varkappa/2 \le \varkappa(R_i, z_j) < \varkappa_m + \Delta\varkappa/2 \tag{2.5.2.7}
$$

is satisfied for all j.

2.6 Guiding Center Motion

Once a fast ion is born at a given point in the plasma, it is acted upon by the equilibrium electromagnetic fields in the plasma and suffers collisions with the cold plasma particles. The magnetic fields force the ion to gyrate around the magnetic field line and thus confine it in the plasma. It will then be slowed down and scattered by collisions with the cold particles. Because of its high energy, the mean collision time of the fast ion with the background plasma is much greater than the time it needs for a complete revolution around the torus; hence for the time of the first few revolutions the ion can be treated as a single particle. The initial motion of the collision-free ion is of great interest since it strongly affects the final confinement of the injected particles.

Ion orbits in the tokamak magnetic field can be described approximately as the superposition of two motions: First, gyration about the magnetic field with a gyration radius determined by the magnetic field strength and the properties of the charged ions, and, second, motion of the guiding center, i.e. the point that the ion gyrates around. Due to the vertical drifts of the guiding center caused by the inhomogeneity and curvature of the toroidal magnetic field, a guiding center trajectory can cut several magnetic flux surfaces. Although this drift is averaged and thus reduced by the toroidal helical magnetic field line, which forces a collision-free particle to return to its initial position after a poloidal circle, this drift is so strong for an ion with high energy that the ion can be driven from one magnetic flux surface to another before it passes through the median plane. Being ionized in the region near the boundary, the particle may drift outside the plasma and even hit the wall during its first revolution around the torus. This phenomenon is clearly demonstrated in counter-injection heated plasmas, in which many particles will be lost due to the vertical drift, which will be discussed in detail in the following.

The guiding center motion consists of a motion along the magnetic field, the ∇B drift and the curvature drift. The drift caused by the toroidal magnetic field ripples can be neglected since it is much smaller than the other drifts. The guiding center trajectory is determined by

$$\frac{d\boldsymbol{x}}{dt} = \boldsymbol{V}_{\parallel} + \boldsymbol{V}_{C} + \boldsymbol{V}_{\nabla B} \tag{2.6.1}$$

with the condition

$$\begin{cases} \frac{1}{2} m V_{\parallel}^{2} + \mu^{*} B = E, \\ \mu^{*} = \text{const}, \end{cases} \tag{2.6.2}$$

where $\boldsymbol{x}$ are the ion coordinates, and $\boldsymbol{V}_{\parallel}$, $\boldsymbol{V}_{\mathbf{C}}$ and $\boldsymbol{V}_{\nabla \mathbf{B}}$ are the ion velocity along the magnetic field $\boldsymbol{B}$, the curvature drift velocity and ∇B drift velocity. Furthermore, μ^{*} is the magnetic moment and E is the energy of the fast ion.

Because of the complexity of the flux surface geometry, some approximations in the solution of the guiding center motion equation have been performed in previous works in order to discuss only the qualitative effects of this problem. In the following work we treat the problem as accurately as possible because some parameters such as the Shafranov shift of the flux surface and plasma current distribution, to a certain extent, affect the drift orbits of the fast ions.

For a plasma with a flux surface geometry described by

$$\begin{cases} R = R(\varkappa, \beta), \\ Z = Z(\varkappa, \beta), \end{cases} \tag{2.6.3}$$

equation (2.6.1) with condition (2.6.2) can be rewritten in the poloidal section (the toroidal motion is not interesting due to the toroidal symmetry of this problem) as

$$\begin{cases} \dfrac{d\varkappa}{dt} = -\dfrac{E(1+\mu^2)}{\omega_c m R_O} \dfrac{1}{|J|} \dfrac{\partial R}{\partial \beta} \\ \dfrac{d\beta}{dt} = \dfrac{E(1+\mu^2)}{\omega_c m R_O} \dfrac{1}{|J|} \dfrac{\partial R}{\partial \varkappa} + \dfrac{B_P}{B} \mu \sqrt{\dfrac{2E}{m}} \left[\left(\dfrac{\partial Z}{\partial \beta}\right)^2 + \left(\dfrac{\partial R}{\partial \beta}\right)^2 \right]^{-\frac{1}{2}} \end{cases} \tag{2.6.4}$$

with $\mu = \cos\vartheta$,

where ω_c, B_P and ϑ are the ion cyclotron freqency, the poloidal magnetic field and the pitch angle of the ion velocity with respect to the toroidal plasma current. Furthermore, $|J|$ is the Jacobi determinant of the expression (2.6.3). Note that $B_P << B_t$ (B_t is the toroidal magnetic field). Thus, we can write equation (2.6.4) as

$$\begin{cases} \dfrac{d\varkappa}{dt_x} = -\Delta_x \dfrac{(1+\mu^2)}{2} \dfrac{a}{|J|} \dfrac{\partial R}{\partial \beta} \\ \dfrac{d\beta}{dt_x} = \Delta_x \dfrac{(1+\mu^2)}{2} \dfrac{a}{|J|} \dfrac{\partial R}{\partial \varkappa} + \dfrac{a\varkappa}{q_x(\varkappa)} \dfrac{R}{R_O} \mu \left[\left(\dfrac{\partial Z}{\partial \beta}\right)^2 + \left(\dfrac{\partial R}{\partial \beta}\right)^2 \right]^{-\frac{1}{2}} \end{cases} \tag{2.6.5}$$

with

$$t_x = \frac{t}{\tau}, \qquad \tau = \frac{q_a R_O}{\upsilon},$$

$$\Delta_x = \frac{q_a \upsilon}{a \omega_c}, \qquad q_x(\varkappa) = \frac{B_t(R_O)\, a\varkappa}{q_a B_P R_O},$$

where q_a is the safety factor of the outermost flux surface. For circular flux surface geometry, $q_x(\varkappa)$ is the normalized safety factor of the flux surface $\varkappa$.

If the flux surface geometry is known, equation (2.6.5) can be solved numerically for all cases. The circular flux surface geometry for ASDEX plasmas can be simply represented by

$$\begin{cases} R = R_O + S_O(1-\varkappa^2) - a\varkappa\cos\beta \\ Z = a\varkappa\sin\beta \end{cases} \tag{2.6.6}$$

where S_O is the Shafranov shift of the innermost flux surface. In this case, equation (2.6.5) can be simplified to

$$\begin{cases} \dfrac{d\varkappa}{dt_x} = \Delta_x \dfrac{(1+\mu^2)}{2} \dfrac{\sin\beta}{1-2\varkappa S_{Ox}\cos\beta}, \\ \varkappa \dfrac{d\beta}{dt_x} = \Delta_x \dfrac{(1+\mu^2)}{2} \dfrac{\cos\beta - 2\varkappa S_{Ox}}{1-2\varkappa S_{Ox}\cos\beta} + \varkappa \dfrac{\mu}{q_x(\varkappa)} \dfrac{R}{R_O}, \end{cases} \tag{2.6.7}$$

where $S_{Ox}=S_O/a$. As the ion drifts through different regions of the magnetic field, the pitch angle ϑ ($\mu=\cos\vartheta$) changes in order to conserve its energy and magnetic moment. Since the toroidal magnetic field varies as $1/R$, μ is only a function of R. If an ion is born at the position $(\varkappa_O, \beta_O)$ with the initial pitch angle ϑ_O ($\cos\vartheta_O=\mu_O$), the pitch angle can be determined by

$$\mu(\varkappa,\beta) = \pm\sqrt{1 - \frac{R(\varkappa_O,\beta_O)}{R(\varkappa,\beta)}(1-\mu_O^2)}, \tag{2.6.8}$$

where the ± sign indicates whether $\mathbf{V}\cdot\mathbf{j}$ is positive or negative. Here, $\mathbf{j}$ is the toroidal plasma current density.

As the ion moves toward the inside wall, its transverse energy will increase, which leads to a decrease of its parallel energy component. The particle, which moves too slowly along the magnetic field lines and thus does not have sufficient parallel energy for this energy component conversion, will be reflected and trapped by the magnetic mirror effect. This happens to the particles which are born on the outside of the torus with relatively small μ values. The guiding centers of these trapped particles trace out banana-shaped orbits (FIGS.2.6.1.*a-b*), which is considered to be one of the major particle loss mechanisms in the beam heated tokamak plasmas. Whether a fast ion can spiral around the torus or not depends on its birth position and the initial angle of its velocity with

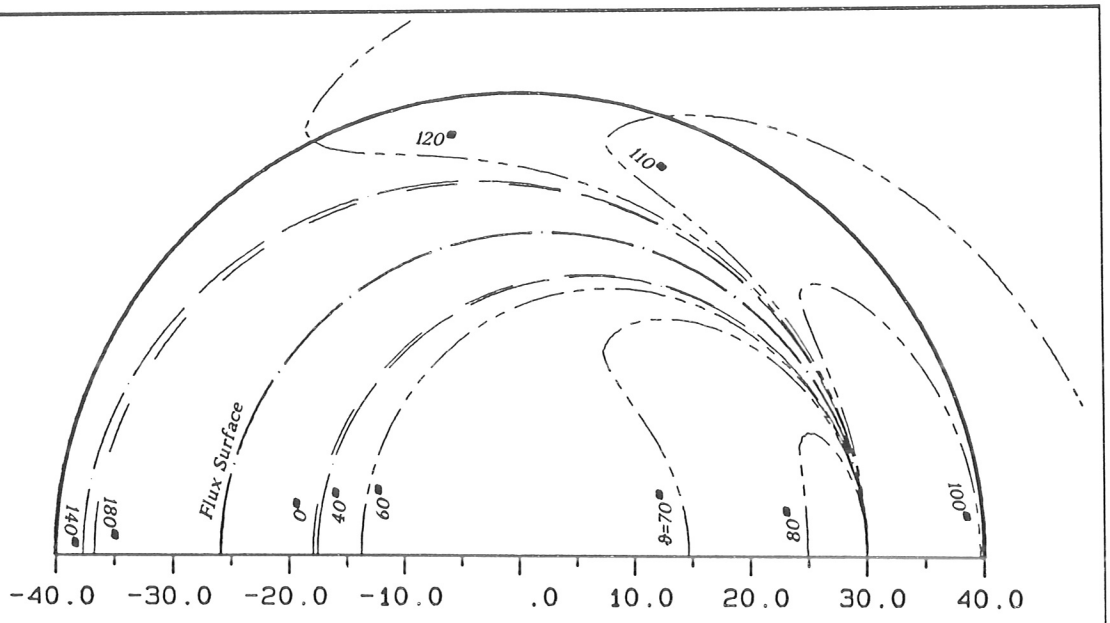

(a) I_P *= 280kA, —·—·— The flux surface on which the ions are born.*

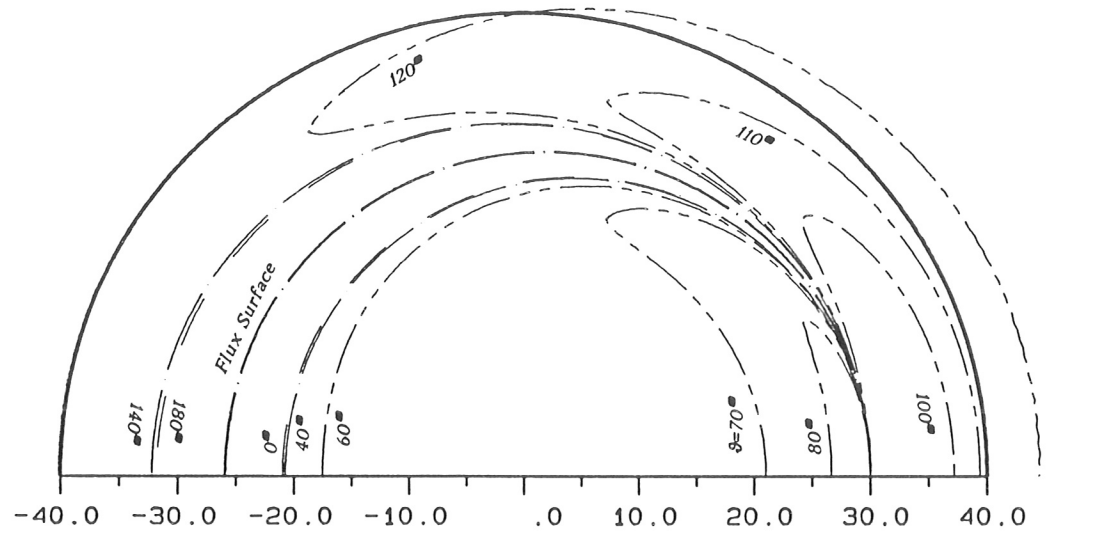

(b) I_P *= 420kA, —·—·— The flux surface on which the ions are born.*

FIG.2.6.1 *Drift orbits of the guiding centers of the fast ions with different pitch angles. In (a) a current of 280 kA is passed through the plasma compared with 420 kA in (b). Particle: deuteron; E=45keV;* S_O*=4cm.*

respect to the toroidal current. The orbits of the ions which are born at the position $(0.61, \pi)$ in an ASDEX plasma with different pitch angles are illustrated in FIG. 2.6.1.*a-b*, for different toroidal currents. Because of their up-down symmetry about the median plane, only the half orbits are shown.

For particles with a pitch angle smaller than about *60* degrees their orbits are whole circles, but the centers of the circles deviate from the center of the flux surface on which the ions are born. As the pitch angle increases, the ions become trapped and perform banana orbits. As long as the pitch angle is smaller than *90* degrees, the orbit is bent toward the inside of the plasma, otherwise toward the outside, till the pitch angle increases to about *120* degrees and the particle can complete the circular orbit again. Unlike the ion with a small pitch angle, which makes a circle with a smaller radius than that of its initial flux surface, the ion with a large pitch angle prefers a circular orbit with a greater radius than that of the flux surface. Both cases show a tendency that, due to the vertical drift, a fast ion cannot be confined on a magnetic flux surface in any case. The two circles traced out by the ions with the pitch angles *0* and π build up a region surrounding the flux surface that no ions born at the given position can reach, which prevents the fast ions from being confined on the flux surface. This unfavorable effect cannot be expected to be rooted out because of the curvature nature of the toroidal magnetic field lines, but can, to a large extent, be reduced by, for example, increasing the toroidal plasma current, as seen in the comparison between FIG. 2.6.1.*a* and FIG. 2.6.1.*b*.

The fact that the drift orbits of the guiding centers of the fast ions will deviate from the flux surface on which they were born was predicted by equation (2.6.7), in which a radial drift is indicated. The radial drift velocity is proportional to the parameter Δ_x, which plays a dominant role in the unwished motion. Its physical meaning can immediately be found if some approximations to equation (2.6.7) are performed. On the assumption that $S_{Ox}=0$ and $q_x(x)=1$ (which corresponds to a constant current density and will be discussed a little later), the orbits of the ions with $\mu=\pm 1$ are whole circles around the centers displaced by $\pm\Delta_x$ from that of the flux surface they should be confined on. For a desired confinement, we hope of course that Δ_x has small values. Recalling the expression for Δ_x and noting that both q_a and ω_c are proportional to B_t, one conseqently finds that Δ_x is proportional to the ion speed v and inversely proportional to the plasma current strength I_p. This means, on one hand, that the particle confinement can be effectively improved by increasing the plasma current, which was demonstrated in FIG. 2.6.1; on the other hand, if the plasma current is selected, the magnetic field configuration in tokamak shows a poorer ability to confine the ions with high energy than those with low energy, as shown in FIG. 2.6.2.

After the effect of the global parameter I_p on the drift orbit has been discussed, let us turn our attention to the normalized safety factor $q_x(x)$, which reflects the current density distribution. For this purpose, it is necessary to assume a current profile. It is

$$j(x) = j_O (1 - x^2)^{\alpha}, \qquad (2.6.9)$$

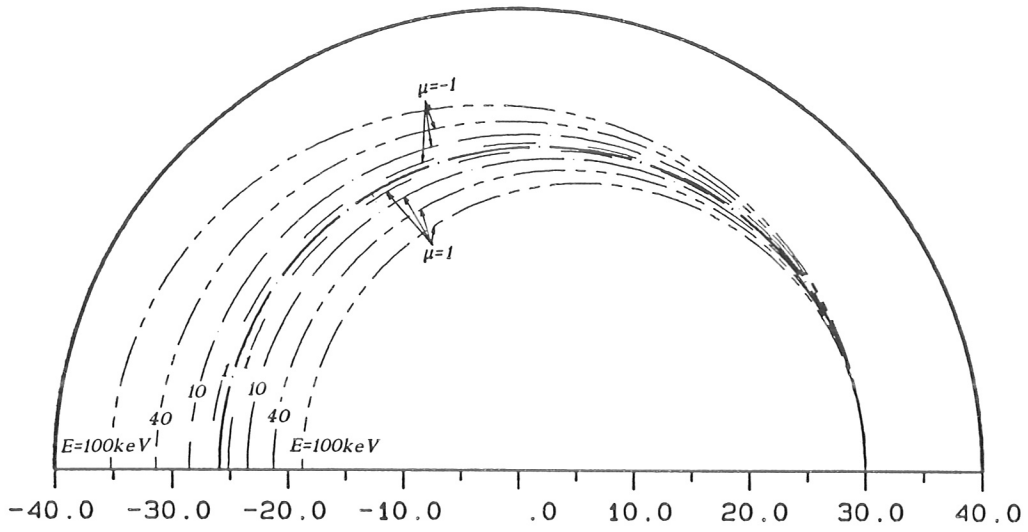

FIG.2.6.2 *Drift orbits of the fast ions with different energies.*
—·—·— Flux surface on which the ions are born. The curves away from the flux surface correspond to ion energies of 1, 10, 40 and 100 keV, respectively. The four curves outside the flux surface are the orbits of ions with μ_O*=-1, otherwise,* μ_O*=1.*

where j_0 is the current density at the plasma center and the parameter α can be varied in order to model different current density distributions. In this case, $q_x(x)$ is given by

$$q_x(x) = \frac{x^2}{1-(1-x^2)^{\alpha+1}} . \qquad (2.6.10)$$

The expected orbits of the ions for different current density distributions are illustrated in FIG. 2.6.3. Here, two identical test particles born in different plasma regions have been taken in order to find out the region where the current density distribution strongly affects the drift orbits. As expected, the orbit of the ion at the plasma boundary hardly responds to the change of the plasma current profile, whereas the inside ion is very strongly forced to its flux surface by peaking the current profile. In short, if I_p remains constant, a peaked current profile is preferred.

The last quantity to be discussed is the Shafranov shift S_{Ox}. Its physical meaning is clear. Note that the center of the circular orbit is displaced from the flux surface center by $\pm\Delta_x$, rather than from the plasma geometrical center. As the flux surfaces move outside, the orbits go outside too. This is very important for counter-injection ($\mu_O<0$), where the inside drift of the orbit relative to the plasma geometrical center will be partly compensated by the outside drift of the flux surface so that the fast particle confinement is improved. This effect is considerable in ASDEX plasma, where S_{Ox} is comparable with Δ_x.

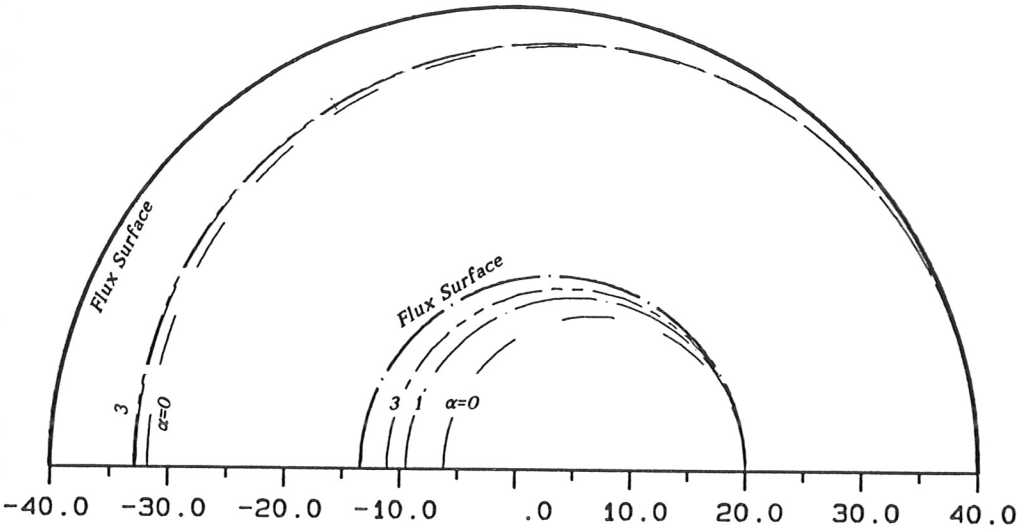

FIG.2.6.3 *Effect of the plasma current distributions upon the ion drift orbits. The curves away from the flux surfaces correspond to current profiles with α=3, 1, 0, respectively. E=45keV, S_O=4cm.*

The fact that the guiding centers of the injected particles drift away from the flux surfaces makes it very difficult to follow them further since their slowing-down properties depend on the local plasma conditions, which are a function of the flux surface position. A straightforward solution to this problem is to follow them in small time steps by using a Monte Carlo method. Unfortunately, this is very time-consuming. A fast method is to average the effects caused by the drifts along their drift orbits. This can be done by, for example, averaging their initial deposition over their drift orbits, as discussed in the next section.

2.7 Orbit-Averaged Beam Deposition

Before averaging the initial ion deposition over the drift orbits, we set up an array $D^*(E_l, \varkappa_m, \mu_n)$ to represent the average deposition. Here, the coordinates E_l, $\varkappa_m$ and μ_n have the same meanings as in section (2.5). We now follow the fast ions stored in the BIRTH(E_l, R_i, Z_j, μ_k) array element in small time steps. Their position $[\varkappa(t_\zeta), \beta(t_\zeta)]$ at the time point t_ζ is determined by integrating equation (2.6.5) as well as equation (2.6.7) according to the flux surface geometry involved. Here, the birth position given in cylindrical coordinates has to be transformed into the plasma coordinate system. For each position, the corresponding pitch angle of the ions is determined by equation (2.6.8) in

the preceding section. The ions are traced till they complete a poloidal orbit. It is reasonable to assume that the ions are redistributed over the drift orbit with the same weight at each time step. Their contribution to the particle deposition in the plasma volume element ΔV_m is proportional to the time Δt_m that the ions spend in ΔV_m. If the selected time step Δt_ζ is much smaller than Δt_m, the fraction of ions stored in BIRTH(E_l, R_i, z_j, μ_k) that contributes to the array element $D^*(E_l, \varkappa_m, \mu_n)$ is given by

$$\Delta D^*(E_l, \varkappa_m, \mu_n) = \frac{\Delta N_{lijk}^{mn}}{N_{lijk}} \text{ BIRTH}(E_l, R_i, z_j, \mu_k), \tag{2.7.1}$$

where ΔN_{lijk}^{mn} and N_{lijk} are the numbers of time steps the ions spend in ΔV_m, and for a complete orbit, in addition, the variation of the pitch angle with the ion position has been taken into account. The total average deposition is given by tracing all fast ions:

$$D^*(E_l, \varkappa_m, \mu_n) = \frac{1}{\Delta V_m} \sum_{k=1}^{N_\mu} \sum_{i=1}^{N_R} \sum_{j=1}^{N_z} \frac{\Delta N_{lijk}^{mn}}{N_{lijk}} \text{ BIRTH}(E_l, R_i, z_j, \mu_k). \tag{2.7.2}$$

It is convenient to rewrite the average deposition $D^*(E_l, \varkappa_m, \mu_n)$ as

$$D^*(E_l, \varkappa_m, \mu_n) = D(E_l, \varkappa_m) \cdot K(E_l, \varkappa_m, \mu_n), \tag{2.7.3}$$

where $D(E_l, \varkappa_m)$ is the average deposition profile given by

$$D(E_l, \varkappa_m) = \sum_{n=1}^{N_\mu} D^*(E_l, \varkappa_m, \mu_n) \tag{2.7.4}$$

and $K(E_l, \varkappa_m, \mu_n)$ is the normalized pitch angle distribution of the ions with energy E_l on the flux surface $\varkappa_m$. The pitch angle distribution can be expanded in Legendre polynomials P_i as

$$K(E_l, \varkappa_m, \mu_n) = \sum_{i=0}^{\infty} k_i(E_l, \varkappa_m) \cdot P_i(\mu_n). \tag{2.7.5}$$

The coefficients $k_i(E_l, \varkappa_m)$ are calculated by

$$k_i(E_l, \varkappa_m) = \frac{2i+1}{2} \sum_{n=1}^{N_\mu} K(E_l, \varkappa_m, \mu_n) \; P_i(\mu_n). \tag{2.7.6}$$

As n varies from 1 to N_μ, the pitch angle takes N_μ discrete values in the range from -1 to 1.

3. The SINBAD Code

The theories discussed in the preceding sections served as a basis for developing a fast computer code for simulation of neutral particle beam injection into tokamak plasmas, SINBAD (**SI**mplified **N**eutral particle **B**eam **A**ttenuation and **D**eposition). The deposition of hydrogen, deuterium or tritium beams can be calculated either locally at chosen points or as a profile for an arbitrary flux surface geometry.

The code is written in FORTRAN as a subroutine, its execution being controlled by several control parameters. The detailed descriptions of the SINBAD code can be found in appendix A. A brief discussion is given in the following.

The SINBAD code is composed of a program package including fourteen main subroutines (FIG. 3.1). Once SINBAD is started, the CKDATA subroutine is called first to check the input data. If any input variable describing the beam and plasma geometries and parameters is found to be unavailable, e.g. not defined in the code or given in an unacceptable unit, the execution will be terminated with

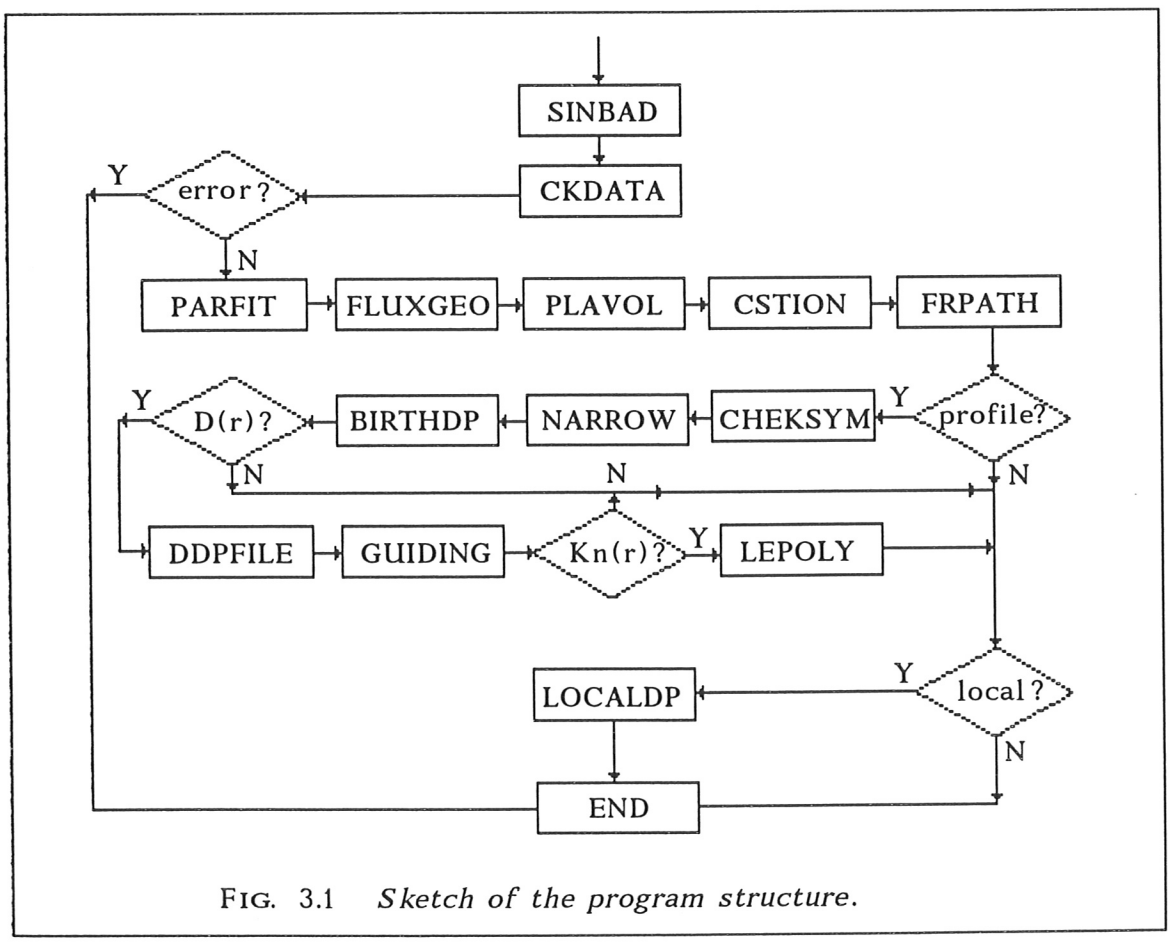

FIG. 3.1 *Sketch of the program structure.*

relevant error messages. Otherwise the input data are transformed by PARFIT into internal variables used in SINBAD. Further quantities necessary to determine the beam deposition are prepared by the FLUXGEO, PLAVOL, CSTION and FRPATH subroutines.

The SINBAD code is able to treat an arbitrary plasma geometry by setting up the data array $\varkappa(R_i,Z_j)$. Here, the corresponding flux surface radii $\varkappa_{ij}$ at the fixed points (R_i,Z_j) specified in the SINBAD code have to be supplied by the user. If there are no specifications, a Lao representation is suggested for the flux surface geometry. In this case, the FLUXGEO subroutine numerically solves the Lao equation to determine the flux radii $\varkappa_{ij}$ at the fixed points (R_i,Z_j). The PLAVOL subroutine is used to calculate the plasma volume element enclosed by any two flux surfaces or to calculate the volume average of a given parameter.

Currently, the collision cross sections for the hydrogen isotope injection are stored in the program. However, the code can also simulate the injection of the other atoms if their relevant collision cross sections are provided. The cross sections at the flux surfaces selected are calculated by CSTION and, if necessary, averaged over appropriate velocity distributions of the target particles. The FRPATH subroutine is used to estimate the average traveling distance of the traced atoms in the plasma in order to select a reference point for determining the beam intensity distribution (s. section 2.2.3).

The calculation of the beam deposition profile starts with the BIRTHDP subprogram, in which the narrow beams created by NARROW are followed on their way through the plasma. If the flux surfaces possess up-down symmetry, the CHEKSYM subroutine is called to find the symmetric sources about the median plane in order to avoid repeating the calculation. A distribution of the initial birth ions over the flux section is provided and then transformed into the plasma coordinates in order to get a deposition profile as a function of the flux surface radius. Furthermore, the initial fast ion distribution is given to DDPFILE and the ions are traced by GUIDING according to the initial positions such that the initial fast ion birth deposition is averaged over their drift orbits. The pitch angle distribution of the ions on each flux surface is expanded in Legendre polynomials and the corresponding expansion coefficients are calculated in LEPOLY.

The LOCALDP subroutine is used to predict local information about the initial deposition of the particles, their energy or momentum according to the different requirements of the user. Once an observation point is given, the trajectory and beam intensity of each narrow beam from each operating source are determined by the observation and source position (s. section 2.5.1). Each narrow beam is then followed from its entry point into the plasma down to the observation point. The contributions of the narrow beams from different operating sources are added up so that the total local deposition rates of particles, energy and momentum are calculated.

4. Comparison of Sinbad with Other Codes

The FREYA and TRANSP codes use Monte Carlo techniques to simulate the injection of neutral particles into tokamak plasmas. The application of FREYA is restricted to circular plasmas. For both cases, the calculation of the beam deposition is performed by generating Monte Carlo particles at the injector, which is weighted by a four-dimensional intensity distribution function accurately representing the neutral beam geometry. The Monte Carlo method is used because of the multiple dimensionality involved in this problem. However, it is very time-consuming.

The PENCIL code, on the other hand, calculates the neutral beam deposition using a simplified beam model where the beam focussing and angular divergence are ignored. The neutral beam is divided into a number of pencil beams described by a two-dimensional intensity distribution function on the source face. The calculations are then carried out by following each pencil beam through the plasma. Using this model, the PENCIL code needs much less CPU time than the Monte Carlo codes to provide a beam deposition profile. Unfortunately, the beam model used in PENCIL is too simple to give as accurate results as are possible with Monte Carlo codes.

The SINBAD code uses a point beam source model based on a reasonable treatment

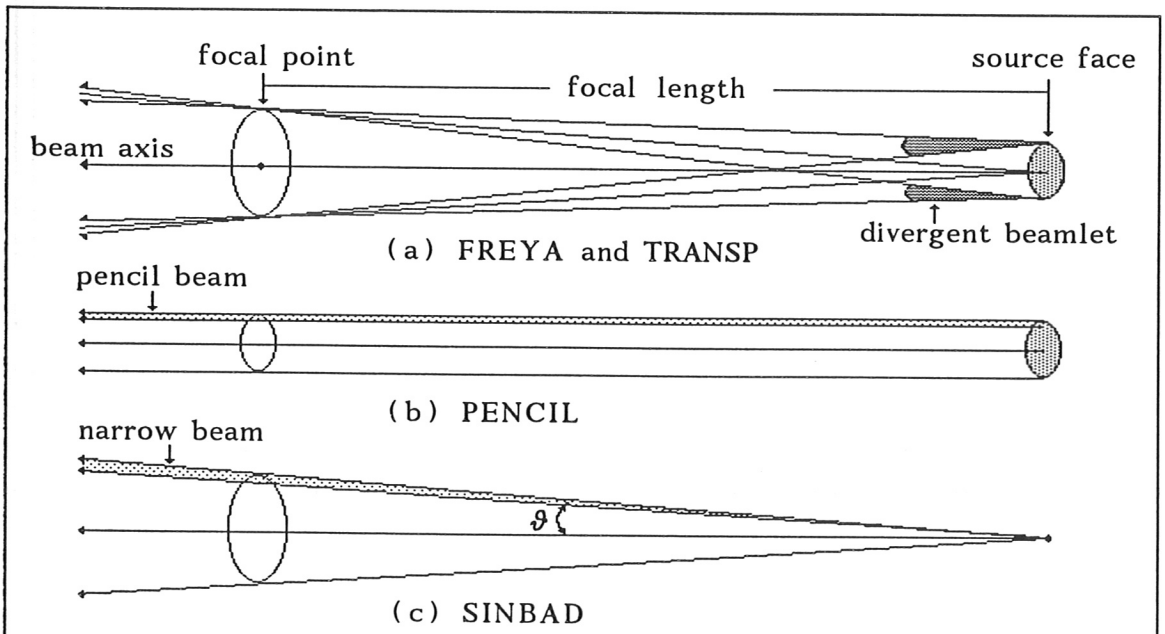

and an appropriate simplification of the beam geometry, with emphasis on investigation of the partice trajectory and the beam intensity distribution in the plasma (s. section 2). The calculations are performed by following narrow beams emitted from each point source along their trajectories through the plasma.

The different beam models used in the four codes are sketched in FIG.4.1.

The spatial beam intensity distributions resulting from the different models for the circular neutral beam source at ASDEX and the data from the NBI group are shown in FIG.4.2. Here, the radial distributions are taken in the plasma at

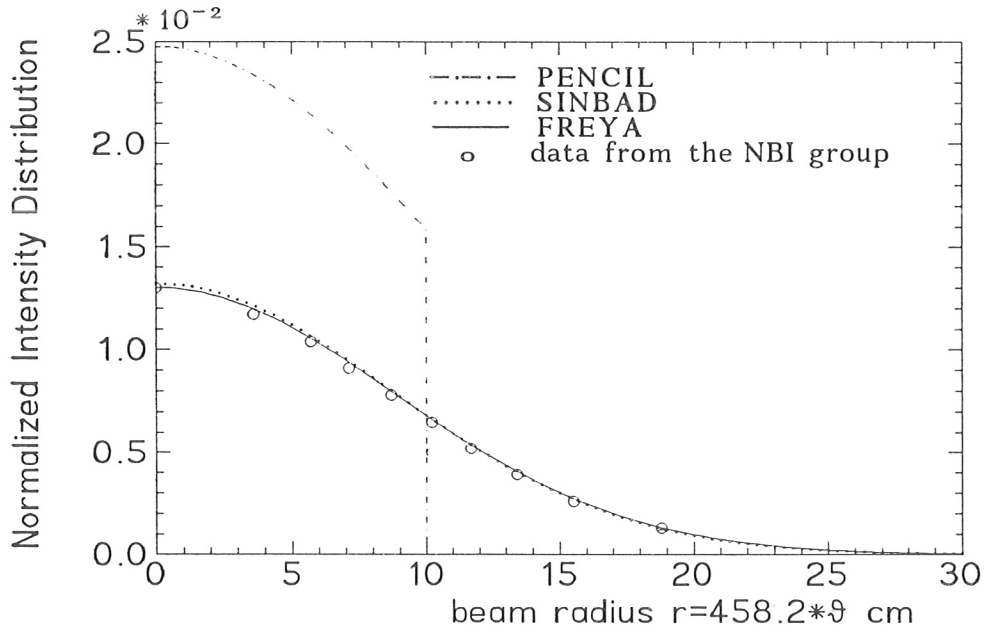

FIG. 4.2: *Comparison of the beam intensity distributions described by different beam models.*

a distance of about 58 cm from the entry point of the beam into the plasma. The beam intensity distribution from SINBAD only slightly deviates from the actual one, while the one provided by PENCIL is much more concentrated around the beam axis as compared with the others. It will be seen that the concentrated beam intensity distribution causes a peaked deposition profile.

Further comparisons of the results from the SINBAD code with those from the other codes have been carried out for some ASDEX and JET discharges. In FIG. 4.3, the initial ion birth deposition profiles for the different energy components for ASDEX discharge #25216 as derived from the SINBAD code and from the FREYA code are plotted as a function of the flux surface radius. Clearly, the 10,000 Monte Carlo particles followed in the FREYA code are not sufficient to suppress the statistical fluctuations.

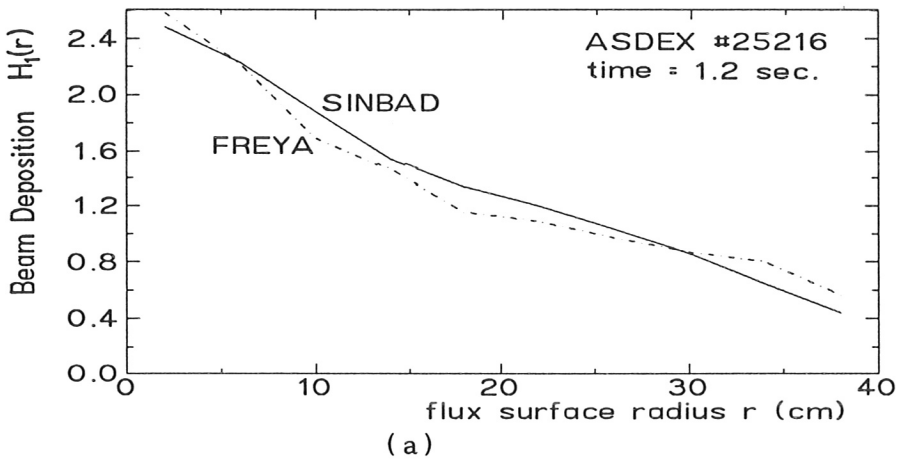

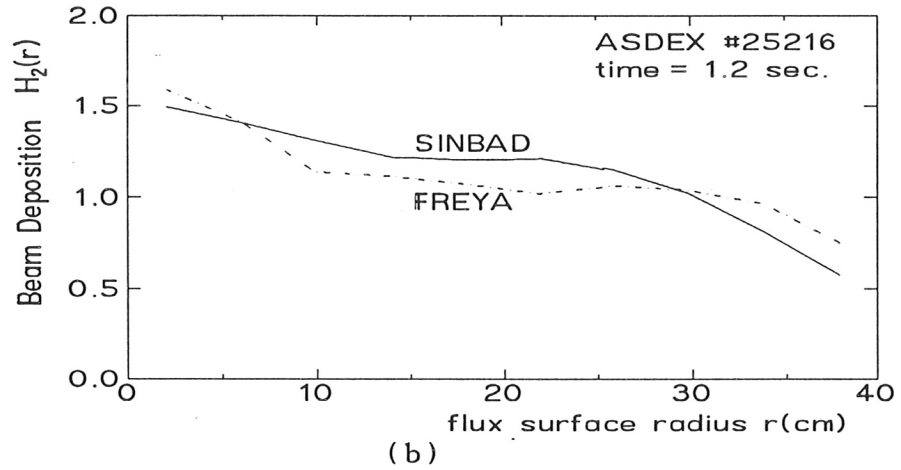

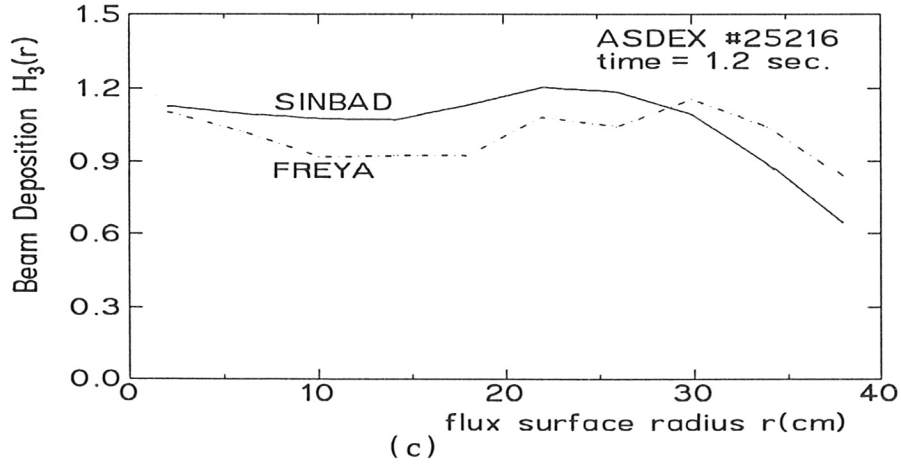

FIG. 4.3: *Comparison of the deposition profiles for ASDEX discharge #25216 derived from FREYA and SINBAD for the full (a), half (b) and one-third (c) energy components.*

Another comparison with FREYA is illustrated in FIG.4.4. In order to reduce the statistical fluctuations, 100,000 neutral particles were followed in FREYA this time. The deposition profile calculated by FREYA is somewhat broader than that from SINBAD. The reason may be that the ionization cross section used in FREYA is somewhat larger than that used in SINBAD. However, the computation time used to determine the beam deposition profiles is reduced by a factor of more than two orders of magnitude by using the simplified beam model in the SINBAD code.

The deposition profiles for ASDEX discharge #24309 calculated with SINBAD and with PENCIL are shown in FIG. (4.5). The deposition profile computed by PENCIL is more peaked in the plasma center than the one from SINBAD. This is due to the missing beam focussing and angular divergence in the beam model used in the PENCIL code.

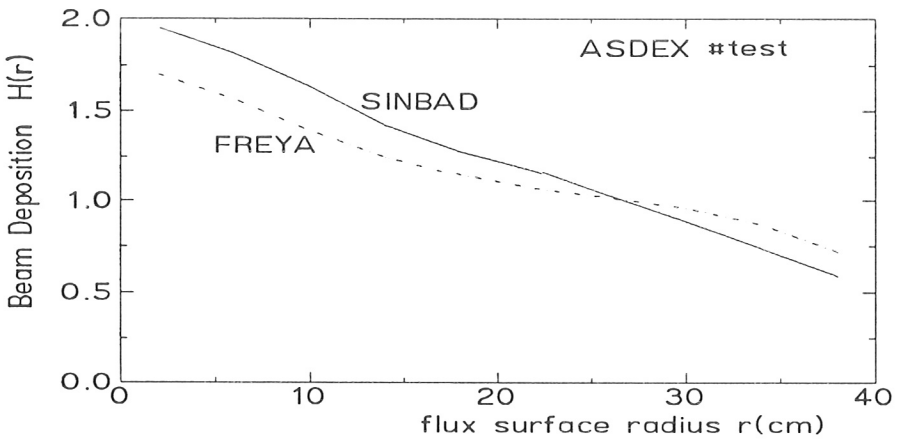

FIG.4.4: *Comparison of the deposition profiles resulting from FREYA and SINBAD (a test at ASDEX).*

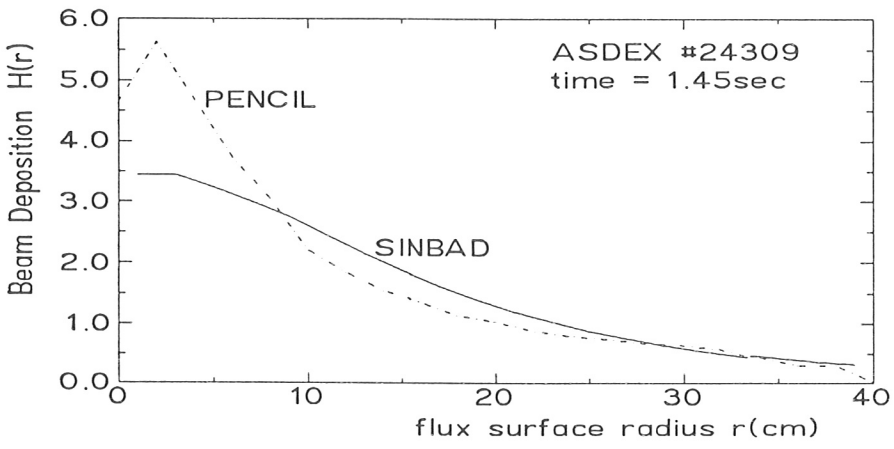

FIG. 4.5: *Comparison of the deposition profiles from PENCIL and SINBAD.*

Comparisons of SINBAD with TRANSP and PENCIL have been carried out for the JET tokamak. FIGURE 4.6 shows some calculated deposition profiles from the different codes.

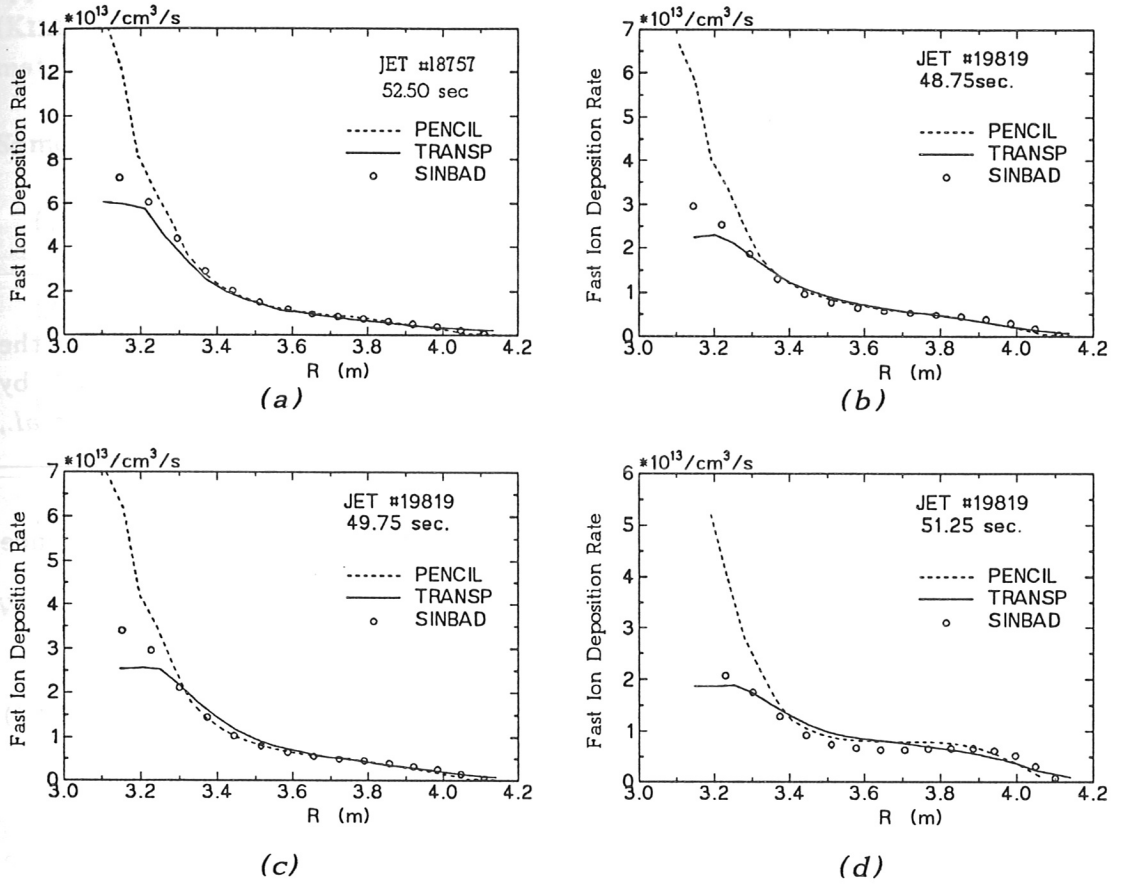

FIG. 4.6: *Comparisons of the results from SINBAD with those from TRANSP and PENCIL for JET discharges.*

The calculations show that the results from SINBAD agree with those from TRANSP, but slight differences remain, which are considered to be due mostly to differences in treatment of the flux surface geometry or different ionization cross sections used in the two codes. The differences in the plasma center are suspected to be due to statistical fluctuations of the Monte Carlo calculations. On the other hand, as also pointed out by CORRIGAN (1992), the PENCIL code calculates a fast ion density in the plasma center which is up to a factor of 2 higher.

PART II

5. SLOWING-DOWN PROCESSES

5.1 Fokker-Planck Equation

The fast ion thermalization process through Coulomb collisions with the background plasma can be treated classically. This has been confirmed by experimental observations (CORDEY, *et al.*, 1975; GOLDSTON, 1975; KAITA, *et al.*, 1985; HEIDBRINK, *et al.*, 1988).

The equation which describes the evolution of a particle species in the presence of neutral particle beam injection is the Fokker-Planck equation:

$$\frac{\partial f_a}{\partial t} + \boldsymbol{v} \cdot \frac{\partial f_a}{\partial \boldsymbol{r}} + \frac{\boldsymbol{F}}{m_a} \cdot \frac{\partial f_a}{\partial \boldsymbol{v}} = \left(\frac{\partial f_a}{\partial t}\right)_c + S_a + L_a. \tag{5.1.1}$$

Here f_a is the distribution function in a six-dimensional phase space for the heating particle species, S_a is the source term for the injected particles, $(\partial f_a/\partial t)_c$ is the collision term, and L_a contains loss terms. The Fokker–Planck collision term for an inverse-square force was derived by ROSENBLUTH *et al.* (1957) in the form

$$\frac{1}{\Gamma_a}\left(\frac{\partial f_a}{\partial t}\right)_c = -\frac{\partial}{\partial v_i}\left(f_a \frac{\partial h_a}{\partial v_i}\right) + \frac{1}{2}\frac{\partial^2}{\partial v_i \partial v_j}\left(f_a \frac{\partial^2 g_a}{\partial v_i \partial v_j}\right), \tag{5.1.2}$$

where $\Gamma_a = 4\pi Z_a^4 e^4/m_a^2$; furthermore, h_a and g_a are the *Rosenbluth potentials*, which are given by

$$h_a = \sum_b \frac{m_a + m_b}{m_b}\left(\frac{Z_b}{Z_a}\right)^2 \ln\Lambda_{ab} \int f_b(\boldsymbol{v}')\,|\boldsymbol{v} - \boldsymbol{v}'|^{-1}\, d\boldsymbol{v}', \tag{5.1.3}$$

$$g_a = \sum_b \left(\frac{Z_b}{Z_a}\right)^2 \ln\Lambda_{ab} \int f_b(\boldsymbol{v}')\,|\boldsymbol{v} - \boldsymbol{v}'|\, d\boldsymbol{v}', \tag{5.1.4}$$

where $ln\Lambda_{ab}$ is the Coulomb logarithm for interacting species *a* and *b*.

Solving the seven-dimensional partial differential equation for a tokamak configuration is impracticable.Therefore simplifications are required. For specific applications, several methods based on different assumptions were developed (KILLEEN, *et al.*, 1968; CORDEY, 1976). For toroidally confined plasmas, the mathematical models are summarized in KILLEEN et al. (1986).

Sometimes the following assumptions can be made:

(1) The perpendicular drifts caused by the magnetic field inhomogeneity are negligibly small as compared with the thermal velocity.

(2) Since the slowing-down times are much larger than the time scale of the gyro-motion, the Fokker-planck equation can be gyro-phase averaged.

(3) The fast ions are slowed down through collisions with Maxwellian background particles. The interactions between fast particles themselves are neglected.

(4) The system is in a steady state.

With the above assumptions, the Fokker-Planck equation becomes

$$\frac{\partial f_a}{\partial t} = \left(\frac{\partial f_i}{\partial t}\right)_c + S_a + L_a = 0. \tag{5.1.5}$$

The Fokker-Planck collision term is given by

$$\left(\frac{\partial f_a}{\partial t}\right)_c = \frac{1}{v^2}\left[-\alpha v^2 f_a + \frac{1}{2}\frac{\partial}{\partial v}\left(\beta v^2 f_a\right)\right] + \frac{\gamma}{4v^2}\frac{\partial}{\partial \mu}\left[\left(1-\mu^2\right)\frac{\partial f_a}{\partial \mu}\right], \tag{5.1.6}$$

where $\mu=cos\vartheta$ is the pitch angle cosine of the ion velocity relative to the magnetic field line. The coefficients α, β and γ are given by

$$\begin{aligned} \alpha &= \langle \Delta v_{\parallel} \rangle + \frac{1}{2v}\langle (\Delta v_{\perp})^2 \rangle , \\ \beta &= \langle (\Delta v_{\parallel})^2 \rangle , \\ \gamma &= \langle (\Delta v_{\perp})^2 \rangle \end{aligned} \tag{5.1.7}$$

and describe the slowing-down, diffusion and pitch-angle scattering. The source term S_a in equation (5.1.5) is given by

where $S_i(\mu)$ is the local deposition rate of monoenergetic particles with the velocity v_i. The deposition rate is usually calculated through beam deposition codes, e.g. SINBAD.

WOLLE (1990) developed a computer code to solve the simplified 2D Fokker-Planck equation numerically. There, the distribution function is expanded in Legendre polynomials which are eigenfunctions of the pitch-angle scattering operator

$$f_a(v,\mu) = \sum_{n=0}^{\infty} a_n(v)\, P_n(\mu). \tag{5.1.9}$$

The expansion series is cut off at an order which gives a sufficient accuracy. The corresponding coefficients $a_n(v)$ are determined according to appropriate boundary conditions.

5.2 Relaxation Time Model

The injected particles can initially be represented by a delta-function in energy space. Colliding with the bulk plasma they transfer energy to the cold plasma. If collisions with injected particles are neglected, the initial energy loss can be described by (HÜBNER *et al.*, 1985; 1988)

$$E(t) = E_0 \exp\left(-\frac{t}{\tau_w}\right), \tag{5.2.1}$$

where E_0 and $E(t)$ are the injection energy and the average energy of the fast particles at a time t. The energy relaxation time τ_w can be written (TRUBNIKOV, 1956) as

$$\frac{1}{\tau_w} = \frac{2}{\tau_s} - \frac{1}{\tau_D} - \frac{1}{4\,\tau_E}\,, \tag{5.2.2}$$

where τ_s, τ_D and τ_E are defined as

$$\tau_s = -\frac{v}{\langle \Delta v_{\parallel} \rangle}, \qquad \tau_D = \frac{v^2}{\langle (\Delta v_{\perp})^2 \rangle},$$
$$\tau_E = \frac{E^2}{\langle (\Delta E)^2 \rangle} = \frac{1}{4}\frac{v^2}{\langle (\Delta v_{\parallel})^2 \rangle}, \qquad \tau_w = -\frac{E}{\langle \Delta E \rangle}. \tag{5.2.3}$$

The slowing-down time τ_s characterizes the dynamic friction. The characteristic times τ_D and τ_E, i.e. deflection time and energy exchange time, describe the diffusion of the particles in velocity space and the energy diffusion, which tends to expand the energy spectrum of the monoenergetic ions.

If particle loss mechanisms only occur for energies comparable to the kinetic energies of the background particles, the distribution, $F_a(E)$ can be determined by the particle conservation equation

$$\frac{\partial F_a}{\partial t} + \frac{\partial}{\partial E}\left(F_a \frac{dE}{dt}\right) = \sum_{i=1}^{3} S_i(E)\, \delta(E-E_i) \qquad (\zeta k T_e < E \leq E_1), \tag{5.2.4}$$

where the coefficient ζ sets up an energy limit to any possible particle loss mechanisms. With equation (5.2.1) we can rewrite equation (5.2.4) as

$$\frac{\partial F_a}{\partial t} = \frac{\partial}{\partial E}\left(F_a \frac{E}{\tau_w}\right) + \sum_{i=1}^{3} S_i(E)\, \delta(E-E_i) \qquad (\zeta k T_e < E \leq E_1). \tag{5.2.5}$$

In steady state, the distribution function $F_a(E)$ can immediately be calculated by integrating equaton (5.2.5):

$$F_a(E) = \frac{\tau_w}{E} \sum_{i=1}^{3} S_i(E_i)\, \sigma(E-E_i) \qquad (\zeta k T_e < E \leq E_1), \tag{5.2.6}$$

where

$$\sigma(E-E_i) = \begin{cases} 1, & \zeta k T_e < E \leq E_i, \\ 0, & E > E_i \end{cases}$$

5.3 Consistency of the Two Models

With

$$F_a(E) = 4\pi \frac{v}{m_a} \left[\frac{1}{2} \int_{-1}^{+1} f_a \, d\mu \right] \tag{5.3.1}$$

and assuming that $\beta = 0$, i.e. $\tau_E = \infty$, one finds that the Fokker-Planck collision term (5.1.6) reduces to the diffusion term in equation (5.2.5). Therefore, the two models are identical if $\tau_E = \infty$.

It is clear that the application of the relaxation time model is restricted to plasma conditions with a large energy-exchange time or, more precisely, to plasmas where the ratio $4\tau_E/\tau_w$ (s. equation 5.2.2) is large. In order to determine the plasma parameters for which equation (5.2.6) can provide a reliable result, a comparison of the two different models for different plasma conditions as shown in FIG.5.1

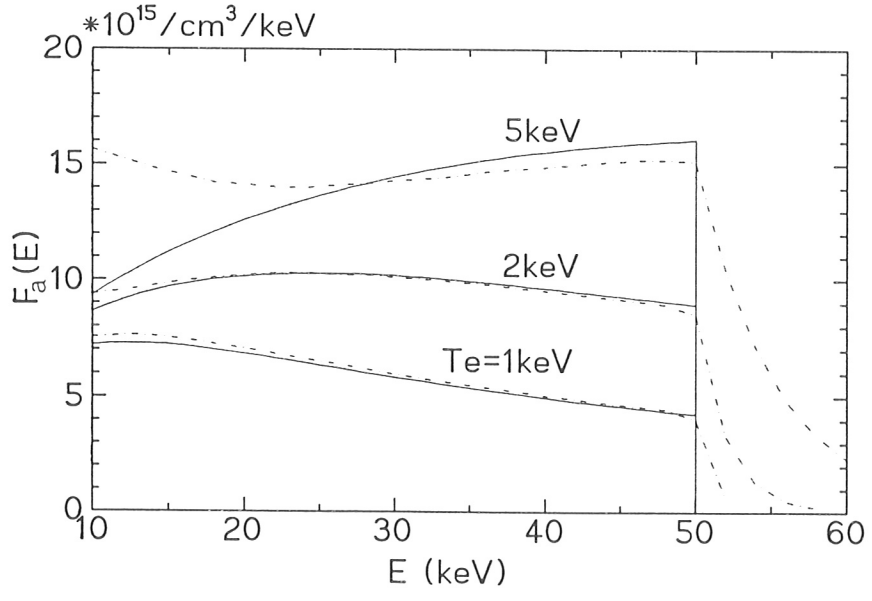

FIG.5.1 *Comparison of simulations of the slowing-down process using different models.*
(———) Relaxation time model, (— · — · —) Fokker-Planck model
Injected particle: Deuteron, Injection energy: 50 keV,
Deposition rate: $10^{19}/m^3/s$, Plasma density $5.*10^{19}/m^3$,
Plasma composition: $D^+ : H^+ : O^{8+} = 0.85 : 0.1 : 0.05$,
Plasma temperature: $T_e = T_i = 1, 2, 5$ keV.

was made. For the selected test particle, there is no great discrepancy between the two models as long as the plasma temperature is smaller than about *2 keV*. As the plasma temperature increases above *5 keV*, the energy exchange time τ_E becomes smaller and comparable to the energy relaxation time τ_w. In order to achieve an accuracy of better that *10%*, the ratio $4\tau_E/\tau_w$ should be kept larger than *10*, roughly estimated.

Since both τ_E and τ_w are inversely proportional to the plasma density, the ratio $4\tau_E/\tau_w$ is only a function of the plasma temperature and the energy of the fast ion, as shown in FIG. 5.2.a and FIG. 5.2.b.

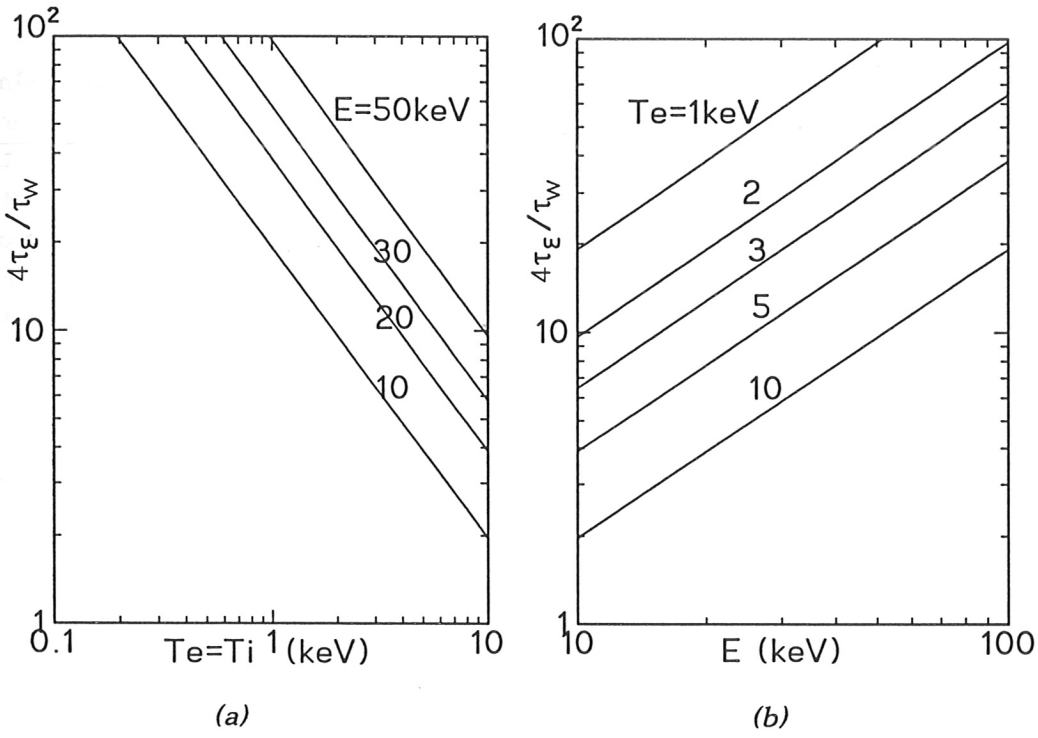

FIG. 5.2 *Dependence of the ratio $4\tau_E/\tau_w$ on the plasma temperatures and energy of the slowing-down particles.*

As seen above, if the energy of the fast particles is fixed, the ratio $4\tau_E/\tau_w$ increases with decreasing plasma temperature. This indicates that the relaxation time model is restricted to relatively cold plasmas. On the other hand, for a given plasma temperature, the simple model cannot be used to follow the particles down to an energy comparable to the mean kinetic energy of the bulk

For ASDEX plasmas with typical temperatures of less than *2 keV*, the beam particles can be precisely followed down to an energy of about *10 keV* by using the simple relaxation time model (BOMBA, 1989; WOLLE, 1990). The high energy tail predicted by the Fokker-Planck equation can be neglected in these cases due to the small number of the fast ions involved.

5.4 Energy Transfer Analysis

The plasma is a mixture of electrons, hydrogen isotopes and impurity ions. Once an ion population with high energy is present in the plasma, energy is transfered to each background particle species through collisions. As a consequence, the energetic particles are slowed down. The analysis of the energy transfer rates to different particle species determines which particle species are the most important ones for the slowing-down processes of the beam particles. The implications for simulations can be considerable because the slowing-down processes depend on a large amount of plasma quantities some of which may lack reliable measurements.

As discussed above, the energy loss rate of the beam particles can be characterized by the energy relaxation time τ_w, which consists of the contributions of all particle species involved in the plasma. It is given by

$$\frac{1}{\tau_w} = \sum_i \frac{1}{\tau_w^i}, \tag{5.4.1}$$

where τ_w^i is the contribution to the energy relaxation by the particle species i. The fraction of the power lost to the particle species i is τ_w/τ_w^i. The total power absorbed by species i, P_i is then given by

$$P_i = \int_{\zeta k T_e}^{E_1} \frac{\tau_w}{\tau_w^i} \frac{dE}{dt} F_a(E)\, dE. \tag{5.4.2}$$

Using the relaxation time model, one obtains

$$P_i = \sum_{j=1}^{3} S_j(E_j) \int_{\zeta k T_e}^{E_j} \frac{\tau_w}{\tau_w^i}\, dE. \tag{5.4.3}$$

Equation (5.4.3) is a simple integration of τ_w/τ_w^i, which is a function of the plasma temperature and the energy of the fast particle as illustrated in FIG. 5.3. Here, the plasma has been assumed to consist of an ion mixture of *85%* deuterons, *10%* hydrogen and *5%* oxygen. FIGURE 5.3.a shows the energy fraction transferred to different particle species for various plasma temperatures. There, the energy of the fast particle is chosen to be *50 keV*. FIGURE 5.3.b shows how the energy transfer of the fast particles changes as they are slowing down in a given plasma. Here, it is assumed that the velocity of the fast particle is much larger than the mean velocities of the background ions and much smaller than the mean velocity of electrons. Both figures indicate a tendency that, as the velocity of the fast ions approaches the mean thermal velocity of one species, the energy exchange between them become more effective.

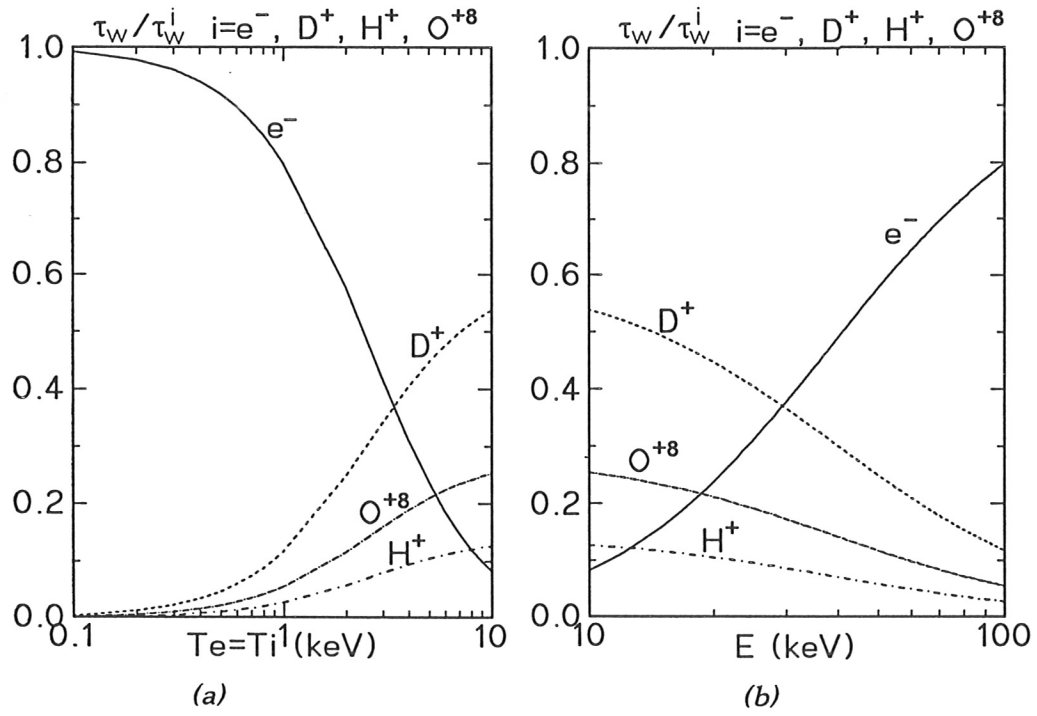

FIG. 5.3 *Analysis of the energy transfer to different particle species.*
(a) Energy loss fractions versus plasma temperature. Energy of the fast deuterons is chosen to be 50 keV.
(b) Energy loss fractions versus energy of the fast deuterons. It is assumed that the plasma temperature is 2 keV (T_e=T_i).

For the beam particles injected with an energy of *50 keV* into a plasma with a temperature lower than *2 keV,* collisions of the fast particles with electrons dominate the energy transfer mechanisms. This is the typical situation for ASDEX plasmas. Because the local electron temperature and density are measured rather accurately, the low temperature plasma is a favorable choice to investigate the behavior of particles slowing down. This is discussed in the next section.

PART III

6. Simulations of The Relevant Diagnostics at ASDEX

Neutral particle beam injection is very successful for plasma heating and current drive. A further exploited potential of the neutral particle beam is application for plasma diagnostic measurements. Two typical diagnostics which rely on neutral beam injection are charge-exchange recombination spectroscopy and the neutral particle analyzer. Charge-exchange reactions between the injected neutrals and the background ions lead to radiation emission which can be measured, and information about the thermal plasma ions, such as temperature and density, can be deduced from the emission spectroscopy. Moreover, charge exchange between a beam particle and a background ion leads to birth of a 'hot' ion and a 'cold' atom. Analysis of the energy distribution of the detected neutrals gives information about the ion temperature.

Apart from the diagnostics based on the charge-exchange process, there are some diagnostic signals that sensitively respond to the fast particle energy distribution, such as those of the plasma pressure and neutron production. Due to their high energy, the injected particles, even if their number is much smaller than that of the background particles, considerably contribute to these signals. Since the reactivity of two fusing nuclei strongly depends on their relative energy, the neutrons arising from the nuclear reactions between the fast particles and the bulk plasma may dominate the total neutron production. Therefore, both diagnostics may be used to investigate the behavior of the fast particles, and thus to test the theories developed in the preceding sections.

Since it is impossible to deduce a beam deposition profile from the two global measurements, the test has to be carried out by means of simulations. Even so, difficulty remains since both signals depend on fast ion energy distributions which are related to many plasma quantities. Some of the quantities may even lack reliable measurements. The uncertainties in these quantities may completely cover over the effects of the deposition profile on both signals. Therefore, in order to investigate the effects caused by the beam deposition profile, we have to choose appropriate plasma conditions or introduce appropriate methods to minimize the effects caused by other quantities.

6.1 Neutron Rate

The global neutron rate can be determined by a neutron counter. Before comparing theoretical calculations with measurements, first we have to discuss the neutron production process in order to select suitable plasma conditions. The local neutron rate depends not only on the velocity distribution of the fast ions but also on the distributions of the background particles. The velocity distribution of the background particles of each species is usually considered to be a Maxwellian. Thus, only macroscopic parameters such as the density and temperature are required. The electron density and temperature can be well measured, but the densities and temperatures of ion species are not well measured quantities. Therefore, the effects of the background ions on the neutron rate should be reduced.

The local neutron rate Q_{ab}, arising from the nuclear reaction between two fusing species with velocity distributions $f_a(v_a)$ and $f_b(v_b)$, is given by

$$Q_{ab} = \frac{1}{1+\delta_{ab}} \iint \sigma_{ab}\, |v_a - v_b|\, f_a(v_a)\, f_b(v_b)\, dv_a dv_b \tag{6.1.1}$$

with $$\delta_{ab} = \begin{cases} 1, & a=b \\ 0, & a \neq b \end{cases}$$

where σ_{ab} is the corresponding cross section. For the plasma investigated at ASDEX, deuterium is usually used. Thus, in this work, only the *D-D* reaction will be discussed.

It is helpful to separate the reacting deuterons into two groups, i.e. the thermal background (a Maxwellian distribution) and the nonthermal fast deuterons arising from the beam. Equation (6.1.1) can thus be written as

$$Q = Q_{tt} + Q_{bt} + Q_{bb}$$

with

$$\begin{aligned} Q_{tt} &= \frac{1}{2} \iint \sigma\, |v_t' - v_t|\, f_t(v_t')\, f_t(v_t)\, dv_t' dv_t\,, \\ Q_{bt} &= \iint \sigma\, |v_t - v_b|\, f_t(v_t)\, f_b(v_b)\, dv_t dv_b\,, \\ Q_{bb} &= \frac{1}{2} \iint \sigma\, |v_b' - v_b|\, f_b(v_b')\, f_b(v_b)\, dv_b' dv_b\,, \end{aligned} \tag{6.1.2}$$

where $f_t(v_t)$ and $f_b(v_b)$ are distribution functions of the thermal background and fast deuterons, respectively. Furthermore, Q_{tt}, Q_{bt} and Q_{bb} are the thermal,

be averaged over the thermal particles. This yields

$$Q_{bt} = \frac{1}{2} n_{dt}^2 \langle \sigma v \rangle_{tt} , \tag{6.1.3}$$

$$Q_{bt} = n_{dt} \int \langle \sigma v \rangle_t F_b(E)\, dE , \tag{6.1.4}$$

where n_{dt} and $F_b(E)$ are the density of the thermal deuterons and the energy distribution of the fast ions. Furthermore, $\langle \sigma v \rangle_{tt}$ and $\langle \sigma v \rangle_t$ are the thermal reactivity and the reactivity between monoenergetic ions and the thermal ions. As expected, the former is only a function of the ion temperature, while the latter depends on both the ion temperature and the fast ion energy, as shown in FIG. 6.1.1.

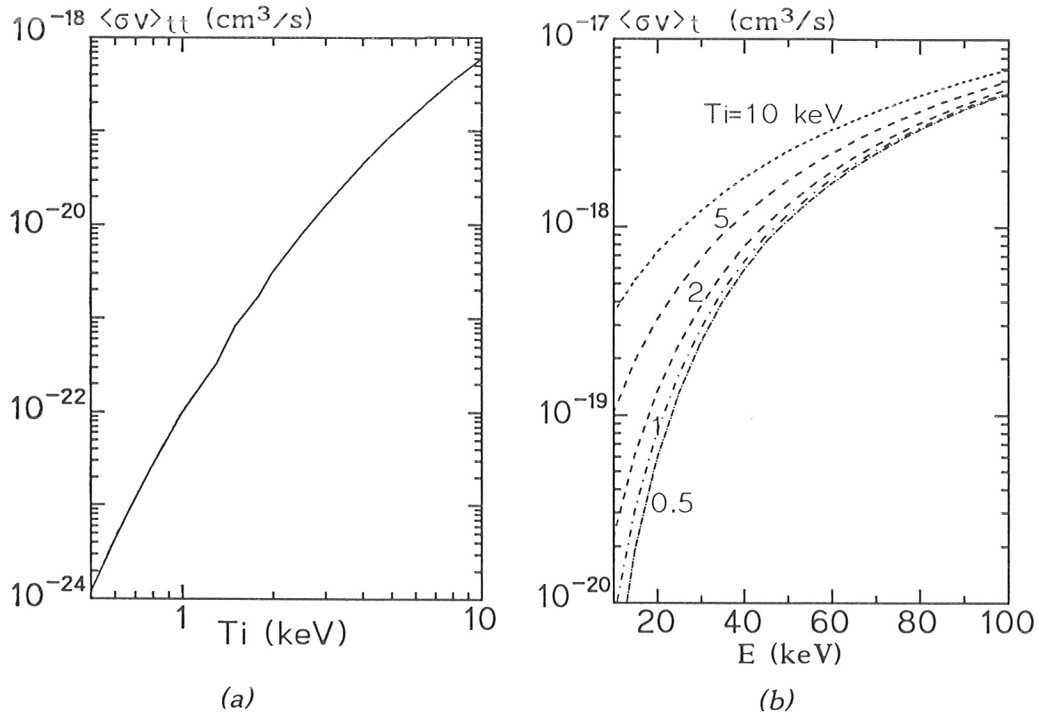

FIG. 6.1.1 *Reactivities*

(a) Thermal reactivity $\langle \sigma v \rangle_{tt}$ versus T_i.

(b) $\langle \sigma v \rangle_t$ versus the energy of the fast particles for different ion temperatures.

Here, the relevant cross section of the D–D reaction is taken from Bosch (1992). Since the cross section of the nuclear fusion strongly depends on the relative energy of the two reacting nuclei, a small variation of the ion temperature leads to a large change in the thermal reactivity. On the other hand, since the fast ion energy is usually much greater than the mean energy of the thermal ions,

$\langle\sigma v\rangle_t$ depends more strongly on the fast ion energy than on the ion temperature, except at high ion temperature, for which the mean thermal velocity of the thermal ions is comparable with that of the fast ions. For ion temperatures lower than *1 keV*, the dependence of $\langle\sigma v\rangle_t$ on T_i can be neglected. In addition, FIG. 6.1.1.b shows that if there are, for instance, beam particles injected with an energy of *50 keV* into a plasma with an ion temperature somewhat lower than *2 keV*, most of the neutrons resulting from the beam-thermal reactions are produced just initially after the birth of the fast ions. After having slowed down to half of their initial energy, the contribution of the fast ions to the neutron production is negligibly small.

If the fast ion velocity is much greater than the thermal velocity of the ions, the dependence of the energy relaxation time τ_w on the ion temperature can be neglected. Thus, the product of the energy distribution function and the electron density $n_e F_b(E)$ is a function of the electron temperature and the fast ion energy only. The fast ion distribution at low electron temperatures can be obtained from the relaxation time model. In this case, $\langle\sigma v\rangle_t$ can be averaged over the fast ion distribution. One thus gets

$$Q_{bt} = n_{dt} n_{db} \langle\sigma v\rangle_{bt}, \tag{6.1.5}$$

where n_{db} and $\langle\sigma v\rangle_{bt}$ are, respectively, the beam particle density and the beam-

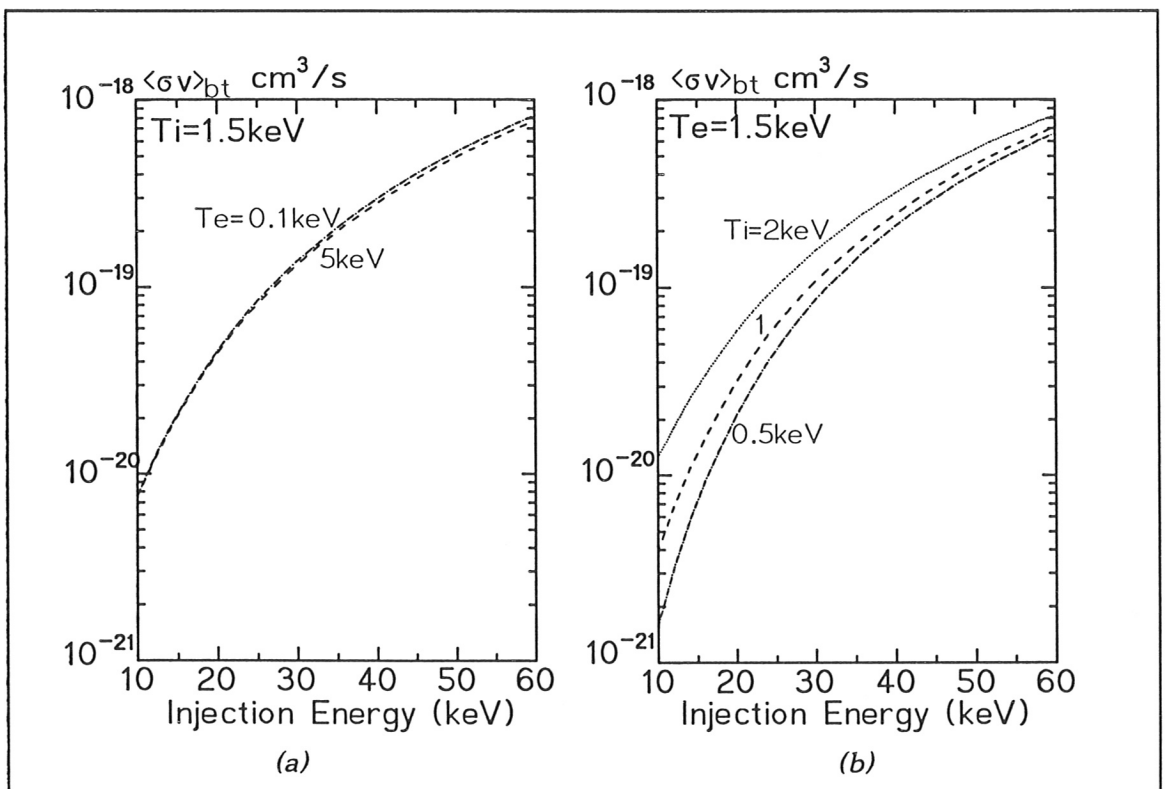

thermal reactivity, which is a function of the injection energy of the beam particle and the electron and ion temperatures, as shown in FIG. 6.1.2.

Since the fast ion distribution functions for different electron temperatures are roughly constant in the energy range relevant to neutron production (s. FIG. 5.1), $\langle\sigma v\rangle_{bt}$ depends very weakly on the electron temperature, as illustrated in FIG. 6.1.2.a. By contrast, if the electron temperature is given, the beam-thermal reactivity responds to the change of ion temperature, especially at low injection energy, as shown in FIG. 6.1.2.b. The reason for this is that the reaction cross section strongly depends on the relative energy of two reacting nuclei. Thus, either a rise in the temperature of the background ions or an increase of the injection energy of the beam particles leads to an increase of the relative energy and, consequently, to an increase of their mean reactivity. If the injection energy of the beam particles is much greater than the thermal energy of the background ions, the dependence on the ion temperature is negligible.

Comparing the thermal reactivity $\langle\sigma v\rangle_{tt}$ (s. FIG. 6.1.1.a) with the beam-thermal reactivity $\langle\sigma v\rangle_{bt}$, as shown in FIG. 6.1.2, the thermal reactivity is two orders of magnitude smaller than the beam-thermal reactivity as long as the ion temperature is somewhat lower than $2\ keV$ and the energy of the beam particle is greater than $40\ keV$. This means that even a small amount of beam particles may produce a dominant amount of neutrons.

Following the discussion of the thermal and the beam-thermal reactivities, the beam-beam neutron rate Q_{bb} can also be written as

$$Q_{bb} = \frac{1}{2} n_{db}^2 \langle\sigma v\rangle_{bb} , \tag{6.1.6}$$

where $\langle\sigma v\rangle_{bb}$ is the beam-beam reactivity. In keeping with the injector geometry, the velocity distribution of the beam particles is anisotropic. The beam-beam reactivity depends on the pitch angles of the velocities of the fast ions relative to the magnetic field line. For a given injector geometry, the initial velocity distribution of the fast ions can be calculated exactly. During the slowing-down process, the fast ions are deflected through collisions with the background particles. Nevertheless, the diffusion in velocity space can initially be neglected because the deflection time is large as compared with the energy relaxation time. As the fast ions are slowed down to the low energy region, the diffusion in velocity space becomes considerable, but its influence on the mean reactivity is also small due to the low energy. With this assumption, one can estimate the beam-beam reactivity with the energy distribution of the fast ions, taking the initial velocity distribution into account. The results for the particles injected into ASDEX plasmas are illustrated in FIG. 6.1.3. Unlike the beam-thermal

reactivity, the beam-beam reactivity does not depend on the ion temperature, but somewhat on the electron temperature.

Both the beam-thermal and the beam-beam reactivities are of the same order at a moderate ion temperature and more than two orders of magnitude greater than the thermal reactivity for injection energies of more than *40 keV*.

So far, the reactivities have been discussed in detail. The remaining parameter to be discussed is the beam particle density n_{db}, which is completely determined by the distribution function $F_b(E)$. Since, for a given injection energy component E_j, the resulting fast ion

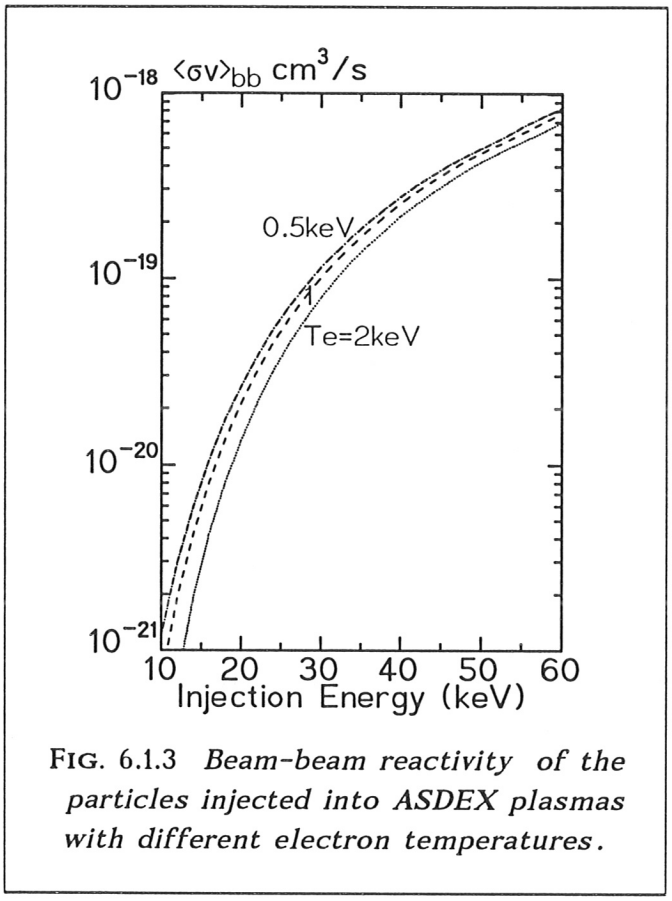

FIG. 6.1.3 *Beam-beam reactivity of the particles injected into ASDEX plasmas with different electron temperatures.*

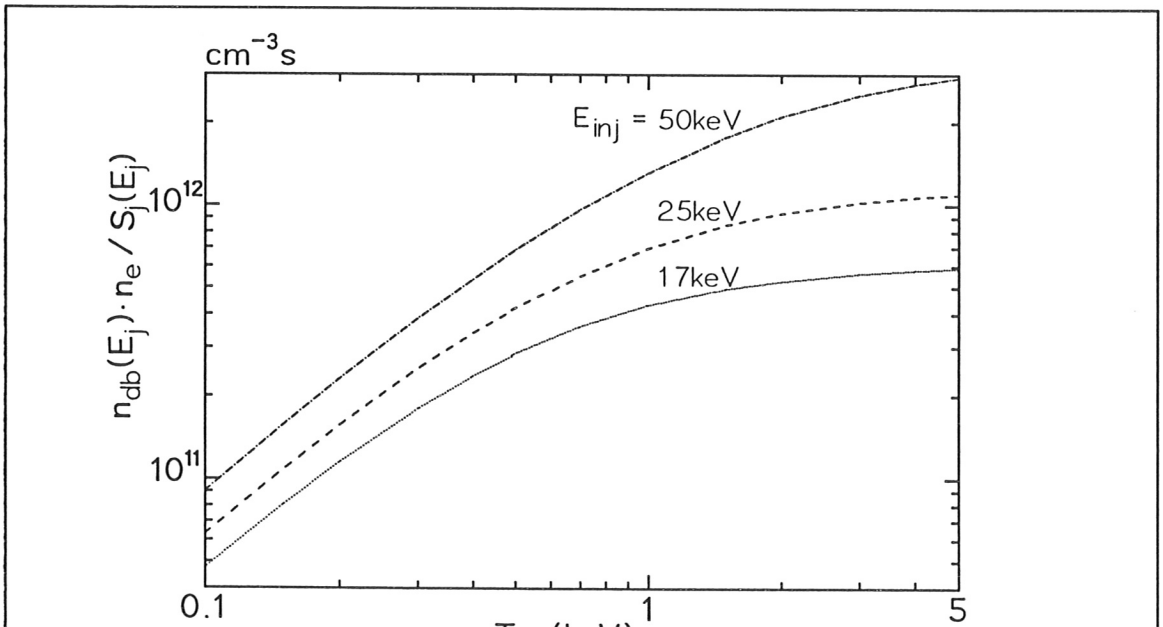

density $n_{db}(E_j)$ is proportional to the deposition rate $S_j(E_j)$ and inversely proportional to the electron density n_e, only the quantity $n_e \cdot n_{db}(E_j)/S_j(E_j)$ needs to be calculated. As shown in FIG. 6.1.4, it is a function of the electron temperature and injection energy. It is found that, for low electron temperatures and high injection energies, the fast ion density strongly depends on the electron temperature because collisions with electrons dominate the slowing-down process. As the electron temperature increases, collisions with ions become more important and thus the increase in the fast ion density with the electron temperature becomes smaller. For typical ASDEX plasmas, the beam ion density is very small as compared with the background ion density. As an example, it is assumed that deuterons with a full energy of *50 keV* and a power of *1 MW* are injected into a high purity deuterium plasma with a density of $0.5*10^{14}$ $/cm^3$ and a temperature of *2 keV* ($T_e=T_i$). If the shine-through is neglected, the average fast ion deposition rate is about $2.4*10^{13}$ $/cm^3/s$. Here, the plasma volume is assumed to be $5.2*10^6$ cm^3. According to FIG. 6.1.4, the fast ion density is estimated to be $2*10^{12}$ $/cm^3$, i.e. only *4%* of the background ion density.

If the fast deuteron density n_{db} is known, the thermal deuteron density n_{dt} can be obtained from the total deuteron density n_d. Assuming a neutral plasma with a mixture of deuterium, hydrogen and impurity ions with charge Z_x, one has

$$\frac{n_d}{n_e} = \frac{Z_x - Z_{eff}}{Z_x - 1}\left(1 + \frac{n_h}{n_d}\right)^{-1}, \tag{6.1.7}$$

where n_h is the hydrogen density and Z_{eff} is the effective charge, defined as

$$Z_{eff} = \frac{1}{n_e}\left(n_d + n_h + n_x Z_x^2\right). \tag{6.1.8}$$

Equations (6.1.3), (6.1.5) and (6.1.6) can now be rewritten as

$$Q_{tt} = \frac{1}{2}\left(n_e \frac{Z_x - Z_{eff}}{Z_x - 1}\left(1 + \frac{n_h}{n_d}\right)^{-1} - \sum_{j=1}^{3} n_{db}(E_j)\right)^2 \langle \sigma v \rangle_{tt}, \tag{6.1.9}$$

$$Q_{bt} = \left(n_e \frac{Z_x - Z_{eff}}{Z_x - 1}\left(1 + \frac{n_h}{n_d}\right)^{-1} - \sum_{j=1}^{3} n_{db}(E_j)\right)\sum_{j=1}^{3} n_{db}(E_j) \langle \sigma v \rangle_{bt}, \tag{6.1.10}$$

$$Q_{bb} = \frac{1}{2}\left(\sum_{j=1}^{3} n_{db}(E_j)\right)^2 \langle \sigma v \rangle_{bb}. \tag{6.1.11}$$

Note that $n_{db}(E_j)$ for a given injection energy is a function of the electron density, electron temperature and deposition rate $S_j(E_j)$. Finally, it is found that the total

local neutron rate Q is a complicated function of the parameters n_e, n_h/n_d, E_j, $S_j(E_j)$, T_i, T_e, Z_{eff} and Z_x. In order to investigate the influence of the fast ion deposition rate $S_j(E_j)$ on the neutron production, it is necessary to minimize the effects caused by other plasma quantities by an appropriate choice of the plasma conditions.

As discussed above, the thermal neutron rate strongly depends on the ion temperature. This means that, for sufficiently low ion temperature, the contribution of the thermal ions to the total neutron production can be neglected. On the other hand, the beam-beam neutron rate is proportional to the square of the beam particle density, which can be sensitively reduced by lowering the beam injection power. The beam-beam neutron rate can be left out of account as long as the beam particle density n_{db} is kept at a few per cent of the target ion density. In this case, the total local neutron rate is approximately given by

$$Q \approx Q_{bt} \approx \frac{Z_x - Z_{eff}}{Z_x - 1}\left(1 + \frac{n_h}{n_d}\right)^{-1} n_e \sum_{j=1}^{3} n_{db}(E_j) \langle \sigma v \rangle_{bt}(T_i, E_j). \tag{6.1.12}$$

Since the quantity $n_e \cdot n_{db}(E_j)/S_j(E_j)$ is only a function of T_e and E_j, we define $n_e \cdot n_{db}(E_j)/S_j(E_j) = \Upsilon(T_e, E_j)$ as given in FIG. 6.1.4. Thus, equation (6.1.12) can be rewritten as

$$Q \approx Q_{bt} \approx \frac{Z_x - Z_{eff}}{Z_x - 1}\left(1 + \frac{n_h}{n_d}\right)^{-1} \sum_{j=1}^{3} \Upsilon(T_e, E_j)\, S_j(E_j) \langle \sigma v \rangle_{bt}(T_i, E_j). \tag{6.1.13}$$

If deuterium is the dominant ion species in the plasma, Z_{eff} is usually much smaller than the charge number of the impurity ion and, furthermore, the ratio n_h/n_d is a small quantity. As shown in FIG. 6.1.2, the beam-thermal reactivity around an injection energy of *50 keV* only weakly depends on the ion temperature. Although the influence of the ion temperature becomes important for the particles injected with lower energy components, i.e. half and one-third of the injection energy, they, however, make no appreciable contributions to the total neutron production because of their small energy. According to the above discussion, it is found that the dominant parameters in equation (6.1.2) are T_e, E_1 and $S_j(E_j)$. The injection energy E_1 can easily be accurately measured. The electron temperature is considered to be one of a few quantities which can be well measured in the plasma. Therefore, a cold plasma with a low density of fast ions is an appropriate choice for investigating the deposition behavior of

$$Q_{tot} \approx \int \frac{Z_x - Z_{eff}}{Z_x - 1} \left(1 + \frac{n_h}{n_d}\right)^{-1} \sum_{j=1}^{3} Y(T_e, E_j)\, S_j(E_j) \langle \sigma v \rangle_{bt}(T_i, E_j)\, dV, \qquad (6.1.14)$$

where Q_{tot} is the global neutron rate.

According to equation (6.1.14), the global neutron rate Q_{tot} depends indirectly on the plasma density through the local fast ion deposition rate $S_j(E_j)$. For injection into plasmas with different densities, the beam particle deposition in the plasma will change. It is expected that the neutron counters should respond to the changes of the local deposition rates. In order to demonstrate this effect clearly, the following two points should be taken into account:

(1) The local deposition rate $S_j(E_j)$ should sensitively respond to the change of the plasma density. Because of the large orbit-losses for counter injected particles, counter-injection is preferred to co-injection for this purpose.

(2) The electron temperature should be kept constant in order to minimize the effect caused by the change in electron temperature.

Here, two ASDEX discharges which are suited to the investigation of the deposition properties of neutral particles injected into tokamak plasmas are presented. During the discharges, deuterium atoms with a full energy of *51 keV* were counter-injected into deuterium plasmas with central electron temperatures of about *1 keV*. The measured relevant plasma parameters, such as the electron temperature, ion temperature, electron density, *Z*-effective and injection power, are plotted in FIG. 6.1.5. Here, the electron temperature, density and Z_{eff} were taken from the Thomson scattering system, which consists of *16* spatial channels. This is capable of providing profile measurements every *17* milliseconds. The central ion temperatures were deduced from the energy spectra of the escaped atoms.

In both discharges selected, the electron density increases during the neutral particle beam injection. The development of the fast ion deposition profile in time as obtained from the SINBAD code is illustrated in FIG. 6.1.6. Since over *90%* of the neutrons are produced by the beam particles with the full energy, only the deposition profiles for the particles with the full energy are shown. In both cases, the deposition profiles are sensitive to changes in the plasma density. As the plasma density increases, more and more injected neutrals are ionized or undergo charge exchange in the region near the plasma boundary, and fewer neutrals reach the plasma center. Thus, the local deposition rates in the plasma center decreases with increasing plasma density. But, once the penetrated atoms become charged in a plasma region near the outside boundary of the torus, they drift towards the inside of the torus and will be driven out of the plasma and lost. Although, as the plasma density is increasing, more and more neutrals will be ionized in the outside region, few of them can be confined. As a consequence,

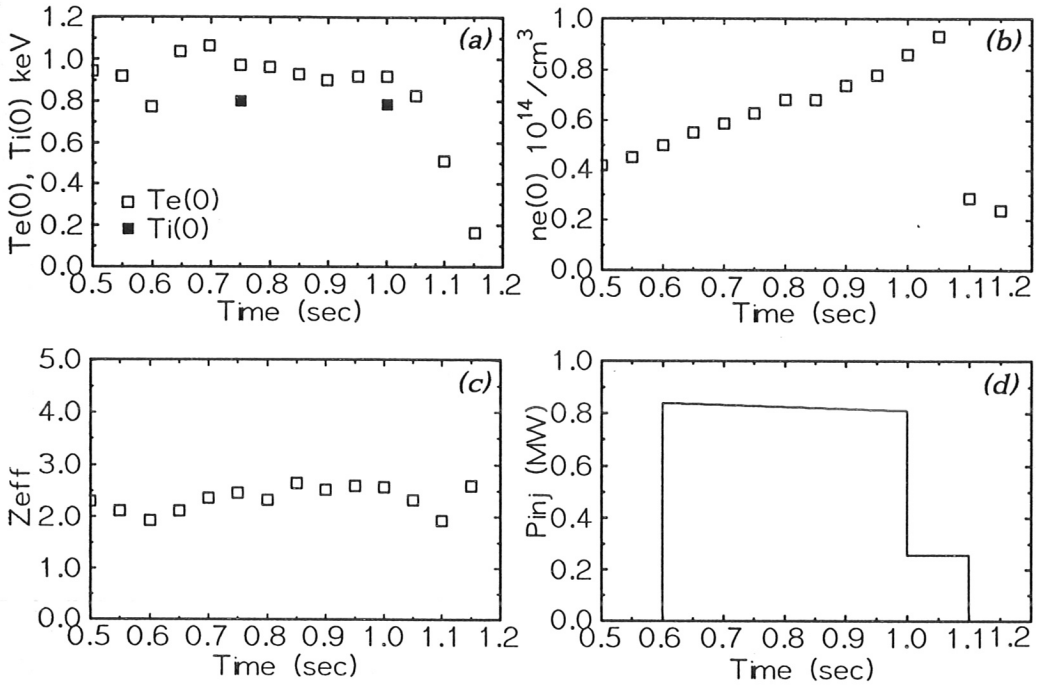

(a) ASDEX shot #25581

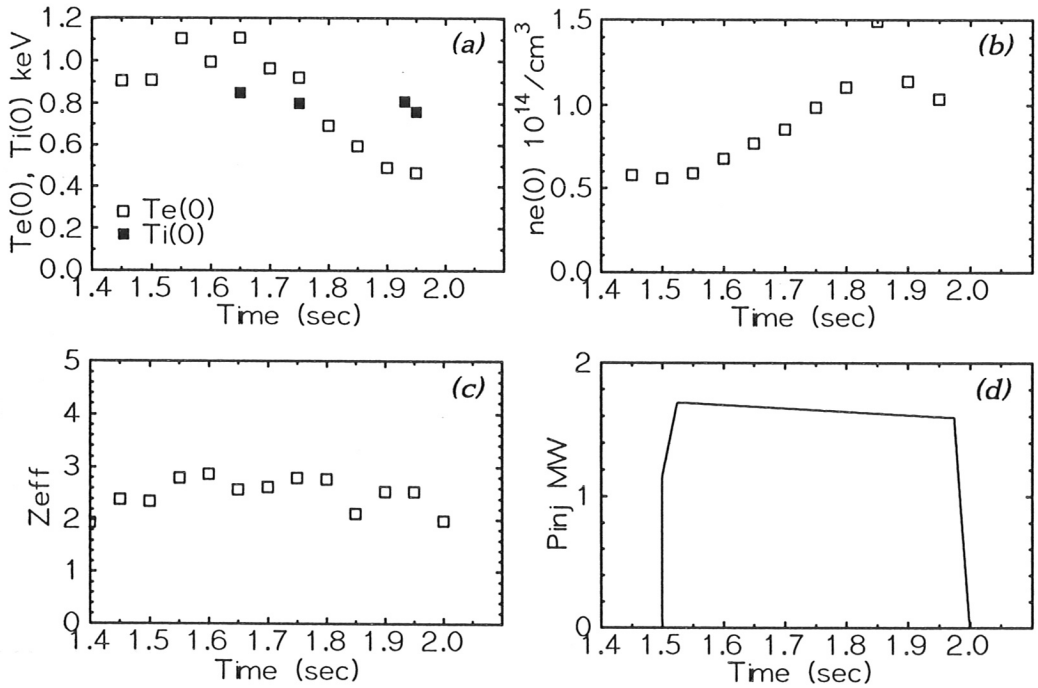

(b) ASDEX shot #25595

FIG. 6.1.5 *Evolution of some relevant parameters for ASDEX shots #25581 and #25595*

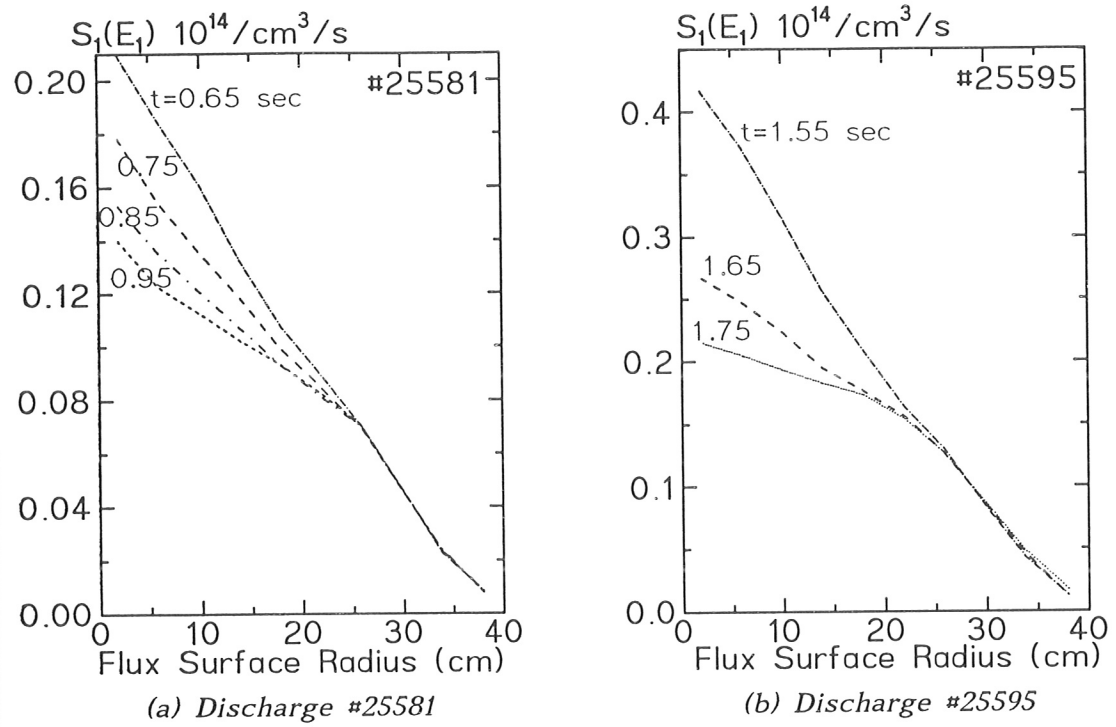

(a) Discharge #25581 *(b) Discharge #25595*

FIG.6.1.6 *Temporal evolution of deposition profiles for ASDEX discharges #25581 and #25595.*

the local deposition rates in the outside region of the plasma do not increase very much with increasing plasma density.

The number of particles lost through orbit effects in the two discharges is very considerable. Because of the high plasma density and its flat profile, most of the injected neutrals are stripped in the outside region of the torus. As they are moving towards the inside, the drift motion of their guiding centers caused by the inhomogeneity of the toroidal magnetic field drives them from the flux surfaces on which they are born, away into the outside plasma region. Although most of them are not trapped by the magetic mirror effect because of the small injection angles with respect to the toroidal magetic field lines, the passing particles follow drift orbits which are displaced from the flux surfaces by over *5 cm*. This is large enough to drive the ions born outside the the flux surface with the radius of *30 cm*, out of the plasma, when drifting to the inside of the torus. In both discharges discussed, more than *30%* of the injected particles are lost after their first revolutions around the torus. As the plasma density increases, even more particles drift out of the plasma. This is the main reason why counter-injection is less favorable than co-injection for heating tokamak plasmas.

The strong decrease of the deposition rate in the plasma center predicts a drop in the local neutron rate. Due to the limitation of the neutron counter at ASDEX, the evolution of the local neutron rates cannot be observed. Fortunately, due to

the peaked electron temperature profile, most of neutrons are produced in the inside plasma region, where the deposition rates change. Therefore, the global neutron rate measured by the neutron counter should respond to these changes. This is shown in FIG. 6.1.7, where the global neutron rate clearly decreases with decreasing deposition rates. It was taken that $n_h/n_d=0.13$ for both discharges so that the absolutely measured neutron rates agree with the calculated ones.

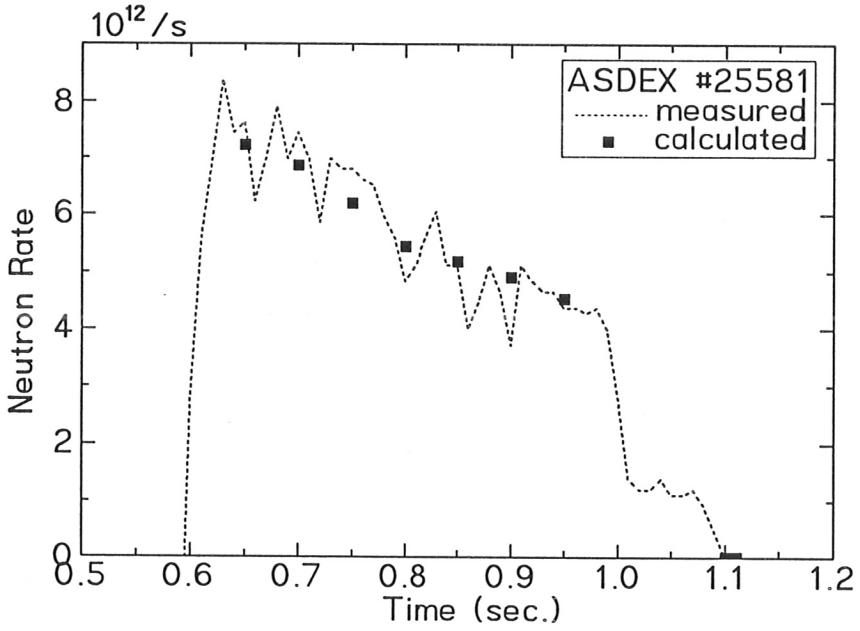

(a)

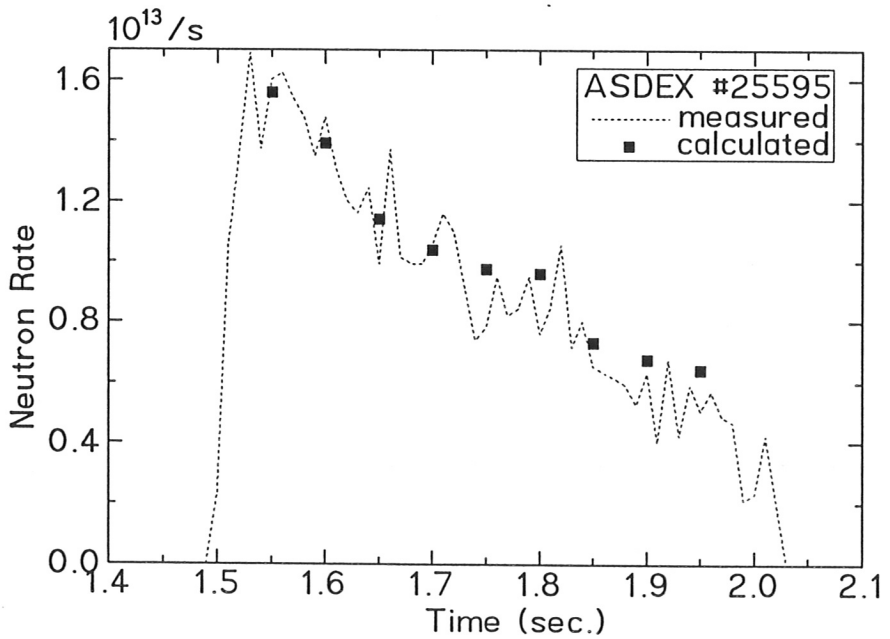

In discharge #25581, the continuous decrease of the neutron rate is mainly due to the decrease of the fast ion deposition rates in the plasma center, since the change of the electron temperature during beam injection is negligibly small. In discharge #25595, the initial rush drop of the global neutron rate in the neutral beam heating phase is caused by the strong decrease of the neutral particle deposition rates in the inside plasma region, due to the increase of the plasma density. As the central electron density increases above $\sim 10^{14}$ cm^{-3} after about *1.7 s*, the electron density profile becomes more peaked. As a result of the peaking of the density profile together with the increasing central density, the fast ion deposition profiles do not change very much. Thus, after *1.7 s*, the moderate decrease of the neutron rate is caused by the relatively strongly decreasing electron temperature.

It should be mentioned that the effects of the plasma rotation on the beam deposition profile and neutron production were not taken into account in the calculations. Plasma rotation will give rise to a decrease of the relative velocity between a beam particle and a background particle, and consequently, an increase in the ionization cross section of the injected neutrals and a decrease in the beam-thermal reactivity. Whether the increase in the ionization cross section leads to a more peaked or a broader deposition profile than that without plasma rotation depends on the rotation velocity and the electron density profiles. This change in beam deposition profile should give rise to a change in the neutron rate. However, this effect should be much smaller than that caused by the change in beam-thermal reactivity since the beam-thermal reactivity relies more strongly than the ionization cross section of the neutrals on the relative energy. Therefore, one should first neglect the change in beam deposition profile.

In order to make it clear whether the decreases of the global neutron rates in both discharges are possibly due to increases in the rotation velocities, we first estimate the rotation velocity according to the fit formula obtained by KALLENBACH (1990) by analysis of a number of D→D counter-NI discharges at ASDEX. The central rotation velocity for discharge *#25581* is $1.63*10^5$ *m/s* at *0.65 s* and, due to the increasing plasma density, is reduced to $1.25*10^5$ *m/s* at *0.95 s*. For discharge *#25595*, the central rotation velocities are $2.98*10^5$ *m/s* at *1.55 s* and $2.45*10^5$ *m/s* at *1.70 s*. The decreases in the rotation velocities in the two discharges should give rise to some increases in the neutron rates and, to some extent, moderate the effect caused by the increasing plasma densities. However, this is not observed. Moreover, if one simply estimates the neutron rate in the rotating plasma coordinate system, one finds that the the neutron rate in discharge *#25595*, due to the double rotation velocity responding to the double injection power, should be considerably smaller than twice the neutron rate in discharge *#25581*. However, this is not observed by the neutron counters either. Therefore, it is considered that the effect of plasma rotation on neutron production should be much smaller than that predicted by the simple consideration. A reliable explanation remains to be given.

6.2 Diamagnetic Flux Measurement

In a tokamak configuration, the plasma is kept in equilibrium by magnetic fields. The condition

$$\nabla P = j \times B \tag{6.2.1}$$

relates the plasma pressure to the magnetic field configuration. If the plasma pressure changes, the magnetic field has to be adjusted in such a way that the pressure-balance equation (6.2.1) is satisfied. Any change of the magnetic field will induce an electric field, which can be measured by setting a probe coil along the induced electric field lines. Since it is not possible to introduce probes into a fusion plasma, the loop has to be mounted poloidally on the vacuum vessel, surrounding the whole torus (GERNHARDT, *et al.*, 1986). Therefore, we have to average the pressure-balance equation (6.2.1) throughout the whole poloidal cross section. When the curvature of the toroidal magnetic field line is neglected, according to MUKHOVATOV and SHAFRANOV (1971) we have

$$\langle P_\perp \rangle = \frac{1}{2\mu_o} \left[B_p^2(a) - 2B_{t,coil}(R_0) \frac{\delta \Phi_t}{\pi a^2} \right], \tag{6.2.2}$$

where $\langle P_\perp \rangle$, $B_p(a)$ and $B_{t,coil}(R_0)$ are the transverse plasma pressure averaged over the poloidal cross section, the poloidal magnetic field at the plasma boundary and the toroidal magetic field in the plasma center, produced by just the toroidal field coils. Furthermore, $\delta \Phi_t$ is the diamagnetic flux of the toroidal magnetic field in the plasma column, defined as

$$\delta \Phi_t = \pi a^2 \langle B_t(R) - B_{t,coil}(R_0) \rangle , \tag{6.2.3}$$

where the pointed brackets again denote averaging over the whole plasma column cross section. The physical meaning of $\delta \Phi_t$ can be found if one assumes a toroidal magnetic field configuration without plasma and toroidal current in which $\delta \Phi_t = 0$. Once the plasma is set up, the kinetic pressure and plasma current appear such that the toroidal magnetic field has to be adjusted to keep the plasma in equilibrium. Thus, the diamagnetic flux $\delta \Phi_t$ occurs, which can be determined by integrating the induced voltage on the diamagnetic loop. Measuring the diamagnetic flux $\delta \Phi_t$ allows the average transverse plasma pressure $\langle P_\perp \rangle$ to

$$\beta_P = \frac{\langle P_\perp \rangle}{B_P^2(a)/2\mu_o}. \tag{6.2.4}$$

Replacing $\langle P_\perp \rangle$ by β_P, one can rewrite equation (6.1.2) as

$$\beta_P = 1 - 2\frac{B_{t,coil}(R_o)}{B_P^2(a)}\frac{\delta\Phi_t}{\pi a^2}. \tag{6.2.5}$$

Because $B_{t,coil}(R_o)$ and $B_P(a)$ are well-known quantities, beta poloidal can be determined directly by measuring the diamagnetic flux. Assuming a Maxwellian plasma in which the plasma pressure is isotropic, we replace $\langle P_\perp \rangle$ by $\langle P \rangle_t$. Thus, the global energy content E_c can be obtained directly from β_P:

$$E_c = \frac{3}{2}\langle P \rangle_t V = \frac{3}{2}\beta_P \frac{B_P^2(a)}{2\mu_o} V, \tag{6.2.6}$$

where V is the total plasma volume. As a fast diagnostic tool, the diamagnetic loop is usually used to observe the time development of the plasma energy confinement property during a discharge with different operation regimes. Since the diamagnetic measurement is based on the pressure-balance condition, a stationary or a quasi-stationary state is necessary for a reliable result.

In the OH regime (ohmic heating), β_P usually has small values due to the poor energy content sustained by the ohmic heating. Additional heating improves the plasma energy content and, consequently, gives rise to an increase of β_P. Particularly in the presence of neutral particle beam injection, both the rising of the plasma temperature and the fast particle population drive the plasma to a high energy content level. Because of their high energy, the fast particles, in spite of their small number, play a dominant role. These nonthermal particles contribute an anisotropic term, $\langle \boldsymbol{P}_B \rangle$, to the plasma pressure, given by

$$\langle \boldsymbol{P}_B \rangle = \begin{pmatrix} \langle P_{\parallel B} \rangle & 0 & 0 \\ 0 & \langle P_{\perp B} \rangle & 0 \\ 0 & 0 & \langle P_{\perp B} \rangle \end{pmatrix}, \tag{6.2.7}$$

where $\langle P_{\perp B} \rangle$ and $\langle P_{\parallel B} \rangle$ are the pressure components perpendicular and parallel to the toroidal magnetic field line. Thus, equation (6.2.6) has to be rewritten as

$$E_c = \left[\frac{3}{2}\langle P \rangle_t + \langle P_{\perp B} \rangle + \frac{1}{2}\langle P_{\parallel B} \rangle \right] V, \tag{6.2.8}$$

where $\langle P \rangle_t$ is an isotropic pressure contributed by the background particles of Maxwellian distributions. Since the diamagnetic signal only responds to the

transverse plasma pressure, i.e.

$$\langle P_\perp \rangle = \langle P \rangle_t + \langle P_{\perp B} \rangle, \tag{6.2.9}$$

the energy content

$$E_c = \left[\frac{3}{2} \langle P \rangle_\perp + \frac{1}{2} \left(\langle P_{\parallel B} \rangle - \langle P_{\perp B} \rangle \right) \right] V \tag{2.8.10}$$

cannot be determined by the diamagnetic signal alone without a knowledge of $\langle P_{\perp B} \rangle$ and $\langle P_{\parallel B} \rangle$. Therefore, theoretical calculations are required. If the local distribution of the fast particles, $f_b(\varkappa, \upsilon, \mu)$, is known, where $\varkappa$, υ and μ are the normalized flux surface radius and the velocity and pitch angle of the fast particle, $\langle P_{\perp B} \rangle$ and $\langle P_{\parallel B} \rangle$ can be calculated by

$$\langle P_{\perp B} \rangle = 2\pi \int_0^1 \int_0^\infty \int_{-1}^{+1} \frac{1}{2} m_b \upsilon^2 (1-\mu^2)\, \upsilon^2 f_b(\varkappa, \upsilon, \mu)\, d\mu\, d\upsilon\, d\varkappa^2, \tag{6.2.11}$$

$$\langle P_{\parallel B} \rangle = 2\pi \int_0^1 \int_0^\infty \int_{-1}^{+1} m_b \upsilon^2 \mu^2\, \upsilon^2 f_b(\varkappa, \upsilon, \mu)\, d\mu\, d\upsilon\, d\varkappa^2, \tag{6.2.12}$$

with

$$2\pi \int_0^\infty \int_{-1}^{+1} \upsilon^2 f_b(\varkappa, \upsilon, \mu)\, d\mu\, d\upsilon = n_b(\varkappa), \tag{6.2.13}$$

where $n_b(\varkappa)$ is the local density of the fast particles. According to WOLLE (1990), the fast partice distribution can be expanded in Legendre eigenfunctions $P_n(\mu)$ as

$$f_b(\varkappa, \upsilon, \mu) = \sum_{n=0}^{\infty} a_n(\varkappa, \upsilon)\, P_n(\mu). \tag{6.2.14}$$

With

$$\mu^2 = \frac{1}{3} \left(P_0 + 2P_2 \right), \tag{6.1.15}$$

$$1 - \mu^2 = \frac{2}{3} \left(P_0 - P_2 \right), \tag{6.2.16}$$

$$\int_{-1}^{+1} P_m(\mu)\, P_n(\mu)\, d\mu = \frac{2}{2m+1} \delta_{mn}, \tag{6.2.17}$$

and inserting equation (6.2.14) into equations (6.2.11) and (6.2.12) , one obtains

$$\langle P_{\perp B} \rangle = \frac{4\pi}{3} m_b \int_0^1 \int_0^\infty \left[a_0(\varkappa, \upsilon) - \frac{1}{5} a_2(\varkappa, \upsilon) \right] \upsilon^4\, d\upsilon\, d\varkappa^2, \tag{6.1.18}$$

$$\langle P_{\parallel B} \rangle = \frac{4\pi}{3} m_b \int_0^1 \int_0^\infty \left[a_0(x,v) + \frac{2}{5} a_2(x,v) \right] v^4 \, dv dx^2 , \qquad (6.1.19)$$

where the coefficients $a_0(x,v)$ and $a_2(x,v)$ can be obtained from the NRFPS code calculations.

The relative fractions of $\langle P_{\perp B} \rangle$ and $\langle P_{\parallel B} \rangle$ depend on the beam injection geometry and the beam and plasma parameters. In keeping with the small injection angles of the beams at ASDEX, the ratio $\langle P_{\perp B} \rangle / \langle P_{\parallel B} \rangle$ is small. For deuterons with an energy of *50 keV* injected into plasmas with linearly averaged densities of $2 \sim 5 * 10^{13} / cm^3$, the ratio $\langle P_{\perp B} \rangle / \langle P_{\parallel B} \rangle$ takes an initial value in the range of *0.35~0.4*, in accordance with the fast ion birth deposition. Since most of the fast ions are born in the outside region of the torus, as they drift towards the inside region, the parallel energy component will be partly converted into the transverse energy component in order to conserve the total energy and magnetic moment (see section 2.6). As a consequence, $\langle P_{\perp B} \rangle / \langle P_{\parallel B} \rangle$ increases from the initial range up to a range of *0.45~0.50*, in accordance with the orbit-averaged deposition.

The transverse pressure $\langle P_{\perp B} \rangle$ contributed by the fast particles can be deduced from the diamagnetic signal and, consequently, compared with theoretical calculations. In order to figure out the contribution of the fast particles, it is necessary to set an offset line to eliminate the background introduced by the thermal particles from the preceding OH phase. This can be done because of the linear relation of the diamagnetic signal to the plasma pressure. We thus have

$$\langle P_{\perp B} \rangle_{dia} = \Delta \langle P_\perp \rangle_{dia} - \sum_i \Delta \langle n_i k T_i \rangle , \qquad (6.2.20)$$

where $\Delta \langle P_\perp \rangle_{dia}$ and $\Delta \langle n_i k T_i \rangle$ are the increase of the total transverse plasma pressure from ohmic heating to OH+NBI heating measured by the diamagnetic loop and the increase of the contributions of the thermal particles calculated according to other local diagnostics available, such as the Thomson scattering system, HCN-laser interferometer, ECE diagnostic and CX spectroscopy.

As examples, two $D \rightarrow D$ discharges are presented for investigation of the fast particle behavior. Prior to NB injection, ohmic heating sustained the plasmas to operate at center temperatures of *~1 keV* and center densities of $5 * 10^{13} / cm^3$ (*#28820*) and $6 * 10^{13} / cm^3$ (*#28821*), respectively, according to the Thomson scattering measurement. The neutral particle beams are fired at *0.95 s* in both cases. The penetration of fast deuterons with powers of *~1.5 MW* heat the plasmas up to *1.4 keV* in the plasma center. During NB injection, the electron densities in the plasma center are locked at about $4 * 10^{13} / cm^3$. In both discharges,

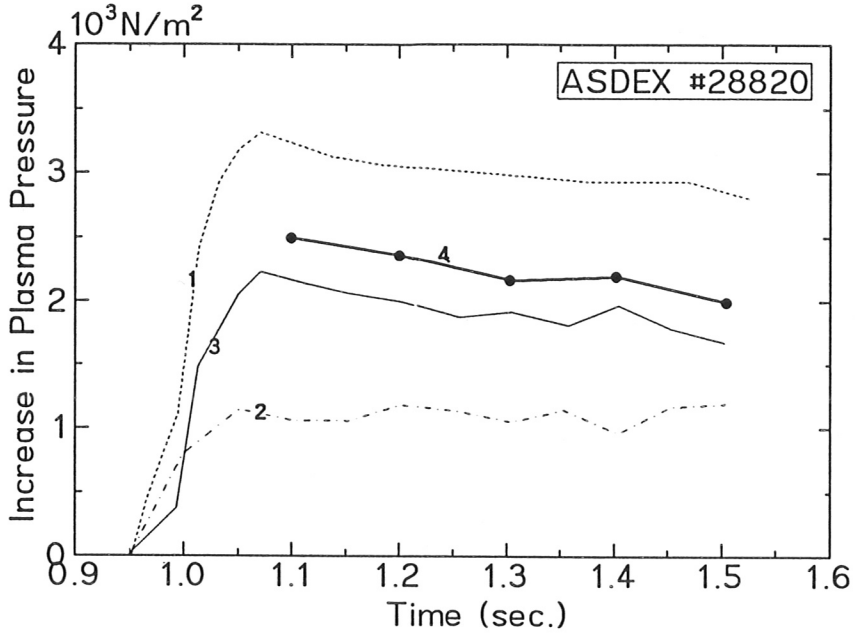

(a) ASDEX shot #28820

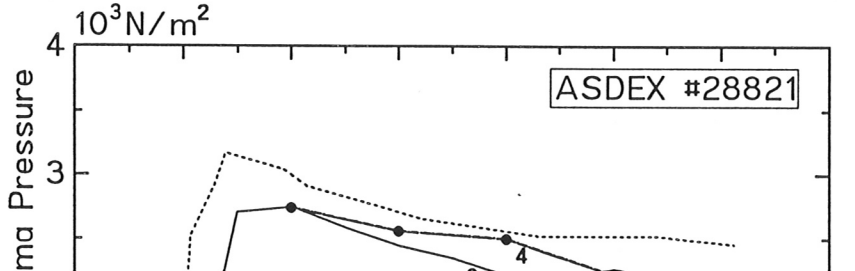

the increase of the plasma pressure from the OH regime to the OH+NBI regime is mainly caused by the fast particle population arising from the beam. Therefore, the plasma pressure contributed by the fast particles can be well derived from the diamagnetic flux measurement without a rather detailed knowledge of the thermal particles. The results are shown in FIG. 6.2.1 where the beam particle pressure deduced from the diamagnetic signal is compared with that calculated by the SINBAD+NRFPS package. Z_{eff} and the electron temperature and density profiles are measured by the Thomson scattering system. The ion temperature in the preceding OH phase is obtained from the neutron rate measured by the neutron counter, by assuming identical profile shapes for ions and electrons. In the NBI phase, the center ion temperature is determined by the neutral particle analyzer. Clearly, in FIG. 6.2.1, the increase of the plasma pressure is mainly due to the fast particle population in the plasma. Particularly in discharge *#28821*, owing to the decrease in plasma density, the increase of the thermal pressure from the OH to the OH+NBI regime is negligibly small with respect to the beam particle pressure. In this case, the diamagnetic loop serves as a sensitive detector of the fast particles.

Comparisons of the neutron rates calculated by NRFPS with those measured by the neutron counters for the two discharges indicate that the calculated neutron rates are about *20%* higher than the measured ones in both cases. The differences may be partly caused by the uncertainties in the deuteron density profile and n_h/n_d. For lack of reliable measurement, identical profiles were assumed for deuterons and electrons. The ratio n_h/n_d was taken to be *0.13.* With FIG. 6.2.1 together, it could be found that another error source could be the Thomson scattering system since the local electron parameters play important roles in both quantities involved.

As discussed in the previous sections, in current ASDEX plasmas, the collisions of fast particles with electrons dominate the slowing-down process. Apart from the neutron rate, in which the dominant beam-target neutron production is proportional to the density of the target ions, the average pressure of the fast particle is nearly independent of the thermal ions. This indicates that, on one hand, the diamagnetic loop is more suitable than the neutron counter for investigating the fast particle properties, and on the other hand, information about the thermal ions can hardly be deduced from the diamagnetic signals. Nevertheless, if a neutral beam with sufficiently high power is injected into a plasma with somewhat low density, the dominant ions may be heated to a temperature significantly exceeding that of the electrons. Due to the high ion temperature, the energy distribution of the fast ions will be strongly related to the thermal ion parameters. Owing to both the elevated ion temperature and the fast particle population, the dominant ion species will significantly contribute to the plasma pressure. This contribution can be well deduced from the diamagnetic signal since the contributions of other particle species are relatively small. Consequently, the ion density or temperature may be estimated through interpretation calculations.

PART IV

7. Neutron Emission Profile

In deuterium plasmas with deuterium injection, the local neutron rates are related directly to the local beam deposition rates. Therefore, a neutron emission profile is desirable to test the SINBAD calculations. Moreover, measurement of the neutron emission profile is of great importance since it includes information about the reacting ions.

Neutron emission profiles can be measured by using a number of collimated neutron counters viewing different plasma regions. For example, a large neutron measurement system is installed at the JET tokamak for this purpose (Marcus *et al.*, 1991). In this section it is shown how information about the neutron emission profile can be obtained from nuclear emulsion measurements.

In order to distinguish effectively the neutrons emitted from different plasma regions, an emulsion plate was positioned at ASDEX as close to the plasma as possible (position 6, Hübner, 1989). The arrangement is skeched in Fig. 7.1.1. The black solid circle indicates the plasma boundary, whereas the dotted ones give the shifted magnetic flux surfaces. The plate was exposed in a poloidal plane, ~*13 cm* outside close to the plasma boundary and with its axis oriented to the plasma center. The angle between the orientation axis and the median plane α_o is about *45* degrees.

7.1 Neutron Fluence

The problem starts with calculations of the neutron fluence at the position of the emulsion plate. In order to deduce the neutron emission profile from the proton tracks, we first investigate the effects caused by the neutrons from different plasma regions. The plasma is therefore divided into *10* subzones, as shown in Fig. 7.1.1. Because of the complex geometry of the problem, an analytical treatment of the angular distribution of the neutron fluence at the emulsion plate is not favorable. Instead, the problem is solved numerically. The calcula-

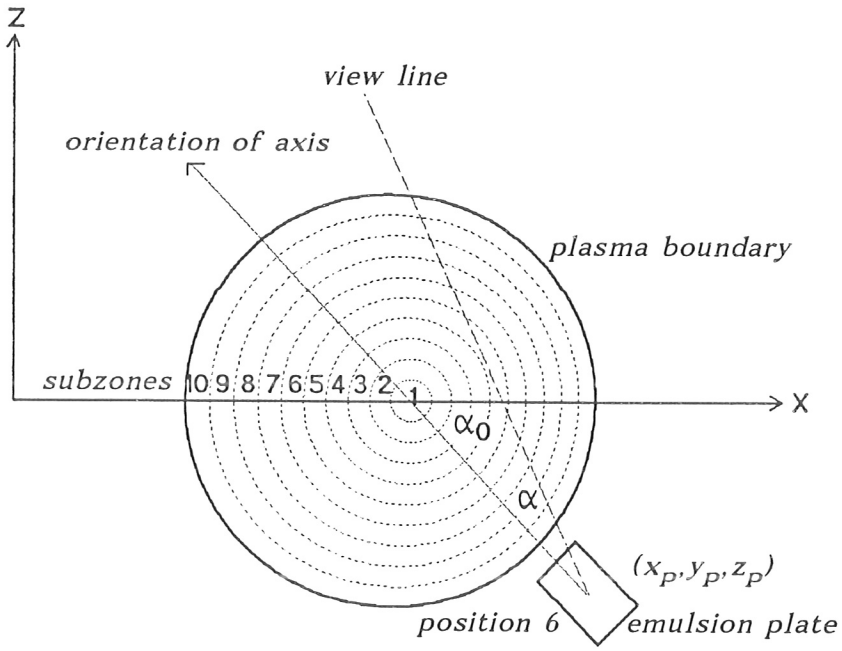

FIG. 7.1.1 *Side view of the emulsion plate arrangement.*

given by

$$\Delta N = \int \frac{Q(\varkappa)}{4\pi L^2}\, dx dy dz\,, \tag{7.1.1}$$

with

$$L^2 = (x-x_P)^2 + (y-y_P)^2 + (z-z_P)^2\,,$$

where $Q(\varkappa)$, $\varkappa$ and (x_P, y_P, z_P) are the emission profile, the normalized flux surface radius and the position of the emulsion plate, respectively. If $Q(\varkappa)$ is constant in each subzone, one has

$$Q(\varkappa) = \mathbb{C}_i\,, \qquad \varkappa_i - \tfrac{1}{2}\Delta\varkappa \le \varkappa \le \varkappa_i + \tfrac{1}{2}\Delta\varkappa \quad (i=1,10)\,, \tag{7.1.2}$$

where the flux surfaces $\varkappa_i - \frac{1}{2}\Delta\varkappa$ and $\varkappa_i + \frac{1}{2}\Delta\varkappa$ build up the boundaries of the i-th subzone. The angular distribution of the neutron fluence at the emulsion plate is given by

$$\frac{dN}{d\alpha\, d\beta} = \frac{\Delta N}{\Delta\alpha\Delta\beta} = \sum_{i=1}^{10} \mathbb{C}_i\, f_n^{\,i}(\alpha,\beta)\,. \tag{7.1.3}$$

Here, α and β are the poloidal and toroidal angles of a view line with respect to

the axis of the emulsion plate (s. FIG. 7.1.1). Furthermore, $f_n^i(\alpha,\beta)$ is the normalized angular distribution of the neutron fluence emitted from the i-th subzone and is completely determined by the flux surface positions and the geometric arrangement of the detector. If the flux surface geometry is known, $f_n^i(\alpha,\beta)$ can immedately be calculated without a knowledge of the emission profile. The flux surfaces in ASDEX plasmas are simple shifted circles and are described by equation (2.6.6) in section (2.6). The displacement of each flux surface center from the magnetic field axis is known as the *Shafranov shift*. The position of each flux surface center, (R_c,z_c), represented in the cylindrical coordinate system with the origin in the tokamak center, is given by

$$\begin{cases} R_c = R_0 + S_0\,(1-\varkappa^2)\ , \\ z_c = 0\ , \end{cases} \tag{7.1.4}$$

where R_0 and S_0 are the radius of the magnetic field axis and the *Shafranov shift* of the innermost flux surface. Thus, the circular flux surfaces are described by

$$(R-R_c)^2 + (z-z_c)^2 = a^2\varkappa^2\ . \tag{7.1.5}$$

Inserting equation (7.1.4) into equation (7.1.5) and transforming equation (7.1.5) into the Cartesian coordinates, one gets

$$\left[\sqrt{x^2+y^2} - R_0 - S_0\,(1-\varkappa^2)\right]^2 + z^2 = a^2\varkappa^2\ . \tag{7.1.6}$$

Thus, the flux surface radius is determined by

$$x_i - \frac{1}{2}\Delta x < x(x,y,z) \leq x_i + \frac{1}{2}\Delta x . \qquad (7.1.10)$$

Here, $(x_1,x_2,y_1,y_2,z_1,z_2)$ are the boundary conditions of the solid angle element $\Delta\alpha\Delta\beta$ described in the Cartesian coordinate system, given by

$$\begin{aligned} x_1 &= -(R_0 + a), & x_2 &= (R_0 + a), \\ z_1 &= z_P + (x_P - x)\tan(\alpha+\alpha_0), & z_2 &= z_P + (x_P - x)\tan(\alpha+\alpha_0+\Delta\alpha), \\ y_1 &= \sqrt{(x_P - x)^2 + (z_P - z)^2}\,\tan\beta, & y_2 &= \sqrt{(x_P - x)^2 + (z_P - z)^2}\,\tan(\beta+\Delta\beta). \end{aligned} \qquad (7.1.11)$$

The geometrical meanings of the boundary conditions are shown in FIG. 7.1.2.

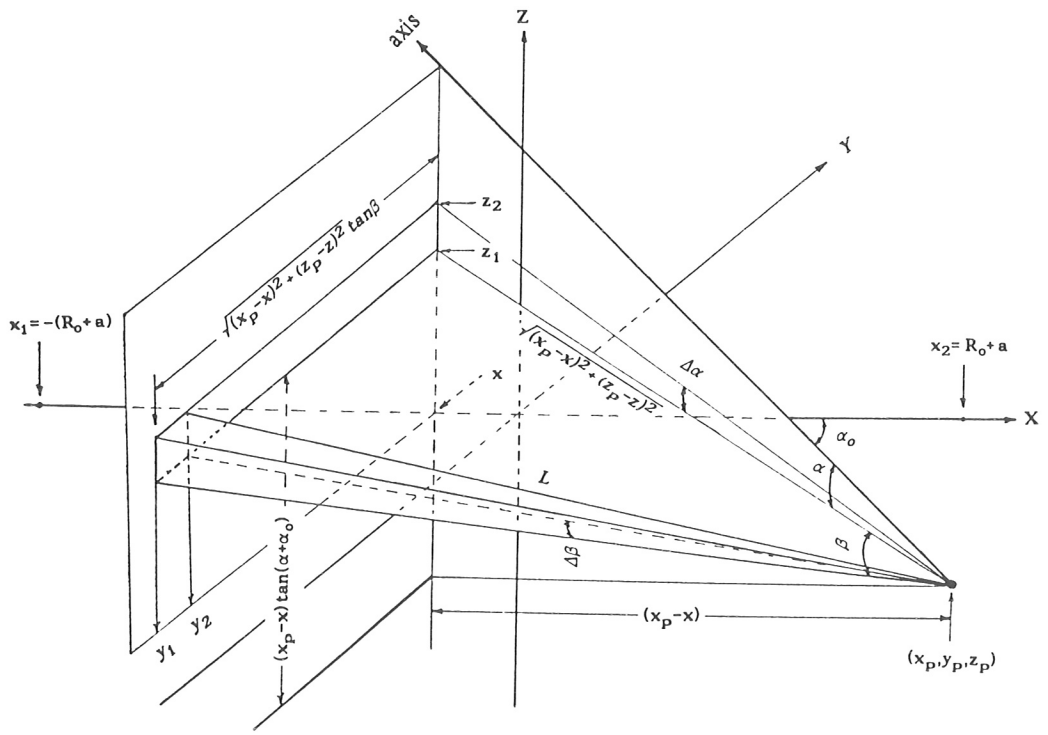

FIG. 7.1.2 *Transformation of the representation of the solid angle element from (L,α,β) to (x,y,z) coordinates.*

7.2 Response Function

In order to determine the response functions of the distribution of the recoil proton tracks, we introduce (ψ,φ), i.e. the plane and dip angles in the emulsion, to describe the orientation of the proton tracks (FIG.7.2.1). For neutrons with energies from E_n to E_n+dE_n and and incidence angles from (α,β) to $(\alpha+d\alpha,\ \beta+d\beta)$, the number of the protons which are scattered into $d\psi d\varphi$, $dP/d\psi d\varphi\, d\alpha d\beta dE_n$ is given by

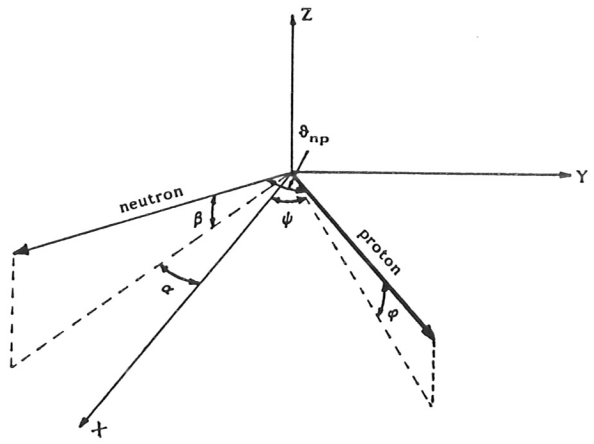

FIG.7.2.1 *Representation of the incidence angles of a neutron and the orientation of a proton track.*

$$\frac{dP(\alpha,\beta,E_n,\psi,\varphi)}{d\psi d\varphi\, d\alpha d\beta dE_n} = k\cos\varphi \frac{dN}{d\alpha\, d\beta} \cos\vartheta_{np}\, \sigma(E_n)\, n(E_n), \tag{7.2.1}$$

where the relation $d\Omega=\cos\varphi d\psi d\varphi$, the collision cross section $\sigma(E_n)$ and the energy spectrum of the incident neutrons $n(E_n)$ have been taken into account. The scattering angle ϑ_{np} is related to the other angles by

$$\cos\vartheta_{np} = \cos\beta\cos\varphi\cos(\alpha-\psi) + \sin\beta\sin\varphi\,. \tag{7.2.2}$$

The constant k in equation (7.2.1) is of no interest since no absolute quantities are involved in our problem. Adding up the contributions of all the neutrons with different incidence angles and energies from E_1 to E_2, one gets

$$\frac{dP(\psi,\varphi)}{d\psi d\varphi} = k\cos\varphi \iint \frac{dN}{d\alpha\, d\beta} \cos\vartheta_{np} \int_{E_1}^{E_2} \sigma(E_n)\, n(E_n)\, dE_n d\alpha d\beta$$

$$= \sum_{i=1}^{10} a_i \left[k \iint f_i \cdots \int_{E_1}^{E_2} \right] \tag{7}$$

where $f_p^i(\psi,\varphi)$ is the normalized response function of the distribution of the proton tracks from neutrons emitted in the subzone *i*. The lower and upper limits of the integration over neutron energy, E_1 and E_2, are determined according to a restriction in the proton energy. Since the longest proton tracks actually reflect the directions of the incident neutrons, it is necessary to set a lower energy limit to the recoil protons to eliminate the protons with large scattering angles. However, the number of the protons rapidly decreases with increasing energy limit. Thus, a reasonable energy range has to be chosen in order to suppress the statistical noise. If the lower energy limit to the protons, $E_{p,min}$, is selected, the neutron energy E_n is restricted to

$$E_1 = \frac{E_{p,min}}{\cos^2\vartheta_{np}} \leq E_n < E_2 = \infty \,. \tag{7.2.4}$$

The neutron spectrum $n(E_n)$, which can be deduced from the measured energy spectra of the recoil protons, is usually approximated by a Gaussian distribution:

$$n(E_n) \sim \exp\left[-\left(\frac{E_n - E_0}{\Delta E}\right)^2\right], \tag{7.2.5}$$

where E_0 and ΔE are the mean energy of the neutron arising from the *D–D* reaction and the half-width of the energy spectrum.

Because of the smallness of ΔE and the lower energy limit, the neutron energy varies only in a small range, where the collision cross section $\sigma(E_n)$ can be considered to be constant. Thus, from equation (7.2.3) one gets

$$f_p^i(\psi,\varphi) = k\,\sigma(E_0)\cos\varphi \iint f_n^i(\alpha,\beta)\cos\vartheta_{np} \int_{E_1}^{\infty} n(E_n)\,dE_n d\alpha d\beta \quad (i = 1, 10). \tag{7.2.6}$$

As seen in FIG. 7.1.1, the poloidal angle α will respond to the change of the neutron emission profile more effectively than the toroidal angle β. This is similar for ψ and φ. In addition, the plane angle ψ of the proton tracks can be measured more precisely than their dip angle φ. For these reasons, one should integrate $f_p^i(\psi,\varphi)$ over the dip angle φ in an appropriate range. This yields

$$F_p^i(\psi) = \int_{\varphi_1}^{\varphi_2} f_p^i(\psi,\varphi)\,d\varphi \qquad (i=1, 10). \tag{7.2.7}$$

However, in order to compare $F_p^i(\psi)$ with the measurements, the dip angle φ cannot be restricted too much because this would lead to only a very small number of proton tracks.

For the nuclear emulsion plate arrangement shown in FIG. 7.1.1, $f_p^i(\psi,\varphi)$ are

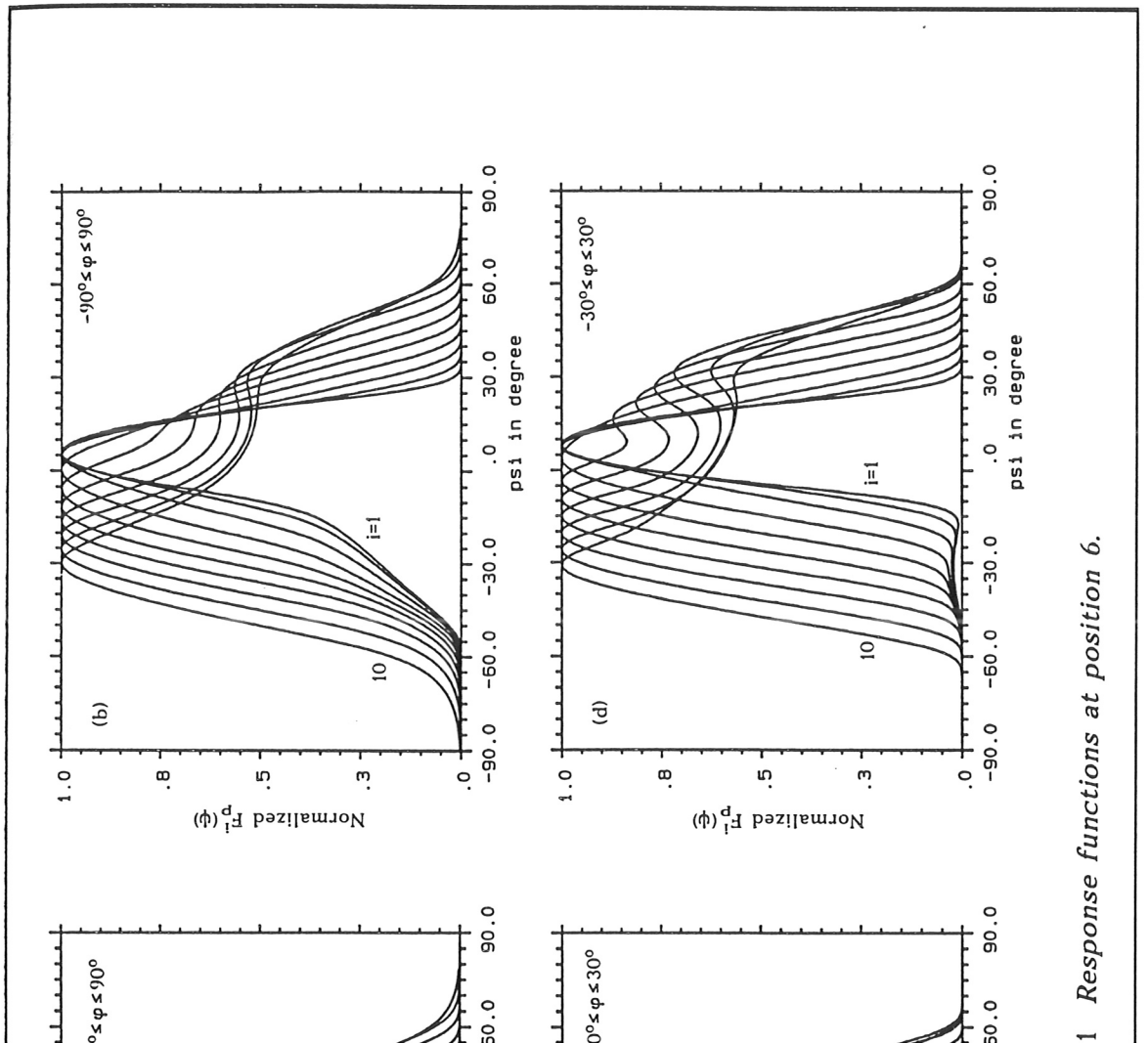

Fig. 7.2.1 Response functions at position 6.

calculated by assuming that S_o = 6.2 cm, E_o = 2.45MeV, ΔE = 0.1MeV and $E_{p,min}$ = 2.3MeV. Then, the ten response functions are integrated over the dip angle in the ranges from -90^o to 90^o (FIG. 7.2.2.a-b) and from -30^o to 30^o (FIG. 7.2.2.c-d). In both cases, as the flux surface radius increases, the corresponding response function becomes broader. The innermost two curves differ only slightly from each other. This indicates that the neutrons emitted in the central plasma region cannot be distinguished from each other by analysis of the corresponding proton tracks. Otherwise, the distributions of the proton tracks are related to the neutron emission source. Comparing the response functions integrated over φ in different ranges, one finds that the ten response functions become more distinguishable from each other as the dip angle is restricted in the smaller range. Moreover, the relative magnitudes of the inner curves, which correspond to the neutrons emitted in the central plasma regions, become greater. This allows an improvement of the accuracy in determining the neutron emission profile near the plasma center.

7.3 Fit Procedure

The distribution of the measured proton tracks, $G(\psi)$, can be described as a linear combination of the ten response functions, i.e

$$G(\psi) = \sum_{i=1}^{10} C_i \, F_P^i(\psi) \tag{7.3.1}$$

with ψ varying from -90^o to 90^o? Here, the ten coefficients C_i $(i=1,10)$ represent the neutron emission profile. According to equation (7.3.1), the coefficients C_i can be determined immediately if ten points on the curves are selected. Due to the errors in the measurements and the finite size of each subzone, the condition (7.3.1) is hard to satisfy. Then, the coefficients C_i have to be determined by minimizing the mean square deviation, i.e.

$$\delta(C_1,\cdots\cdots,C_{10}) = \int_{-90^o}^{90^o} \left(G(\psi) - \sum_{i=1}^{10} C_i \, F_P^i(\psi)\right)^2 d\psi = Min. \tag{7.3.2}$$

with the condition

$$C_i \geq 0 \quad for\ all\ i\,. \tag{7.3.3}$$

Equation (7.3.2) can be rewritten as

$$\delta(\mathbf{C}_1,\ldots\ldots,\mathbf{C}_{10}) = \sum_{i=1}^{10}\sum_{j=1}^{10} \mathbf{C}_i\,\mathbf{C}_j\,A_{ij} - 2\sum_{i=1}^{10} \mathbf{C}_i\,B_i + C, \tag{7.3.4}$$

where

$$A_{ij} = \int_{-90^o}^{90^o} F_P^i(\psi)\,F_P^j(\psi)\,d\psi, \tag{7.3.5}$$

$$B_i = \int_{-90^o}^{90^o} F_P^i(\psi)\,G(\psi)\,d\psi, \tag{7.3.6}$$

$$C = \int_{-90^o}^{90} G(\psi)\,G(\psi)\,d\psi. \tag{7.3.7}$$

In view of the physical meanings of the coefficients $\mathbf{C}_i$, we introduce a fit form for them in order to reduce the number of the variables to be determined. It is defined that

$$\mathbf{C}_i = exp(\,c_o + c_1\,\varkappa_i^2 + c_2\,\varkappa_i^4 + c_3\,\varkappa_i^6\,) \qquad (i=1,10). \tag{7.3.8}$$

Introducing equation (7.3.8) into equation (7.3.4), we determine the parameters c_o, c_1, c_2 and c_3 by varing them separately in order to minimize δ. It should be noted that expression (7.3.8) implies the condition (7.3.3). Furthermore, the parameter c_o is only used for normalizing the calculation to the measurement. This is the reason why not all the constants involved in the procedure were discussed.

Before applying the procedure described above to measurements, we first deduce the neutron emission profile from the proton track distribution provided by VINIA+NEPMC (HÜBNER, 1987; ROOS, 1988). The NEPMC software was developed to simulate the nuclear emulsion response by using Monte Carlo methods. For a given neutron emission profile, the VINIA+NEPMC code predicts an angular distribution of the proton tracks according to the plasma and emulsion plate geometries. The neutron emission profile used in the VINIA+NEPMC calculation is shown in FIG. 7.3.1.b, indicated by the solid line. The resulting angular distribution of the proton tracks simulated by NEPMC (HELBING, 1991) is shown in FIG. 7.3.1.a (solid line). Here, only the neutrons directly emitted from the plasma are taken into account. The dot-dash line in FIG. 7.3.1.a represents the fit curve obtained through optimal superposition of the ten response functions.

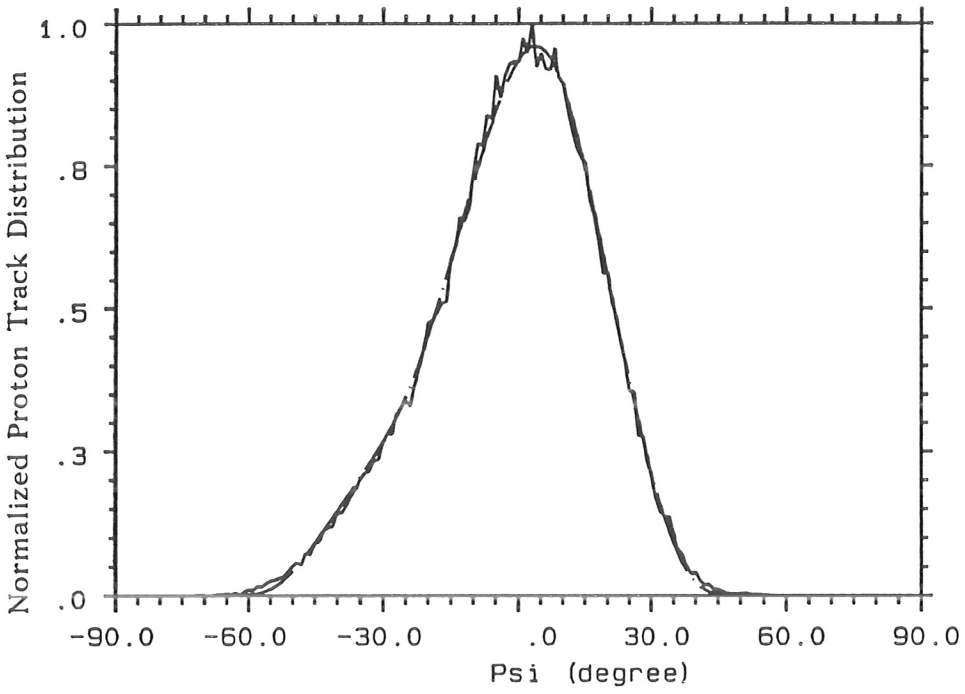

(a) Normalized angular distribution of proton tracks predicted by NEPMC (———) and fit using the response functions (— —)

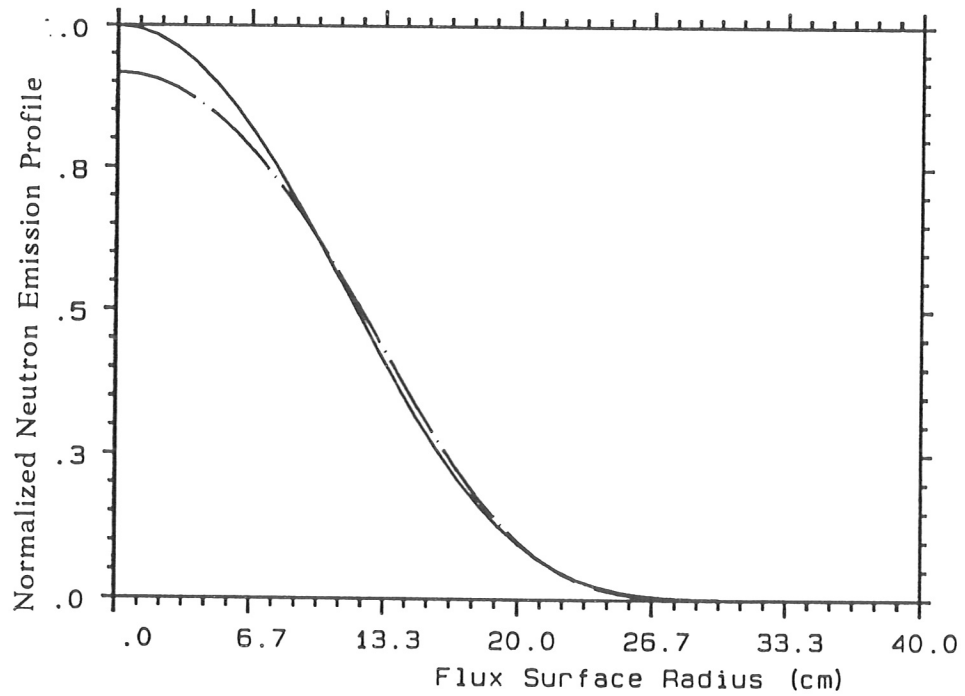

(b) Normalized neutron emission profile as input for NEMPC (———) Compared with that deduced (—·—·) by the fit procedure

FIG. 7.3.1 *Test of the fit procedure developed for deducing the neutron emission profile from the angular distribution of the recoil proton tracks.*

7.4 Applications

At position 6 (HÜBNER, 1989) in the ASDEX tokamak, two nuclear emulsion plates were exposed in order to measure the neutron emission profiles of the D→D discharge *#31136* and the H→D discharge *#30795*. The measured angular distributions of the proton tracks for the two discharges (HELBING, 1991) are given in FIG. 7.4.1.a and FIG. 7.4.2.a by the solid lines. Here, the recoil proton energy is restricted to $\geq 2.3\ MeV$ in both cases. Due to the relatively small number of proton tracks involved in the energy range, the dip angles of the recoil proton tracks were not restricted, in order to reduce the statistical fluctuations.

It should be mentioned that the measured proton tracks are caused by both the neutrons emitted directly from the plasma and those scattered indirectly from the vacuum vessel. The scattered neutrons contribute mainly to the proton tracks in the low-energy range, and therefore this contribution is reduced by the proton energy restriction. However, due to the wide angluar distribution of those proton tracks associated with the scattered neutrons coming from all directions, this contribution should be taken into account. For lack of the response function of the proton tracks to the scattered neutrons, we introduce, according to the VINIA+NEPMC simulations (to be shown in following), a constant, C_{off}, to offset the background contributed by the scattered neutrons. Furthermore, the indicated orientation of the emulsion plate used in the calculations may deviate from the actual one. This would cause a linear deviation of the calculated proton track distribution from the measured one. Assuming that this deviation is $\Delta\psi$ and taking C_{off} into account, we have to rewrite equation (7.3.2) as

$$\delta(C_1,\cdots,C_{10},C_{off},\Delta\psi) = \int_{-90^o}^{90^o}\left(G(\psi) - \left[\sum_{i=1}^{10} C_i\ F_p^i(\psi+\Delta\psi) + C_{off}\right]\right)^2 d\psi = Min. \qquad (7.4.1)$$

With this together with equation (7.3.8), we determine C_{off} and $\Delta\psi$, as well as the neutron emission profile parameters by varying them separately in order to minimize δ.

In this way, the measured proton track distributions for discharges *#31136* and *#30795* are fitted by the calculated response functions, as shown in FIG. 7.4.1.a and FIG. 7.4.2.a (dashed lines). Here, the results from the VINIA+NEPMC simulations (HELBING, 1991) with the input neutron emission profiles from the NR code (BOMBA, 1989) are also shown. In both cases, the VINIA+NEPMC simulations predict nearly constant distributions of the proton tracks caused by the

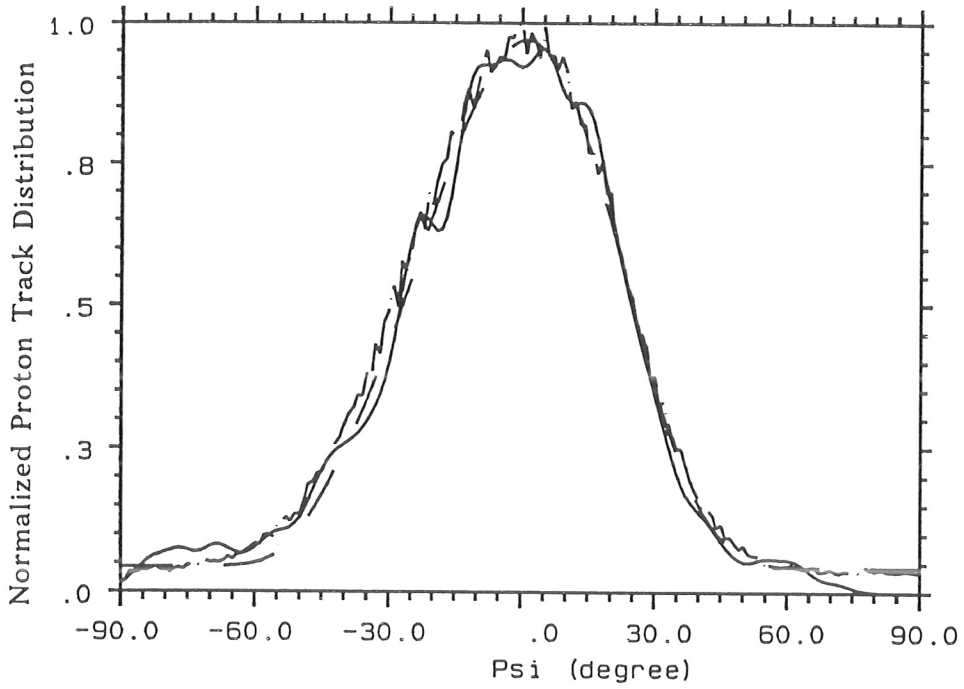

(a) Measured angular distribution of proton tracks (———), fit using the response functions (– – –) and simulation by NEPMC (–·–·)

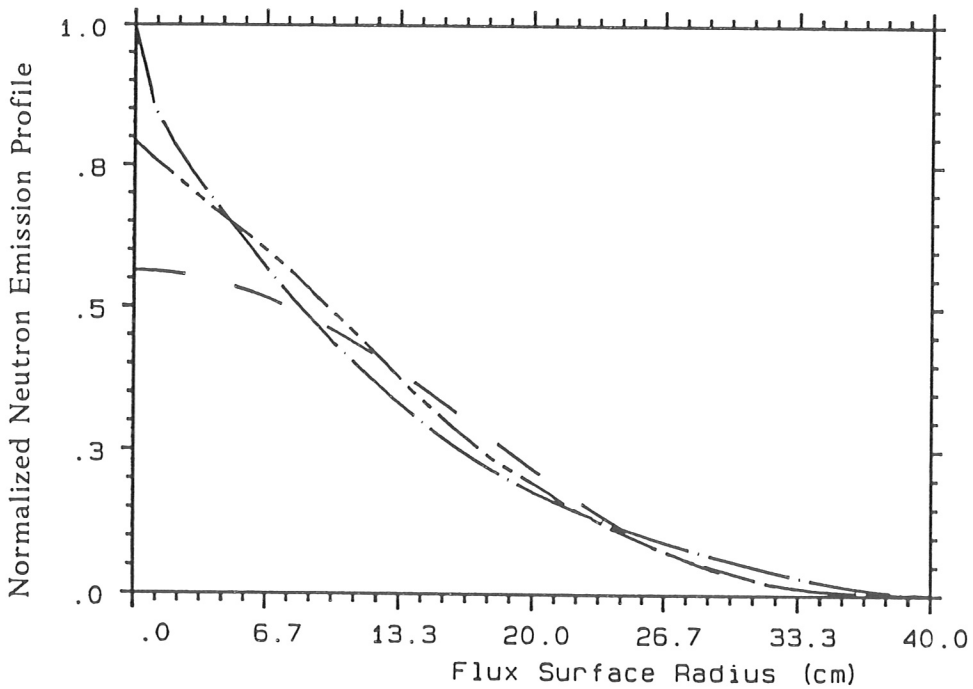

(b) Comparision of the neutron emission profile deduced from the angular distribution of proton tracks (– – –) with that calculated by SINBAD + NRFPS (—— - -) and that from NR code (–·–·) as input for NEPMC simulation

FIG. 7.4.1 *Application to ASDEX discharge #31136 .*

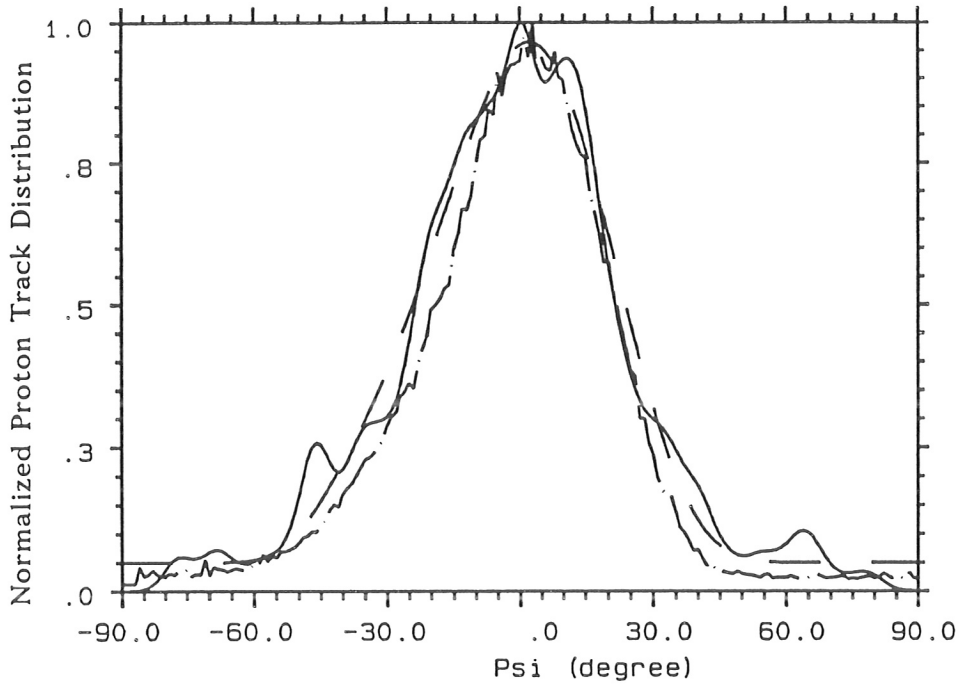

(a) Measured angular distribution of proton tracks (———), fit using the response functions (– – –) and simulation by NEPMC (–·–·)

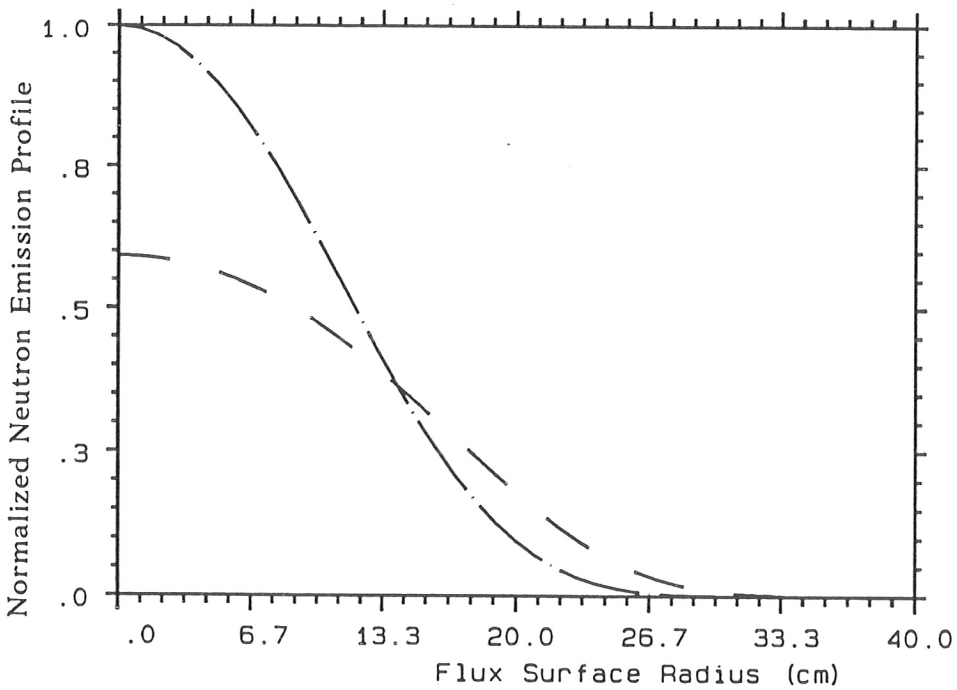

(b) Comparision of the neutron emission profile deduced from the angular distribution of proton tracks (– – –) with that calculated by NR code (–·–·) as input for NEPMC simulation

Comparing the deduced neutron emission profile with that as input for the NEPMC simulation, we find that the neutron rates, in the plasma region with *xa>25cm*, calculated by the NR code are higher than those deduced. Owing to the large plasma volume involved in that region, this gives rise to a broader distribution of the proton tracks. The higher neutron rates in the outside plasma region are due mostly to the fact that the NR code uses the beam deposition profiles calculated by FREYA without taking the initial drift motion of the beam ions into account. As discussed in section (2.6), for co-injection, the fast ions born in the outside region of the torus initially follow circular orbits with radii smaller than those of the circular flux surfaces on which they are born. As an average result, these ions drift towards the inside plasma region. This can be found in the SINBAD+NRFPS calculations, where the initial beam deposition is averaged over the drift orbits of the fast ions. The result is also shown in FIG. 7.4.1.b. It is found that the SINBAD+NRFPS calculations agree well with the measurement, particularly in the outside plasma region.

For H→D discharge *#30795*, the proton track distribution predicted by the NEPMC software is more peaked than that measured by the nuclear emulsion plate (FIG. 7.4.2.a). The neutron emission profile used in the NEPMC simulations is calculated by the NR code, as shown in FIG. 7.4.2.b (HELBING, 1991). It is more peaked than the neutron emission profile deduced from the nuclear emulsion plate measurement. The reason may be that the actual ion temperature profile is broader than that used in the NR calculation. This remains to be confirmed by other ion temperature profile measurements. On the other hand, the number of the proton tracks involved for discharge *#30795* is somewhat too small to allow a rather accurate determination of the neutron emission profile.

The determination of the neutron emission profile is of great importance since the neutron emission profile includes local information about the ions. For plasmas where the reacting ion species can be described by a Maxwellian, the local temperatures or densities of this species can be directly derived from the neutron emission profile. For the deuterium or tritium plasmas with deuterium or tritium injection, the non-Maxwellian distributions of the reacting species can be calculated by the NRFPS code. Thus, either the density profile or temperature profile of the background ions can be deduced from the neutron emission profile through interpretation calculations. In this case, if the plasma temperature is low enough, the ion density profile is immediately obtained without a knowledge of the ion temperature profile.

The calculations of the neutron fluences at the emulsion plate for both discharges were based on the same flux surface geometry where S_O was taken to be *6.2 cm*, that is the average value of *5.9 cm* for *#30795* and *6.5 cm* for *#31136*. This approximation would not entail considerable errors in the results. The indicated orientation of the emulsion plate axis deviates by about *8* degrees from the actual one, which is determined by varying the parameter $\Delta\psi$ introduced in the fit procedure. For the lack of a reliable knowledge of the error sources in the measured proton track distributions, it is impossible to give an error scale

for the deduced neutron emission profiles. However, it is considered that the statistical fluctuations in the measured proton track distributions are the main error sources for the deduced results. Moreover, the effect of the scattered neutrons remains to be considered in more detail.

7.5 Investigation of the Optimal Plate Position

Optimal positioning of a nuclear emulsion plate has practical significance. Here, the distance between the plate and the plasma center is an important parameter. The nuclear emulsion plate should be positioned as close to the plasma as possible. Since the plane angles of the proton tracks can be more precisely measured than the dip angles, the plate should be placed in a poloidal plane where the poloidal angle effectively responds to the neutrons emitted from different flux surfaces. The plate axis should be oriented to around the plasma center, as it was in the ASDEX, due only to the facility for scanning the proton tracks.

FIGURE 7.5.1 gives three positions at the same distance (about *53 cm*) from the plasma center. Position 6 has been discussed. The response functions at position 6-v and position 6-h with the plate axis perpendicular and parallel to the median

plane are shown in FIG. 7.5.2 and in FIG. 7.5.3, respectively. Comparing the response functions at different positions, one finds that the ten response functions at position 6-h can be more effectively distinguished from each other than those at the other two positions. Moreover, at position 6-h, if the plasma possesses D-shaped flux surface geometry, the deviations of the ten response functions from each other become larger due to the elongation of the vertical

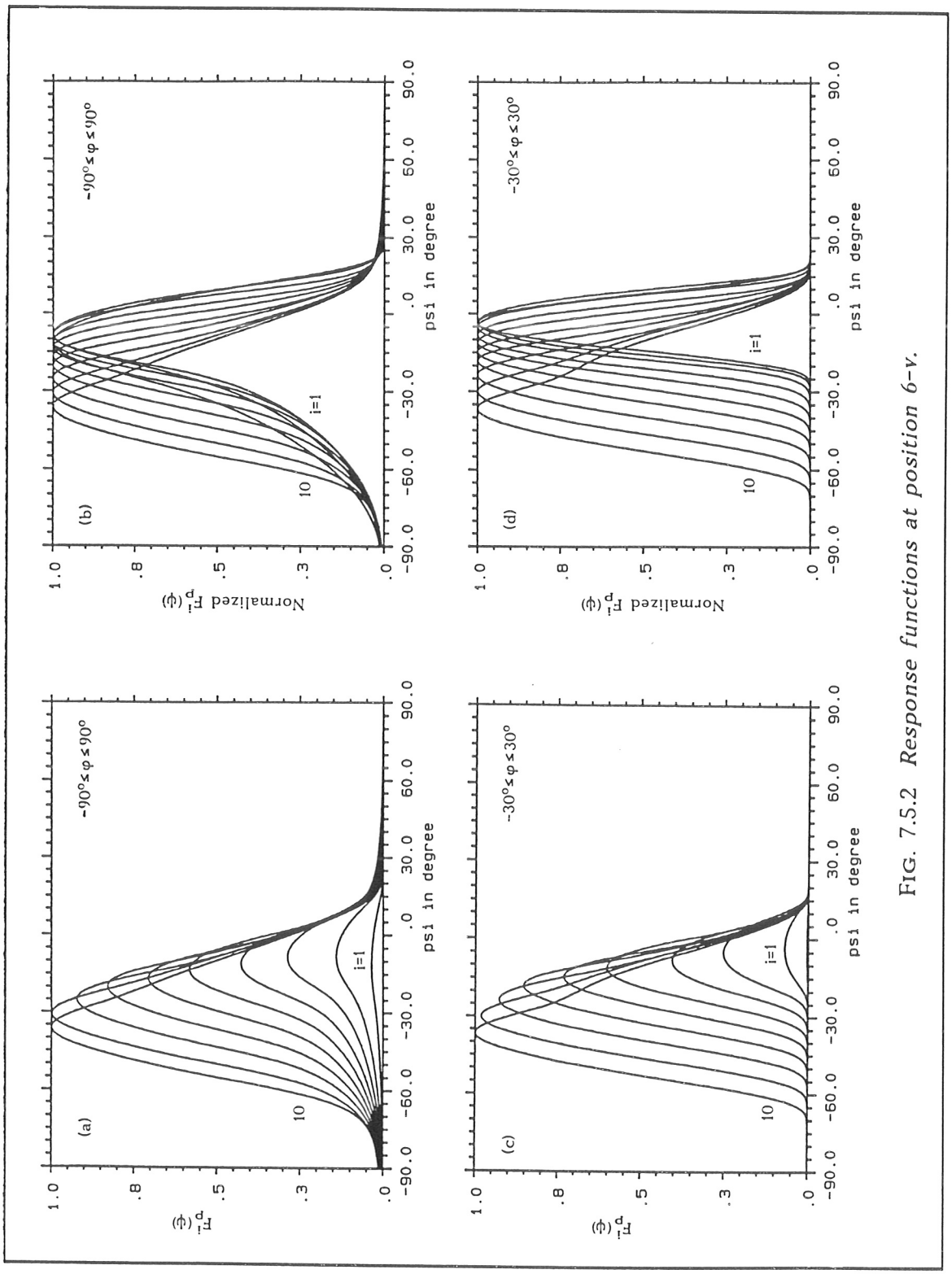

FIG. 7.5.2 *Response functions at position 6-v.*

plasma size. Therefore, position 6-h is considered to be the optimal choice for measuring the neutron emission profile. At position 6-v, the *Shafranov shifts* of the flux surfaces will affect the distributions of the proton tracks more sensitively than at other two positions. Assuming some different values for the *Shafranov shift*, one can calculate the corresponding neutron fluences and response functions. Consequently, the *Shafranov shift* may be determined by introducing a corresponding parameter in the fit procedure.

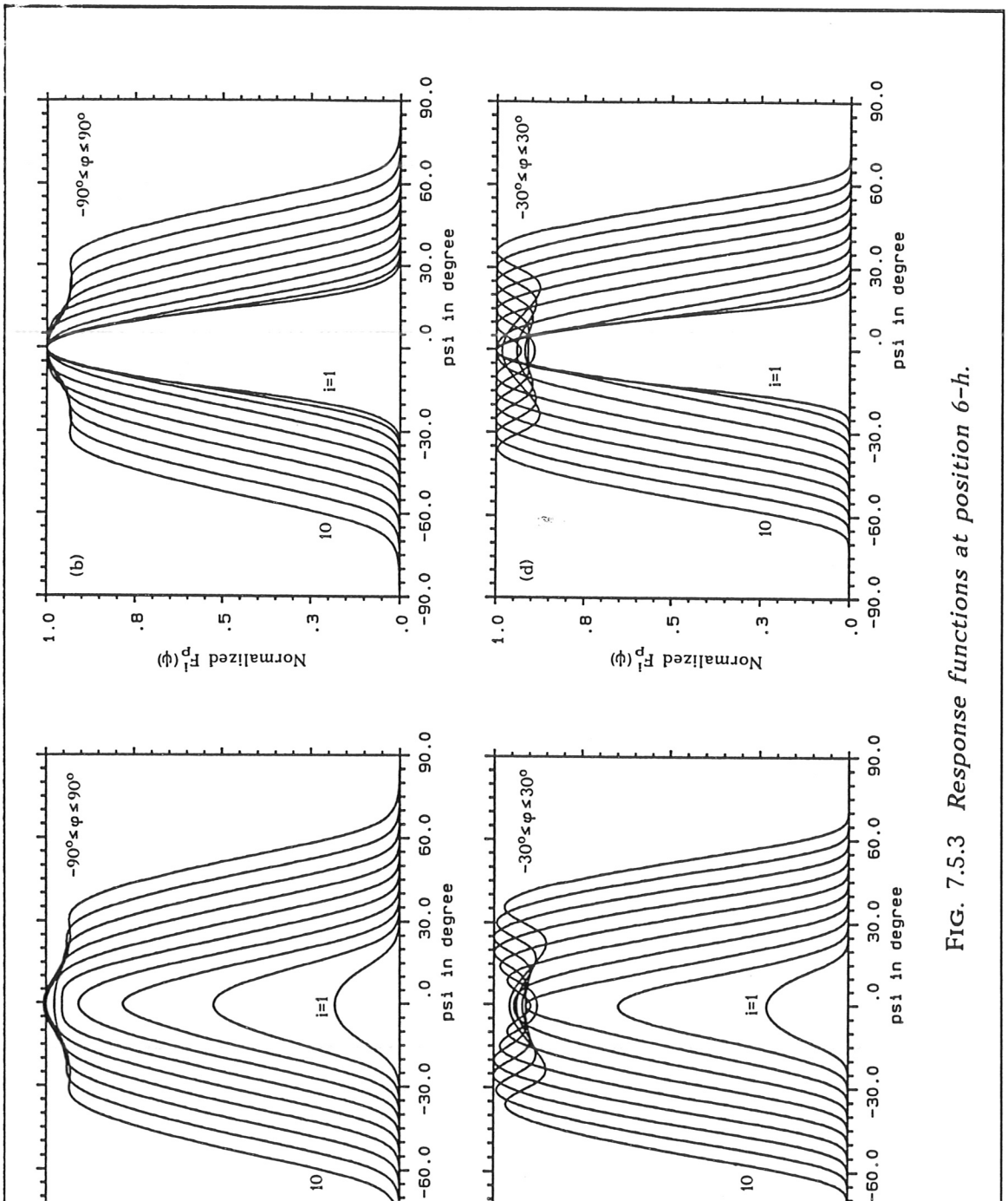

FIG. 7.5.3 *Response functions at position 6-h.*

8. Conclusions

In view of the complex beam geometry, the calculation of the deposition of neutral particles injected into a tokamak plasma is a multi-dimensional problem. Although Monte Carlo methods have been found appropriate to perform the computation, the problem remains time-consuming because of the large dimensionality involved. By careful investigation of the beam intensity distribution and the particle trajectories in the plasma it was found that, since the distance of a source relative to the plasma region is usually much greater than the finite size of the source face, in current injector arrangements, the beam source can be well approximated by a point source. This approximation leads to a reduction of the dimensionality of the beam intensity distribution from four to two. The beam intensity distribution in the plasma region was then derived analytically from a given beam injection geometry and beam focussing property. On the basis of this simplified beam model, a fast computer code, SINBAD, was developed. As contrasted with Monte Carlo codes, the SINBAD code is much less time-consuming and offers the same degree of accuracy in the calculations.

Furthermore, the SINBAD code takes the initial drift motion of the fast ions into account in order to average the effect of the drift motion on the actual distribution of the fast ions in the plasma. Due to the inhomogeneity of the toroidal magnetic field in tokamak devices, the fast ions, once they are born in the plasma, initially follow drift surfaces and not just flux surfaces. The initial drift motion of the fast ions was discussed in detail with the emphasis on their quantitative effects on the final confinement and redistribution of the fast ions in the plasma. In ASDEX plasmas, due to the small injection angle of the beam with respect to the toroidal magnetic field line, few of the penetrating particles are trapped by the magnetic mirror effect. The drift orbits of the passing particles are nearly complete circles displaced from their birth magnetic flux surfaces by a few centimeters, towards the inside or outside of the torus according to their birth positions and pitch angles relative to the plasma current. This drift is very considerable in ASDEX plasmas because of the relatively small plasma currents. This unwished drift motion leads to redistribution of the particle deposition and to loss of the particles ionized in the plasma region near the plasma boundary. The initial drift motion of the fast ions is treated in the SINBAD code rather exactly by using a guiding center theory which takes the complete flux surface geometry and the plasma current intensity distribution into account.

The SINBAD code was compared with other codes. SINBAD, as a reliable and fast computer code, has been installed and is operating on the ASDEX, JET and TEXTOR computer systems and serves for providing particle, energy and

momentum sources in the presence of beam injection. In addition, SINBAD has been linked with the Fokker-Planck code, NRFPS. The combined code is capable of calculating the energy distribution of the slowing-down particles and providing local neutron sources. The SINBAD code can also be coupled with a transport code.

It appears to be difficult to measure the fast particle deposition profile directly. In this work, it has been demonstrated how information about the beam particle deposition can be obtained from the neutron rate and diamagnetic flux measurements. Due to their high energy, the fast ions can significantly increase the neutron production and the plasma energy content. Since the slowing-down process relates neutron rates to many plasma parameters, the slowing-down and neutron production processes were investigated in some detail in order to choose appropriate plasma conditions for enhancing the effect of deposition rates on the neutron rates. For typical ASDEX plasmas which operate at relatively low temperatures, collisions of the fast ions with background electrons dominate the slowing-down process. If the injection energy of the beam particles is given, the quantity, *(electron density*beam particle density)/deposition rate,* is only a function of the electron temperature. For the deuterons with an injection energy of $50\ keV$ and powers of less than $3\ MW$ injected into plasmas with temperatures lower than $2\ keV$ and densities higher than $5*10^{13}/cm^3$, the beam particle density is only a few per cent of the electron density. By analysis of the neutron production processes it was found that, for ASDEX plasmas, the thermal reactivity is more than two orders of magnitude smaller than the beam-thermal and beam-beam reactivities. Thus, most of the neutrons in the presence of beam injection are produced by the beam-thermal reactions. Finally, two counter discharges with temperatures lower than $1\ keV$ and densities higher than $5*10^{13}/cm^3$ were chosen so that the neutron rates mainly depend on the electron temperatures and fast particle deposition rates. In both discharges, the plasma density increased during the beam injection, which led to decreasing deposition rates in the plasma center and, consequently, decreasing neutron rates. This was observed experimentally by using the neutron counters. Furthermore, two other discharges were selected in order to investigate the contribution of the fast particles to the plasma energy content. In these two discharges, the increases of the global plasma energy contents from OH-phases to NBI-phases were mainly due to the fast particle populations. In both cases, the theoretical calculations were highly consistent with the diamagnetic flux measurements.

Usually, the measurement of neutron emission profiles involves complex and expensive detector equipment. In this work, however, a first and successful method of measuring neutron emission profiles by means of nuclear emulsion is presented. A procedure was developed for deducing neutron emission profiles

then derived from the plasma and the emulsion plate geometries. Since the longest proton tracks actually reflect the directions of the incident neutrons, the proton energy was restricted to the high energy range. The neutron emission profile was then obtained by curve fitting in such a way that the ten coefficients of the ten response functions were varied to minimize the mean square deviation from the measured curve. The procedure was first tested by the NEPMC simulation and then applied to two ASDEX discharges. For lack of other relevant measurements, the deduced neutron emission profile for D→D discharge *#31136* was compared with that calculated by the SINBAD+NRFPS code. Since, in the presence of deuterium injection, the neutron emission profile mainly depends on the beam deposition profile and the electron temperature profile, it is considered that the SINBAD+NRFPS code could provide a rather accurate result in this case. Comparison has shown a good consistency of the theoretical calculation with the measurement. For H→D discharge *#30795*, the measured neutron emission profile predicted a broader ion temperature profile than the electron temperature profile. This, however, remains to be confirmed by further ion temperature profile measurements.

ACKNOWLEDGEMENTS

Professor K. Hübner, my academic supervisor at the University of Heidelberg is thanked, for continued support, helpful discussions and encouragement throughout the development of this work.

I am particularly grateful to Priv. Doz. Dr. F. Wagner of Max Planck Institute of Plasma Physics in Garching for his support and interest in my work. Thanks are also due to Dr. O. Vollmer for providing information on the neutral beam injector system at ASDEX.

Useful discussions with Dr. B. Wolle and Dr. B. Bomba, Wolle's contribution to the Appendix and his careful reading of the manuscript are gratefully acknowledged. In addition, I wish to express my gratitude to the neutron diagnostic group at the University of Heidelberg, whose skillful collaboration and help in various respects made this work possible.

This work was supported by Max Planck Institute of Plasma Physics in Garching.

APPENDIX A

DESCRIPTION OF THE MAIN SUBROUTINES USED IN THE SINBAD CODE

SINBAD Subroutine

This main subroutine organizes the computation and assigns the values for variables used in other subroutines.

```
CALL SINBAD (CTRPAR, LPTERM, RFL,   RPOINT, PLDATA, PAINFO,
             HFILE,  DFILE,  KFILE, COORD,  LPOINT, LOCDEP,
             ERINFO)
```

Arguments

Input:

CTRPAR:	Vector containing the control parameters (see sec. A.2.1).
LPTERM:	Flagvector for the expansion of the pitch angle distribution in Legendre polynomials (see sec. A.2.1).
RFL:	Vector containing the flux surface radii (see sec. A.2.1).
RPOINT:	Number of flux surface radius points (see sec. A.2.1).
PLDATA:	Array containing temperature and density profiles for the plasma background particles (see sec. A.2.1).
LPOINT:	Total number of points for local calculations.
COORD:	Array containing the chosen local points expressed in cylindrical coordinates (see sec. A.2.1).

Output:

ERINFO:	Error number (see sec. A.2.2).
PAINFO:	Array containing the number of injected, shine-through, lost and deposited particles for each injection component (see sec. A.2.2).
HFILE:	Array containing initial beam deposition profiles (see sec. A.2.2).
DFILE:	Array containing orbit-averaged profiles (see also sec. A.2.2).
KFILE:	Array containing expansion coefficients for the pitch-angle distribution (see sec. A.2.2).
LOCDEP:	Array containing the results of the local calculation as defined by CTRPAR (see sec. A.2.2).

Remarks

The following global common blocks are used:

COMMON/BEAMG/	– Beam geometry (see sec. A.1.1).
COMMON/BPARA/	– Beam parameters (see sec. A.1.2).
COMMON/FLGEO/	– Flux surface geometry (see sec. A.1.4).
COMMON/PPARA/	– Plasma parameter (see sec. A.1.3).
COMMON/RESULT/	– Output data (see below).

The following internal variables are defined and stored in the corresponding common blocks:

```
      INTEGER
     I   ITOTAL
      REAL
     R   RESOL, RFLUX(40), NE(40), TE(40), NI(10,40), TI(10,40)
      COMMON/PLASMA/
     I   ITOTAL
     R   RESOL, RFLUX(40), NE(40), TE(40), NI(10,40), TI(10,40)

      INTEGER
     I   NRHD
      REAL
     R   RHD(20), BIRTH(3,-40:40,-40:40,-10:10), HPROF(3,20),
     R   DPROF(3,20), DRBETA(3,20,-10:10), VOLUME(20),
     R   XSHIFT(3), PARTIC(4,0:3), KN(3,0:14,20)
      COMMON/RESULT/
     I   NRHD,
     R   RHD,     BIRTH,  HPROF, DPROF, DRBETA, VOLUME,
     R   XSHIFT, PARTIC, KN
```

The plasma is divided into ITOTAL sections. The parameter RESOL determines the size of each section:

$$\text{RESOL} = \text{AMIN}/\text{ITOTAL} \quad (\text{ITOTAL} \leq 40) \tag{A.1}$$

where AMIN is the minor radius. Each section is indicated by a corresponding flux surface radius RFLUX(i) which is normalized to the minor radius AMIN. The local plasma parameters such as TE(i) (electron temperature), NE(i) (electron density), TI(j,i) (temperature of the ion species j) and NI(j,i) (density of the ion species j) at the flux surface radius RFLUX(i) are then interpolated linearly by the PARFIT subroutine. The integer variable NRHD gives the total number of the flux surface radius points RHD(i) which are assigned in SINBAD for calculating the beam deposition profile. In order to suppress the statistical fluctuations which may occur in the beam deposition near to the plasma center, it is necessary that NRHD be smaller than ITOTAL. If there is no specification, a standard value of 15 is assigned to NRHD. It can be changed by the user in the range from 10 to 20.

The other arrays in the common block RESULT and their corresponding symbols used in the text are given in the following table:

Array	Symbol	Remark
BIRTH(l,i,j,k)	$\text{BIRTH}(E_l,R_i,z_j,\mu_k)$	s. section 2.5
HPROF(l,m)	$H(E_l,\varkappa_m)$	s. section 2.5
DRBETA(l,m,n)	$D^*(E_l,\varkappa_m,\mu_n)$	s. section 2.7
DPROF(l,m)	$D(E_l,\varkappa_m)$	s. section 2.7

Usage

```
                    PROGRAM MAIN
                        :
C---> INPUT DATA FOR EXECUTING THE SINBAD CODE
CA:   COMMON BLOCK VARIABLES:
CA.1. BEAM GEOMETRY
      INTEGER
I     NSOURC,      FACE(16)
      REAL
R     RTANG(16),   ROSOUR(16),   ZOSOUR(16),   YOSOUR(16),
R     ZFOCUS(2,16),BDIVER(16),   AGBETA(16),   BWIDTH(2,16)
      COMMON/BEAMG/
I     NSOURC,    FACE,
R     RTANG,     ROSOUR,    ZOSOUR,    YOSOUR,
R     ZFOCUS,    BDIVER,    AGBETA,    BWIDTH
C A.2. BEAM PARAMETERS
      INTEGER
I     DIRECT
      REAL
R     EINJ(3),   COMPIJ(3),   BMASS,    PINJ(0:16)
      COMMON/BPARA/
I     DIRECT,
R     EINJ,      COMPIJ,      BMASS,    PINJ
C A.3. FLUX SURFACE GEOMETRY
      INTEGER
I     FLFORM
      REAL
R     RMAJ,      AMIN,      ZSHIFT,   RVESSI,    RVESSO,
R     SFIT(0:3),EFIT(0:3),DFIT(3),  SDIS(20),  EDIS(20),
R     DDIS(20),  RRZ(-100:100,-100:100)
      COMMON/FLGEO/
I     FLFORM,
R     RMAJ,  AMIN, ZSHIFT, RVESSI, RVESSO,  SFIT,   EFIT,
R     DFIT,  SDIS,   EDIS,   DDIS,     RRZ
C A.4. PLASMA COMPOSITION AND PLASMA CURRENT
      INTEGER
I     NOPART
      REAL
R     ZX(10), PMASS(10), IP, ALPHA
      COMMON/PPARA/
I     NOPART,
R     ZX,      PMASS,      IP, ALPHA
C B: SUBROUTINE VARIABLES (assumed: RPOINT=20, LPOINT=100)
      INTEGER
I     CTRPAR(4),    LPTERM(0:14),     RPOINT,    LPOINT
      REAL
R     RFL(20),   PLDATA(2,0:10,20),   COORD(3,100)
```

```
C----> OUTPUT
       INTEGER
     I   ERINFO
       REAL
     R  PAINFO(4,0:3),  HFILE(0:3,20), DFILE(0:3,20),
     R  KFILE(0:3,0:14,20), LOCDEP(3,100)

C---- DEFINITION END -------
                              :
                              :
       CALL SINBAD (CTRPAR, LPTERM, RFL,     RPOINT, PLDATA
     +              PAINFO, HFILE,  DFILE,   KFILE,
     +              COORD,  LPOINT, LOCDEP,  ERINFO         )
                              :
                              :
       END
```

CKDATA Subroutine

CKDATA is called first by SINBAD to check the input data.

```
CALL CKDATA (CTRPAR, LPTERM, RFL,   RPOINT, PLDATA, COORD,
             LPOINT, ERINFO)
```

Arguments

Input:

CTRPAR:	Vector containing the control parameters (see sec. A.2.1).
LPTERM:	Flagvector for the expansion of the pitch angle distribution in Legendre polynomials (see sec. A.2.1).
RFL:	Vector containing the flux surface radii (see sec. A.2.1).
RPOINT:	Number of flux surface radius points (see sec. A.2.1).
PLDATA:	Array containing temperature and density profiles for the plasma background particles (see sec. A.2.1).
COORD:	Array containing the chosen local points expressed in cylindrical coordinates (see sec. A.2.1).
LPOINT:	Total number of points for local calculations (integer).

Output:

ERRINFO:	Error number (see sec. A.2.2).

Remarks

If one of the input variables takes a value which is:

a) not defined in the code,

b) given in an unacceptable unit,

the input is considered to be unavailable and the computation will be terminated. The possible error will be indicated by ERINFO.

PARFIT Subroutine

This subroutine prepares the internal variables used in SINBAD.

```
CALL PARFIT (RPOINT, RFL, PLDATA)
```

Arguments

Input:

RPOINT:	Number of flux surface radius points (see sec. A.2.1).
RFL:	Vector containing the flux surface radii (see sec. A.2.1).
PLDATA:	Array containing temperature and density profiles for the plasma background particles (see sec. A.2.1).

Remarks

The following global common blocks are used for the output:

COMMON/PLASMA/ – Plasma profile data (see SINBAD).
COMMON/BPARA/ – Beam parameters (see sec. A.1.2).

FLUXGEO Subroutine

This subroutine is used for the LAO representation of the flux surface geometry.

```
CALL FLUXGEO (RPOINT, RFL)
```

Arguments

Input:

RPOINT:	Number of flux surface radius points (see sec. A.2.1).
RFL:	Vector containing the flux surface radii (see sec. A.2.1).

Remarks

The following global common block is used for the output:

COMMON/FLGEO/ – Flux surface geometry (see sec. A.1.4).

The FLUXGEO subprogram performs a numerical solution to the LAO representation (2.3.3) in order to determine the flux surface radius $\varkappa$ for cylindrical coordinates R and z. The output is stored in the vector RRZ in the common block FLGEO. The fixed points (R_i,z_j) are defined in the SINBAD code as:

$$R_i = \text{RMAJ} + i/100*\text{AMIN} \qquad (i=-100,100)$$
$$z_j = \text{ZSHIFT} + j/100*\text{AMIN}*\text{EOUT} \qquad (j=-100,100) \qquad \text{(A.2)}$$

RMAJ: Major plasma radius.
AMIN: Minor plasma radius.
ZSHIFT: Vertical shift of the innermost flux surface from the median plane.
EOUT: Elongation of the outermost flux surface.

PLAVOL Subroutine

This subroutine calculates the volume elements for the plasma geometry used in SINBAD.

```
CALL PLAVOL (ITOTAL, RFLUX)
```

Arguments

Input:

ITOTAL: Number of flux surface radius points (see SINBAD).
RFLUX: Vector containing the flux surface radii (see SINBAD).

Remarks

The following global common blocks are used:

COMMON/FLGEO/ – Flux surface geometry (see sec. A.1.4).
COMMON/RESULT/ – Computational results (output) (see SINBAD).

Remarks

The following common blocks are used for input and output:

COMMON/BPARA/	– Beam parameters (input) (see sec. A.1.2).
COMMON/PPARA/	– Plasma parameter (input) (see sec. A.1.3).
COMMON/PLASMA/	– Plasma profile data (input) (see SINBAD).
COMMON/CRS/	– Cross sections (output) (see below).

The common block CRS is defined as:

```
      REAL
     R    CROSSE(3,40), CROSSI(3,10,40), SIGMA(3,40)
      COMMON/CRS/
     R    CROSSE, CROSSE, SIGMA
```

CROSSE(l,i):	Electron impact ionization cross section on the flux surface RFLUX(i) for the particles injected with the energy EINJ(l).
CROSSI(l,j,i):	Local cross section of the ion species j.
SIGMA(l,i):	Total local rate coefficients.

FRPATH Subroutine

This subroutine calculates the mean free path lengths of the neutrals with different energies in the plasma.

```
CALL FRPATH (NOPART)
```

Arguments

Input:

NOPART:	Number of different plasma ion species.

Remarks

The following common blocks are used for input and output:

COMMON/PLASMA/	– Plasma profile data (input) (see SINBAD).
COMMON/CRS/	– Cross section data (input) (see CSTION).
COMMON/CRBEAM/	– Beam intensity distribution parameters (output).

The common block CRBEAM contains:

FREPTH(i):	Vector containing the mean free path lengths of the neutrals with different energies.
ROUH(i):	Vector containing ρ_h for the different energies (eq. (2.2.3.10)).
ROUV(i):	Vector containing ρ_v for the different energies (eq. (2.2.3.10)).

The factors ρ_h and ρ_v determine the beam intensity distribution as discussed in sec. (2.2.3).

CHEKSYM Subroutine

This subroutine finds symmetric injection sources.

```
CALL CHEKSYM (N, TOTPAI, NOKY)
```

Arguments

Input:

N:	Integer number indicating the injector source (input).
TOTPAI:	Real variable giving the total power of the symmetric sources (output).
NOKY:	Integer array labeling the symmetric sources. If symmetry is found, NOKY(N) = 1; otherwise, NOKY(N) = 0.

Remarks

The following common blocks containing input data are used:

COMMON/BEAMG/	– Beam geometry (see sec. A.1.1).
COMMON/BPARA/	– Beam parameters (see sec. A.1.2).

NARROW Subroutine

This subroutine creates a narrow beam and calculates the beam intensity and the beam trajectory.

```
CALL NARROW (N, RMAJ, AMIN)
```

Arguments

Input:

N:	Integer number indicating the injector source (input).
RMAJ:	Major plasma radius.
AMIN:	Minor plasma radius.

Remarks

The following common blocks are used:

COMMON/BEAMG/	– Beam geometry (input) (see sec. A.1.1).
COMMON/CRBEAM/	– Beam intensity distribution parameters (output) (see FRPATH).

BIRTHDP Subroutine

In this subroutine, the fast ion birth distribution and the deposition profile are calculated.

CALL BIRTHDP (CTRPAR, LPTERM)

Arguments

Input:

CTRPAR: Vector containing the control parameters (see sec. A.2.1).
LPTERM: Flagvector for the expansion of the pitch angle distribution in Legendre polynomials (see sec. A.2.1).

Remarks

The following common blocks containing input data are used:

COMMON/BEAMG/ – Beam geometry (see sec. A.1.1).
COMMON/BPARA/ – Beam parameters (see sec. A.1.2).
COMMON/FLGEO/ – Flux surface geometry (see sec. A.1.4).
COMMON/PPARA/ – Plasma parameter (see sec. A.1.3).
COMMON/PLASMA/ – Plasma profile data (see SINBAD).
COMMON/CRS/ – Cross section data (see CSTION).
COMMON/CRBEAM/ – Beam intensity distribution parameters (see FRPATH).

The output is stored in the common block RESULT. The subroutine calculates:

BIRTH(l,i,j,k) – The fast ion birth distribution BIRTH(E_l,R_i,z_j,μ_k)
HPROF(l,m) – The deposition profile H(E_l,$\varkappa_m$)
XSHIFT(l) – Displacement Δ_x (see section 2.6).
PARTIC(i,j) – Corresponds to PAINFO(i,j) as described in sec. A.2.2.

In order to reduce the computation time, the CHECKSYM subroutine is called to test the beam injection symmetry about the median plane. If the flux surfaces possess up-down symmetry and ZSHIFT is negligibly small, the symmetric sources can be treated as one with their total injection power.

The neutral beam from an operating source is divided into a large number of narrow beams. The number of the narrow beams is determined so that the average width of each narrow beam in the plasma is comparable with the plasma location size defined by RESOL. Once a narrow beam is generated, the NARROW subroutine is called to calculate its intensity based on equations (2.2.3.9-10). The narrow beam is then followed in a mean step corresponding to RESOL. Due to the exponential attenuation of the narrow beam in the plasma, it is necessary to choose nonlinear steps on its path through the plasma.

DDPFILE Subroutine

The initial beam deposition is averaged by using a guiding center theory.

```
CALL DDPFILE (RESOL, NRHD, NPITCH)
```

Arguments

Input:

RESOL: Resolution in the calculation.
NRHD: Number of flux surface raduis points for the deposition profile.
NPITCH: Number of pitch angle points.

Remarks

The following common blocks containing further input data are used:

COMMON/FLGEO/ – Flux surface geometry (see sec. A.1.4).
COMMON/RESULT/ – Computational results (see SINBAD).

From the common block RESULT, the array BIRTH and the vector XSHIFT are input data. The output calculated in this subroutine is stored in the arrays DRBETA and DPROF in the common block RESULT. The initial beam deposition provided from BIRTHDP is averaged by using a guiding center theory. The array DRBETA(E_l,$\varkappa_m$,μ_k) is set up to store the average results. The orbit average beam deposition profile DPROF(E_l,$\varkappa_m$) is given via summation of the particles with different pitch angles. Futhermore, DRBETA(E_l,$\varkappa_m$,μ_k) is normalized to DPROF(E_l,$\varkappa_m$) to get the pitch angle distribution.

GUIDING Subroutine

Output:

LOST:	Indicates whether the fast ion drifts outside the plasma (0/1).
NEND:	Number of time steps for the ion to complete its orbit.
RX, ZX:	Vectors containing the coordinates of the ion for different times.
ANGLE:	Vector containing the pitch angle of the ion for different times.

Remarks

The numerical solution to the guiding center motion equation (2.6.5) is obtained. The time step DT of the traced ions is chosen such that their spatial mean bounce step corresponds to RESOL. Since the drift orbits described by equation (2.6.5) possess up-down symmetry, only the half-orbits above the symmetry plane are calculated. The ions are first followed from their initial position in step DT until they cut the symmetry plane. The orbit is then completed by setting DT negative and repeating the calculation. Whenever the ions are outside the plasma, they are considered to be lost and the parameter LOST is set to 1. Otherwise their position (RX,ZX) and pitch angle ANGLE at the time point t_n are calculated.

LEPOLY Subroutine

This subroutine expands the pitch angle distribution in Legendre polynomials and calculates the expansion coefficients $k_i(E_l,\varkappa_m)$.

```
CALL LEPOLY (KFLAG, NPITCH)
```

Arguments

Input:

KFLAG:	Integer vector indicating the coefficients to be calculated: KFLAG(J)=1 (yes); KFLAG(J)=0 (no).
NPITCH:	Number of points in the pitch angle space.

Remarks

This subroutine uses the common block RESULT as described in SINBAD. The array DRBETA contains further input data. The output is stored in the array KN.

LOCALDP Subroutine

The local beam deposition rates of the particles, their energy or momentum at the points chosen by the user are calculated.

```
CALL LOCALDP (MFLAG, POINTS, NPTOT, MOMOUT)
```

Arguments

Input:

MFLAG:	Contains the value of CRTPAR(4) (see sec. A.2.1).
POINTS:	Array corresponding to COORD (see sec. A.2.1).
NPTOT:	Number of local points.

Output:

MOMOUT:	Array containing the local deposition rates. This array has the same definitions as LOCDEP in sec. A.2.2.

Remarks

Further input data are stored in the following common blocks:

COMMON/BEAMG/	– Beam geometry (see sec. A.1.1).
COMMON/BPARA/	– Beam parameters (see sec. A.1.2).
COMMON/FLGEO/	– Flux surface geometry (see sec. A.1.4).
COMMON/PPARA/	– Plasma parameter (see sec. A.1.3).
COMMON/PLASMA/	– Plasma profile data (see SINBAD)
COMMON/CRS/	– Cross section data (see CSTION)

The local points have to be given in a cylindrical coordinate system with origin in the tokamak centre. The injector is located on the axis ($z=0, \varphi=0$).

A.1 Common Blocks

A.1.1 Common Block BEAMG - Beam Geometry

Variable	Type	unit	Description
NSOURC	I		Total number of operating sources (maximal: 16)
FACE(n)	I		Face shape of the source n: 0 = circular; 1 = rectangular.
RTANG(n)	R	cm	Tangential radius of the beam axis of the operating source n with respect to the tokamak center.
ROSOUR(n)	R	cm	Distance of the source n relative to the tokamak center.
ZOSOUR(n)	R	cm	Distance of the source n with respect to the median plane (above: positive).
YOSOUR(n)	R	cm	Horizontal deviation of the source n from the injector center (on the side of tokamak it is negative).
ZFOCUS(1,n)	R	cm	Horizontal focus length of the neutral particle beam from the source n.
ZFOCUS(2,n)	R	cm	Vertical focus length of the neutral particle beam from the source n.
BDIVER(n)	R	Deg.	Beam divergence for the source n.
AGBETA(n)	R	Deg.	Angle between the beam axis of the source n and the median plane (above: positive).
BWIDTH(1,n)	R	cm	Face width of the source n.
BWIDTH(2,n)	R	cm	Face height of the source n.

A.1.2 Common Block BPARA - Beam parameter

Variable	Type	unit	Description
DIRECT	I		Injection direction relative to the toroidal plasma current: +1: co-injection, -1: counter-injection.
EINJ(N)	R	keV	Injection energies: n=1: full energy, n=2: half energy, n=3: one-third energy.
COMPIJ(N)	R		Fractions of the neutral particles with different energy components
BMASS	R	amu	Atomic mass of the injected atom.
PINJ(N)	R	MW	Injection power: PINJ(0): total injection power n=1,NSOURCE: the injection power of the source n.

A.1.3 Common Block PPARA - Plasma Composition and Current

Variable	Type	unit	Description
NOPART	I		Total number of plasma ion species.
ZX(n)	R		Charge of the ion species n.
PMASS(n)	R	amu	Atomic mass of the ion species n.
IP	R	kA	Toroidal plasma current.
ALPHA	R		Profile parameter used for a parabolic current profile: $j(\varkappa)$ = const*I_{PLAS}*$(1 - \varkappa^2)^{\alpha}$.

A.1.4 Common Block FLGEO - Flux Surface Geometry

Variable	Type	unit	Description
FLFORM	I		Indicates the way to determine the flux surface geometry: 0: use LAO representation. The flux surface parameters (Shafranov shift, elongation and triangularity) are fitted with eqs. (2.3.4-6), 1: use LAO representation but only some discrete values for the flux surface parameters will be supplied. 2: Set up an arbitary flux surface geometry by the user.
RMAJ	R	cm	Major plasma radius.
AMIN	R	cm	Minor plasma radius.
ZSHIFT	R	cm	Shift of the innermost flux surface from the median plane (above: positive).
RVESSI	R	cm	Radius of the inner vessel.
RVESSO	R	cm	Radius of the outer vessel.
SFIT(n)	R	cm	Coefficients of the expansion (2.3.4) to describe the shift of the flux surfaces (they are required if FLFORM=0).
EFIT(N)	R		Coefficients of the expansion (2.3.5) to describe the elongation of the flux surfaces (they are required if FLFORM=0).
DFIT(n)	R	cm	Coefficients of the expansion (2.3.6) used to describe the triangularity (they are required if FLFORM=0).
SDIS(j)	R	cm	Shafranov shifts of chosen flux surface radii RFL(j) (needed if FLFORM=1).
EDIS(j)	R		Elongations of chosen flux surface radii RFL(j) (needed if FLFORM=1).
DDIS(j)	R	cm	Triangularities of chosen flux surface radii RFL(j) (needed if FLFORM=1).

A.2 Main Subroutine Variables

A.2.1 Input Data

Variable	Type	unit	Description
CTRPAR(n)	I		Job control parameters: n=1: Calculate H(r) (1=Y, 0=N). 2: Calculate D(r) (1=Y, 0=N). 3: Calculate k_i(r) (1=Y, 0=N). 4: Calculate local deposition rates at chosen points: 0: NO. 1: Local particle deposition. 2: Local energy deposition. ≥3: Local momentum deposition where the vector is given in: 3: Cartesian coordinates 4: Cylindrical coordinates. 5: Plasma coordinates.
LPTERM(j)	I		Calculate the j-th term coefficient of the Legendre polynomials (1=Y, 0=N).
RPOINT	I		Total number of the flux surface radius points for beam deposition profile.
LPOINT	I		Total number of local points.
RFL(i)	R		Normalized flux surface radii at which the beam deposition will be provided.
PLDATA(1,i,j)	R	keV	Temperature profiles of the plasma background particles: i=0: electron, i≥1: ion species i.
PLDATA(2,i,j)	R	cm^{-3}	Density profiles of the plasma background particles: i=0: electron, i≥1: ion species i.
COORD(1,j)	R	cm	R—coordinate of the chosen local point j in the cylindrical coordinate system with origin in the tokamak centre.
COORD(2,j)	R	Deg.	φ—coordinate of the local point j.
COORD(3,j)	R	cm	z—coordinate of the local point j.

A.2.2 Output Data

Variable	Type	unit	Description
PAINFO(i,j)	R	s^{-1}	Injected neutral particle details: i=1: The number of injected particles with EINJ(j) (total: j=0). 2: Shine-through particles corresponding to different energy components (total: j=0). 3: Orbit-lost particles (total: j=0). 4: Deposited particles (total: j=0).
HFILE(j,n)	R	$cm^{-3}s^{-1}$	Initial fast ion birth deposition profile of the particles with different energy components (total: j=0).
DFILE(j,n)	R	$cm^{-3}s^{-1}$	Orbit-averaged deposition profile for different energy components (total: j=0).
KFILE(j,l,n)	R		The Legendre polynomial coefficients of the pitch angle distributions of the fast ions with EINJ(j) at $\varkappa_n$
LOCDEP(j,i)	R	$cm^{-3}s^{-1}$	Local deposition rates at chosen points [COORD(1,i), COORD(2,i), COORD(3,i)] CTRPAR(4)=1: Deposition rates of the particles with EINJ(j). CTRPAR(4)=2: Energy deposition rates arising from the neutral particles with EINJ(j). CTRPAR(4)=3: Momentum deposition rates where the momentum vector is represented in Cartesian coordinates (x,y,z) indicated by j=1,2,3. CTRPAR(4)=4: Represent the momentum vector in the cylindrical coordinates (R,φ,z) for j=1,2,3. CTRPAR(4)=5: Represent the momentum vector in the plasma coordinates: j=1: $\varkappa$; j=2: φ, toroidal component; j=3: β, poloidal component.
ERINFO	I		Error notice: 0: No errors in the input data; the execution is successful; ≥1: There are errors in: 1: control parameters (CTRPAR); 2: beam geometry; 3: beam parameters; 4: flux surface geometry; 5: plasma composition or current; 6: flux surface points (RPOINT or RFL); 7: plasma parameter profiles (PLDATA); 8: local points (LPOINT or COORD).

REFERENCES

BOMBA, B. (1989), Ph. D. Thesis, Universität Heidelberg, 6900 Heidelberg, Germany.

BOSCH, H.-S. and HALE, G. M. (1992), *Nucl. Fusion,* **32**, 611.

CHALLIS, C. D. *et al.* (1989), *Nucl. Fusion,* **29**, 563.

CORDEY, J. G. (1976), *Nucl. Fusion,* **16**, 499.

CORDEY, J. G. *et al.* (1975), *Nucl. Fusion,* **15**, 441.

CORRIGAN, G., MUIR, D. G. and TIBONE, F. (1992), Neutral Beam-Plasma Interaction in JET: Comparison of PENCIL and TRANSP Modelling Results, Rep. JET-R(91) 14, JET Joint Undertaking, Abingdon, Oxfordshire.

DAVIS, S. L., MUELLER, D. and KEANE, C. J. (1983), *Rev. Sci. Instrum.,* **54**, 315.

DUESING, G., ALTMANN, H., FALTER, H., GOEDE, A., HANGE, R., HEMSWORTH, R. S., KUPSCHUS, P., STORK, D. and THOMPSON, E. (1987), *Fusion Technology* **11** (1), 163.

FIORE, C. L., MEDLEY, S. S., HAMMETT, G. W. and KAITA, R. (1988), *Nucl. Fusion,* **28**, 1315.

FOWLER, R. H., HOLMES, J. A., and ROME, J. A. (1979), NFREYA - a Monte Carlo Beam Deposition Code for Non-circular Tokamak Plasmas, Rep. ORNL-TM-6845, Oak Ridge National Laboratory, Tennessee.

FREEMAN, R. and JONES, E. (1974), Rep. CLM-R137, Culham Laboratory, Abingdon, Oxfordshire.

GERNHARD, J. and SCHNEIDER, F. (1986), Design and Electronic Compensation of a Diamagnetic Loop and Its Application in the ASDEX Tokamak, IPP III/84, Max-Planck-Institut für Plasmaphysik, Garching.

GOLDSTON, R. J. (1975), *Nucl. Fusion,* **15**, 651.

GOLDSTON, R. J., MCCUNE, D. C., TOWNER, H. H., DAVIS, S. L., HAWRYLUK, R. J. and SCHMIDT, G. L. (1981), *J. Comput. Phys.* **43**, 61.

GRISHAM, L. R., EUBANK, H. P., KAMPERSCHROER, J. H., KUGEL, H. W., MARTIN, G. D., PRECHTER, R. E., PRICHARD JR, B. A., WILLIAMS, M. D., WINJE, R. A. and WRIGHT, K. E. (1985), *Nucl. Instr. and Methods* **B10/11**, 478.

HAWRYLUK, R. J. (1980), *Proc. International School of Plasma Physics, Course of Physics of Plasmas close to Thermonuclear Conditions*, Varenna, 1979, Vol. 1, p. 19.

HELBING, S. (1991), Diplomarbeit, Universität Heidelberg, 6900 Heidelberg, Germany.

HEIDERINK, W. W. *et al.* (1988), *Nucl. Fusion,* **28**, 1897.

HÜBNER, K., BÄTZNER, R., HINSCH, H., RAPP, H., WURZ, H., EBERHAGEN, A., GEHRE, O. and MERTENS (1985), V., 12th European Conference on Controlled Fusion and Plasma Physics, Europhys. Conf. Abstracts, **9F I**, 231.

HÜBNER, K., ROBOUCH, B. V. *et al.* (1987), Influence of Neutron Scattering and Source Extent on the Measurement of Neutron Energy Spectra at ASDEX, IPP III/122, Max-Planck-Institut für PlasmaPhysik, Garching.

HÜBNER, K., BÄTZNER, R., BOMBA, B., RAPP, H., HERRMANN, W., MURMANN, H., EBERHAGEN, A., FAHRBACH, H.-U., GEHRE, O. PREIS, R., RÖHR, H., STEUER, K.-H. and VOLLMER, O. (1988), 15th European Conference on Controlled Fusion and Plasma Heating, Europhys. Conf. Abstracts, **12B III**, 1191.

HÜBNER, K., BÄTZNER, R., BOMBA, B., BOSCH, H.- S., BRZOSKO, J. S., VAN CALKER, C., HINSCH, H., INGROSSO, L., KLEIN, R., KUCINSKI, J., ROBOUCH, B. V. and WOLLE, B. (1989), Tokamak Neutron Calibration at High Yields Using Combined Nuclear Emulsion Measurements, Indium Activation, and VINIA-3DAMC Simulation, IPP III/132, Max-Planck-Institut für Plasmaphysik, Garching.

IFRC (International Fusion Research Council) (1979), *Nucl. Fusion,* **18,** 137.

IFRC (International Fusion Research Council) (1990), *Nucl. Fusion,* **30,** 1641.

JANEV, R. K., BOLEY, C. D., and POST, D. E. (1989), *Nucl. Fusion,* **29**, 2125.

JARVIS, O. N. (1991), Neutron Diagnostics for Tokamak Experiments, Rep. JET-P(91)13, JET Joint Undertaking, Abingdon, Oxfordshire.

JARVIS, O. N., GORINI, G., HONE, M., KÄLLER, J., SADLER, G., MERLO, V., and VON BELLE, P. (1986), *Rev. Sci. Instrum.,* **57(8)**, 1717.

KADOMTSEV, B. B., TROYON, F. S., MATKINS, M. L., RUTHERFORD, P. H., YOSHIKAWA, M. and MUKHOVATOV, V. S. (1990), *Nucl. Fusion,* **30,** 1675.

KAITA, R. *et al.* (1985), *Nucl. Fusion,* **25**, 939.

KALLENBACH, A., MAYER, H.-M., FUSSMANN, G., BÜCHSE, R., GRUBER, O., KLÜBER, O., MERTENS, V., VOLLMER, O. and ZOHM, H. (1990), *Nucl. Fusion,* **30**, 645.

KILLEEN, J. and FUTCH, A. H. (1968), Jr., *J. Comput. Phys.,* **2**, 236.

KILLEEN, J., KERBEL, G. D., MCCOY, M. G. and MIRIN, A. A. (1986), Computational Methods for Kinetic Models of Magnetically Confined Plasmas, *Springer Series in Computational Physics.*

LAO, L. L., HIRSHMAN, S. P. and WIELAND, R. M. (1981), *Phys. Fluids* **24**, 1431.

LISTER, G. G., POST, D. E., and GOLDSTON, R. (1976), *Proc. Third Symposium on Plasma Heating in Toroidal Devices*, Varenna, 1976, p. 303.

LISTER, G. G. (1985), A Fully 3-D Neutral Beam Injection Code Using Monte Carlo Methods, Rep. IPP 4/222, Max-Planck - Institut für Plasmaphysik, Garching.

MARCUS, F. B., ADAMS, J. M., CHEETHAM, A. D., CONROY, S., CORE, W. G. F., JARVIS, O. N., LOUGHLIN, M. J., OLSSON, M., SADLER, G., SMEULDERS, P., VAN BELLE, P. and WATKINS, N. (1991), *Plasma Physics and Controlled Fusion,* Vol. 33, No. 4, 277.

MATSUDA, S., AKIBA, M., ARAKI, M., DAIRAKU, M., EBISAWA, N., HORIIKE, H., ITOH, T., KANAI, T., KAWAI, M., KOMATA, M., KURIYAMA, M., KITAMURA, S., MATSUOKA, M., MIZUHASHI, K., OHGA, T., OHHARA, H., OHUCHI, Y., OHARA, Y., OKUMURA, Y., SHIBANUMA, K., SHIBATA, T., SHIRAKATA, H., SUGAWARA, T., TANAKA, S. and WATANABE, K. (1987), *Fusion Eng. and Design* **5**, 85.

MUKHOVATOV, V. S. and SHAFRANOV, V. D. (1971), *Nucl. Fusion,* **11**, 605.

REBUT, P-H. *et al.* (1991), Fusion Energy Production from a Deuterium-Tritium Plasma in the JET Tokamak, Rep. JET-P(91)66, JET Joint Undertaking, Abingdon, Oxfordshire.

RIVIERE, A. C. (1971), *Nucl. Fusion* **11**, 363.

ROME, J. A., CALLEN, J. D., CLARKE, J. F. (1974), *Nucl. Fusion* **14**, 141.

ROSENBLUTH, M. N. *et al.* (1957), *Phys. Rev.,* **107**, 1.

STUBBERFIELD, P. M. and WATKINS, M. L. (1987), JET Experimental Department Research Note DPA(06)87, Multiple Pencil Beam.

SWEETMAN, D. R. (1973), *Nucl. Fusion* **13**, 157.

TRUBNIKOV, B. A. (1965), Particle Interactions in a Fully Ionized Plasma, *Rev. of Plasma Phys.,* Ed. Leontovich, N. Y.

WAGNER, F. *et al.* (1989), The H-Mode of ASDEX, Rep. IPP III/151, Max-Planck-Institut für Plasmaphysik, Garching.

WEISEN, H., VON HELLERMANN, M., BOILEAU, A., HORTON, L. D., MANDL, W. and SUMMER, H. P. (1989), *Nucl. Fusion,* **29**, 2187.

WOLLE , B. (1990), Ph. D. Thesis, Universität Heidelberg, 6900 Heidelberg, Germany.

ZARNSTORFF, M. C. *et al.* (1988), *Phys. Rev. Lett.* **60**, 1306.